Optical nanomanipulation of nanostructures on azobenzene-containing films

Anh-Duc Vu

ÉCOLE
POLYTECHNIQUE
UNIVERSITÉ PARIS-SACLAY

Thèse présentée pour obtenir le grade de

DOCTEUR DE L'ECOLE POLYTECHNIQUE

Spécialité: Physique

par

Anh-Duc VU

Optical nanomanipulation of nanostructures on azobenzene-containing films

soutenue le 20 Octobre 2014 devant le jury composé de:

M.	Fabrice Charra	CEA	Rapporteur
M.	Romain Quidant	ICFO	Rapporteur
M.	Jean-Jacques Greffet	Institut d'Optique	Examinateur
M.	Thierry Gacoin	Ecole Polytechnique	Examinateur
M.	Yves Lassailly	Ecole Polytechnique	Directeur de thèse
M.	Jacques Peretti	Ecole Polytechnique	Co-Directeur de thèse

Abstract

In the present work, we use the photoinduced mass transport in thin films containing azobenzene derivatives to manipulate matter at the nanoscopic scale. First, we develop a simple method to elaborate periodic arrays of metal structures with adjustable plasmonic properties. The dispersion diagrams of the surface plasmons are measured and exhibit, as expected, the opening of an energy bandgap and of an unusual momentum-gap. The latter arises from the interaction of the plasmon modes of the two interfaces on either sides of the metal film. Near-field measurements show the localization of the plasmon-enhanced optical field on the periodic structure, in agreement with calculations by RCWA. Second, we demonstrate the optical control of the displacement of nanoparticles, both metallic and dielectric, on the surface of an azobenzene-containing thin film. Displacement over several microns is observed with the direction controlled by the light polarization. This provides a new toolkit to manipulate nanoparticles at the nanoscale and gives deeper insight into the mechanisms at the origin of the photoinduced mass transport in azobenzene-containing films.

Résumé

Dans ce travail, nous exploitons les propriétés photomécaniques des matériaux contenant des molécules photochromiques dérivées de l'azobenzène pour manipuler optiquement la matière à l'échelle nanoscopique. Tout d'abord, nous développons une méthode simple pour élaborer des réseaux périodiques de nano-structures métalliques dont les propriétés plasmoniques peuvent être ajustées par le contrôle du motif élémentaire. Le diagramme de dispersion des plasmons de surface de ces structures est mesuré. Il présente, comme attendu, l'ouverture d'une bande interdite en énergie mais aussi une structure inhabituelle correspondant à l'ouverture d'un « gap en k », dû à l'interaction des modes plasmons des deux interfaces de part et d'autre de la couche métallique. Dans un second temps, nous démontrons, pour la première fois, le contrôle optique du déplacement de nanoparticules sur la surface d'un film mince d'azo-matériau. Des déplacements de plusieurs microns sont observés avec un contrôle de la direction du mouvement par la polarisation de la lumière. Ces résultats fournissent une nouvelle boîte à outils pour la manipulation des nanoparticules à l'échelle nanométrique et permettent de mieux comprendre le phénomène de transport de matière photo-induit dans les films contenant des molécules d'azobenzène.

Contents

List of Figures

Remerciement

Cette thèse, financée par l'Ecole Polytechniaque, a été réalisée au laboratoire de Physique de la Matière Condensée (PMC) de l'École. Elle n'aurait pu être accompli sans la contribution de nombreuses personnes auxquelles j'exprime toute ma reconnaissance et ma gratitude.

Je remercie à François Ozanam, le directeur du labo, de m'avoir accueilli au sein de PMC, de son grand sourire permanent et de l'énergie qu'il m'a accordé pour trouver des solutions autant dans la recherche que dans les démarches administratives.

La pluridisciplinarité à PMC m'a permit de réaliser cette thèse dans un cadre de collaboration étroite entre physiciens et chimiste du labo. Ainsi, j'ai pu bénéficier de l'expertise des grands maîtres et de la compétence de leur grand disciple.

Je remercie Yves Lassailly et Jacques Peretti, mes deux directeurs de thèse. Leurs enseignements, encouragement et orientation ont été déterminant. J'ai été très motivé par leur confiance et la liberté à qu'ils m'ont accordé au travail. J'ai beaucoup apprécié leur facilité à l'instrumentation, e.g. la ténacité de Jacques à la réparation de la tête du microscope.

Je remercie Thierry Gacoin qui m'a ouvert la voie vers les sciences des matériaux à travers son cours sur les matériaux fonctionnels à l'X. Sa suivi, ses idées et ses encouragement ont été essentiels pour la réalisation de ce travail.

Merci à Nico, le grand partenaire chimiste.[1] Je suis très content et fier du travail qu'on a réalisé ensemble. Son énergie et son attitude de combattant ont joué un rôle très important pour surmonter des longues heures de manips à multiple échecs.

Je remercie au maître tout puissant du bricolage Lucio Martinelli. J'ai beaucoup bénéficié de sa grande connaissance des instruments, de son énergie inépuisable et de ses idées brillantes.

Merci à Filippo Fabbri de ses idée et de son investissement dans ce travail. Les moments passés à discuter le papier autours d'un café où d'une bière (des fois jusqu'à 10 heures du soir dans Paris) me seront inoubliable.

Je remercie Khalid Lahlil et Jean-Pierre Boilot des leçons de chimie et de bons moments passé au labo et sur les chemins de course. La révision du cours de chimie de solide de Jean-Pierre que j'avais eu en SMNO m'a beaucoup fait regretter de n'avoir pas investi plus de temps dans cette belle matière.

J'exprime toute ma gratitude à Jean-Jacques Greffet qui a accepté de présider le jury de thèse. Je remercie qu'à Romain Quidant et à Fabrice

[1] redoutable mécanicien.

Charra pour leur lecture attentive de mon manuscrit de thèse, en tant que rapporteur.

Merci à Fouad Maroun, mon co-bureau, de la formation très pédagogique et intéressant au microscope électronique à balayage ainsi que de son coup de main à dépanner les instruments avec beaucoup d'enthousiasme malgré son calendrier chargé.

Je remercie à Jean-Paul Hugonin de l'Insitut Optique et à Vlacheslav Kubisky, post-doc à PMC de leurs aides dans la simulation numériques et des discussions fructueuses.

Je suis reconnaissant à l'ensemble des éminents physiciens du groupe Électrons Photons Surfaces de m'avoir accueilli parmi eux. J'exprime en particulier ma gratitude à George Lampel pour les discusions fructueux et ses aides dans le montage du dispositif de comptage de photon.

Je remercie à l'ensemble de l'équipe de service commun. Merci aux mécanos Dédé et Domininique pour leur professionnalisme et des jolies composantes mécaniques toujours ponctuellement délivrés; aux informaticiens Julien Monguillon et Denis Coupvent-Desgraviers et l'électricien Didier Lenoir; à Patrice Delaroque de ses encouragement, ses plaisanteries et de ces éclats de rire qui rendent l'ambiance au labo très accueillant. Merci à Eve Brunwic, Anne Marie Dujardin et Blandine André de vos efforts à faciliter mes démarches administratives.

A PMC reigne une ambiance agréable de l'humour, de l'ouverture, de la gentillesse et de la convivialité avec de nombreuses moments de partage. Je remercie aux thésards, post-docs, mud guys, footballeurs, parachutistes, Pointγ-barmen, coureurs, danceurs, ... avec qui j'ai côtoyer pendant ces trois années et qui en ont fait une période inoubliables de ma vie.

Enfin, je remercie à ma famille et à mes amis d'être toujours derrière moi pendant les bons et les difficiles moments.

Introduction

Light allows transporting energy, information, interacts with matter and plays thus important role in technology. Moreover, light is particularly interesting thanks to its relative ease of manipulation (i.e. generation, transport and interaction with matter), to its abundance as being the main component of the solar spectrum, to its strong interaction with matter, including living organs and to its wavelength being in the nano range which makes it elemental in nanotechnology. This explains the large general interest over the last decades to develop light-based technologies. In order to optimize the material design, the understanding of the light-matter interaction is required. At the fundamental level, one continues to discover intriguing phenomena of light-matter interaction. Recently, one phenomenon which has triggered both fundamental and application interest is the photo-induced mass transport in azobenzene-containing films. On one hand, its possibility to convert light energy into mechanical work at the molecular level is rather unique. On the other, a complete theoretical account of this phenomenon is still elusive. No existing models is capable of explaining all the experimental observation.

The photo-induced mass transport in azobenzene-containing film was discovered in 1995 simultaneously by two independent research groups [1, 2]. They observed the generation of a surface relief pattern upon exposing such films to the interference of appropriate light. One rapidly pointed out its link to the photochromic properties of the azobenzene molecules, i.e. their change of color upon exposure to light [3]. Interestingly, much of the research effort was thus far devoted to inhibiting such photochromic property as it was unfavourable to the principal use of azobenzene derivatives as commercial dyes.[2] Since the discovery of the photo-induced mass transport, the photochromic properties of the azobenzene derivative has gain a new place, in the conception of novel photo-responsive materials.

The present work is devoted to the study of the photo-manipulation of nano-objects and the elaboration of nanostructured systems with tailored optical properties. In the first part, we study the optical control of the

[2] Up to 70% of the world's commercial dyes are still azobenzene-based [4].

displacement of nanoparticles, metallic or dielectric, on the surface of an azobenzene-containing thin film. We employ shear-force microscopy to observe the effect of the illumination on the azobenzene-containing thin film and the nanoparticles.

In **Chapter 1**, we introduce the azobenzene molecule, the azobenzene-based materials and the photoinduced mass transport.

In **Chapter 2**, we detail the methods used to obtain polymeric thin films containing-azobenzene which bring about the photo-induced mass transport. This study makes intensive use of a home-made instruments: a system of coupled shear-force/near-field optical microscopy. The working principles and the characteristics of this instruments will be described.

In **Chapter 3**, we demonstrate, for the first time, the optical control of the displacement of nanoparticles, both metallic and dielectric, on the surface of an azobenzene-containing thin film. Displacement over several microns is observed. By carrying out the experiments under different illumination conditions, we establish the relation between the displacement and the illumination (polarization, intensity, wavevector) and the photochromic thin film (materials, thickness) properties. Moreover, we prove that this movement is a consequent of the photo-induced mass transport.

In the second part, we develop a simple method to elaborate periodic arrays of metal structures with adjustable plasmonic properties. The plasmonic properties are studied by measuring the dispersion diagrams of the surface plasmons by angular-resolved reflectance spectroscopy and by mapping out the plasmon-enhanced optical field on the periodic structure by optical near-field microscopy. Calculation of the optical properties is carried out to interpret the experimental data.

In **Chapter 4**, we provide a brief background on the surface plasmons (SP) phenomenon. This will serve as the basis to understand the plasmonic properties of the periodic arrays of metal structures that we have studied.

In **Chapter 5**, we detail methods to obtain hybrid metal/dielectric nanostructures using the photo-induced mass transport in thin films containing azobenzene. We also describe the a home-made apparatus of Angular-Resolved Reflectance Spectroscopy which allows to measure the dispersion curves of the surface plasmons.

Chapter 6 is dedicated to the optical and plasmonic properties of the periodic arrays of metal nanostructures. The photo-induced mass transport combined with metal thermal evaporation offer a simple and robust technique to obtain such metal arrays which are among the basic devices in optics and plasmonics. We consider two types of metal structures: continuous metal films and discontinuous arrays of metal structures. Concerning the continuous metal films, the surface corrugations, or grating, can prohibit

the propagation of the surface plasmon, as expected, in a range of energy but can also prohibit the excitation of SP in a range of momentum. The latter arises from the interaction of the plasmon modes of the two interfaces on either sides of the metal film. Near-field measurements show the localization of the plasmon-enhanced optical field on the periodic structure, in agreement with numerical calculation. On the other hand, the structure of the discontinuous metal arrays can be optically modified as long as the photochromic film is active. This attracts us into studying the manipulation of their optical and plasmonic properties using light. The result of this research will also be presented and discussed.

In the last part, we will discuss some of the implication of this study and the remaining questions on the mechanism at the origin of the photo-induced mass transport. Our future direction in this research will also be presented. In the manuscript, we use for convenience "azobenzene" and "azo" interchangeably to refer to the class of compounds that exhibit the core azobenzene structure, with different ring substitution patterns. Likewise, "azofilm" and "azomaterial" are used to refer to azobenzene-containing film and material, respectively.

Bibliography

[1] P. Rochon, E. Batalla, and A. Natansohn. Optically induced surface gratings on azoaromatic polymer-films. *Appl. Phys. Lett.*, 66(2):136–138, 1995.

[2] D. Y. Kim, S. K. Tripathy, L. Li, and J. Kumar. Laser-induced holographic surface-relief gratings on nonlinear-optical polymer-films. *Appl. Phys. Lett.*, 66(10):1166–1168, 1995.

[3] GS Hartley. The cis-form of azobenzene. *Nature*, 140:281, 1937.

[4] Kevin G. Yager and Christopher J. Barrett. *Azobenzene Polymers for Photonic Applications*, pages 1–46. John Wiley & Sons, Inc., 2008.

Part I

Optical control of nanoparticle motion

Chapter 1

Background on photo-induced mass transport in photochromic materials

The discovery of photo-induced mass transport in azobenzene-containing materials in 1995 [1, 2] has made azobenzene a major compound in the conception of photo-responsive materials. The lack of a coherent theoretical model for this phenomenon does not prevent the flourishing of original ideas to harness the photo-mechanical properties. This section summarizes the current understanding and exploitation of this phenomenon. We first describe the azobenzene molecule and its derivatives. We next consider a particular class of azobenzene-containing materials, polymeric like materials with azobenzene derivatives grafted as side chains, in which the photo-induce mass transport was first evidenced. Such materials are used throughout this work for the photo-manipulation. We will present the important experimental results and the prominent theoretical models concerning the photo-induced mass transport in such materials.

1.1 Azobenzene molecule and its isomerisation

The azobenzene molecule consists of two phenyl rings connected by a -N=N- double bond as depicted in **Figure 1.1** (a). The molecule can exist in two stable conformations, also called "isomers", the thermally stable "trans" isomer and the metastable "cis" isomer whose energy is 50 kJ/mol (~ 0.52 eV per molecule) higher [3]. The azo molecule can switch between its isomers by absorption of a photon of appropriate energy. This process is known

as the photo-isomerization and is at the origin of the photochromism of the azobenzene molecules, i.e. their change of color under excitation by light. Moreover, the optimal photo energy for the photo-isomerization can be tailored, via the substitution of the phenyl ring, to lie anywhere from the ultra-violet (UV) to the visible red region.

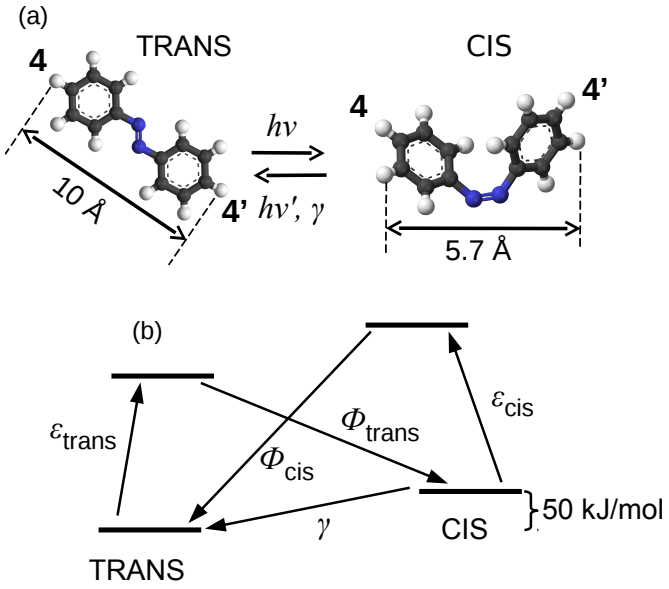

Figure 1.1: (a) Azobenzene molecules in trans and cis configurations. (b) Schematic energy diagram of azobenzene highlighting the photo-isomerization. We denote ϵ_{trans} and ϵ_{cis} the cross-section of light absorption in the trans and cis states, respectively. Φ_{trans} and Φ_{cis} denote the quantum yields of the indicated photo-isomerization and γ is the thermal relaxation rate.

1.1.1 Mechanism of the photo-isomerization

The photo-isomerization of azobenzene occurs as the molecule is put in an excited state by a photon of suitable energy. The following relaxation give rise to a change of conformation, trans $\rightarrow$ cis, or the reverse. **Figure 1.1** (b) shows a simplified energy diagram highlighting the electronic transitions involved in the photo-isomerization. These electronic transitions take place at the N=N bonding, from the bonding states (n) or (π) towards the anti-bonding states π, denoted by $\pi*$: $n \rightarrow \pi*$ and $\pi \rightarrow \pi*$. The change of conformation may occur following two different pathway, through a rotation

about the N=N bond, with rupture of the π bond, or through inversion, with the π bond remaining intact [3]. Rotation is the main mechanism in the thermal relaxation. In the photo-isomerization, both mechanisms are possible and depend on the specific compound [3]. The timescale of the photo-isomerization is of the order of picoseconds while the thermal relaxation, cis $\rightarrow$ trans, may take from milliseconds to hours [3, 4], depending on the given azobenzene molecule and its environment.

1.1.2 Classification of azobenzenes

One of the key properties of azobenzene lies on the ease to tailor the photo-isomerization energy by adding substituents to the phenyl rings. The resulting molecules are called azobenzene derivatives and are classified into three groups according to their absorption spectrum [5]:

- the azobenzene-type molecules - These compounds exhibit a yellow color. Their absorption spectrum is characterized by a low intensity $n \rightarrow \pi*$ band in the visible region and a much stronger $\pi \rightarrow \pi*$ band in the UV range. The relatively slow cis $\rightarrow$ trans thermal relaxation allows to isolate the cis form.

- the aminoazobenzene-type molecules - These orange compounds are obtained by substitution on the phenyl rings of an electron-donating group (usually an amino, -NH_2. The $n \rightarrow \pi*$ and $\pi \rightarrow \pi*$ bands are much closer or even overlap. The molecules of this class exhibit faster cis $\rightarrow$ trans relaxation than the case of the azobenzene-type.

- the pseudo-stilbenes – These red compounds are obtained by the so-called "push-pull" substitution scheme. The 4 and 4$'$ positions (see **Figure 1.1** (a)) are substituted with an electron-donor and an electron-acceptor (such as an amino -NH_2 and an nitro -NO_2 group). The electronic distribution is strongly asymmetric resulting in a broad overlap of the absorption spectra of the trans and cis isomers. The isomerization cycle can hence be induced by illumination with a single light wavelength. These molecules, when grafted into a host medium, can give rise to photo-induced mass transport as will be described later. In our study, we use the so-called dispersed red 1 (DR1) azobenzene derivative of pseudo-stilbene type.

1.1.3 Photo-reorientation and birefringence

The absorption cross-section of the trans isomer is strongly anisotropic which is not the case for the cis isomer. The trans $\rightarrow$ cis isomerization occurs

more readily when the molecular electric dipole is in better alignment with respect to the polarization of the incident light. The molecules whose electric dipole axis lies perpendicular to the light polarization do not absorb and therefore do not isomerize. The reverse process, cis $\rightarrow$ trans, produces trans isomers with equal probability of orientation. Therefore, under illumination with linearly polarized light, the trans population undergoes a net progressively reorientation, known as the *angular hole-burning* process, to a configuration such that all the electric dipoles are perpendicular to light polarization. The photo-induced angular hole-burning can give rise to strong optical anisotropy, i.e. birefringence or dichroism, in azobenzene containing films. Birefringence Δn of up to 0.5 at $633nm$ in azo-polymers has been reported [6, 7]. This optical anisotropy slowly relaxes by the random thermal movement of the molecules. More interestingly, it can be modified or erased also by illumination and can find application in data storage. For instance, linear birefringence can be erased using circularly polarized light which exhibit a rotational symmetry. Instead, this type of beam turns the azobenzene molecules to align along its propagation axis [3]. Since the photo-induced reorientation requires multiple isomerization cycling, it is more conveniently achieved with the pseudo-stilbene systems.

1.2 photo-induced mass transport

The effect of illumination on the properties of the azobenzene containing materials brings about the idea of making photo-tunable materials. Such materials have attracted important research effort as they offer a novel way to develop light-based technology. A good review of the current developments of azobenzene-based materials is [8]. In the followings, we will focus on the photo-induced mass transport in thin films containing azobenzene derivatives. Thin phenomenon not only offers interesting practical applications but also arises ongoing debate on its photo-mechanical mechanism.

1.2.1 Macroscopic effects

During the photo-isomerization of the azobenzene molecules, part of the light energy is translated into mechanical work. This provides azobenzene-containing systems with unique photo-mechanical properties. For instance, the surface potential, i.e. its wettability, can be optically controlled via an auto-assembly of a monolayer of azobenzene. A spectacular demonstration is the transport of a macroscopic water droplet by an illumination gradient [9–11]. Another strategy to harness the photo-mechanical properties of the azobenzene molecules is by putting them into polymer films. As shown in [12], a self-standing azo-polymer film can be optical bended and unbended

along the direction of the light polarization. The mechanical force here is provided by the contraction of the film surface where the photo-isomerization takes place.

1.2.2 Mass transport

Thin films containing the pseudo-stylbene derivatives exhibit a spectacular photo-induced mass transport phenomenon. When the photo-isomerization of the chromophores is excited, the film surface exhibit deformation according to the illumination pattern. This results in a surface relief pattern which remains stable even when the illumination is off. Thermal effects were rapidly ruled out since this phenomenon occurs well below the glass transition temperature, T_g, of the azo-films. The deformation occurs efficiently even under very weak illumination (typically well below 1 W/cm^{-2}) that gives rise to no significant temperature increase. Furthermore, during the surface deformation process, the nature of the material and its density is not altered. These evidences point to a transport of matter triggered by the photo-isomerization of the azobenzene derivatives. The phenomenon was first reported in 1995 simultaneously by two research groups who observed the appearance of a surface relief grating (SRG) on an azo-polymer film upon exposure to an optical interference pattern (**Figure 1.2**) [1, 2]. The height of the surface structures, depending on the exposure, may attain heights comparable to the film's thickness while their periods are given by the interference pitch. It is remarkable to note that half of the film's mass is moved over several-micron-distance by a rather weak optical interference pattern.

Even though the microscopic mechanism of the photo-induced mass transport is not completely known, studies on the different hosting materials, the types of dyes and the grafting methods have evidenced the critical role of the the azobenzene molecules and their photo-isomerization [2, 13, 14]. Replacing the chromophores removes or reduces drastically the efficiency of the SRG formation. The molecules of the pseudo-stilbene are the most suitable since their isomerization can be excited by one wavelength giving rise to continuous cycling of the isomers. The photodeformation process follows in general two stages. First, a photoexpansion of the hosting material takes place within a few photo-isomerization cycles. This photoexpansion is not reversible and corresponds to the increase in the free volume required to accommodate the isomerizing chromophores [15, 16]. Subsequently, the photo-induced mass motion sets in. This process is fully reversible [17, 18]. The photo-induced pattern is flattened upon annealing the sample above the glass transition temperature T_g of the polymeric materials or by activating the isomerization using uniform illumination. Moreover, by shifting

the interference pattern, one can translate the surface pattern [19, 20]. Finally, the efficiency of the photo-induced mass transport depends strongly on the light polarization [21]. Indeed, the direction of the photo-induced transport is mainly governed by the gradient of the light polarization inside the azobenzene-containing films [22].

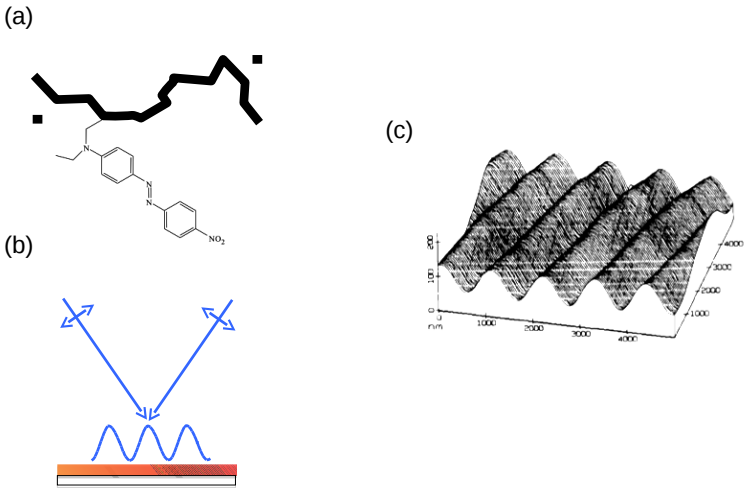

Figure 1.2: (a) Azobenzene derivative of pseudo-stilbene family grafted as side-chain to a polymer backbone. (b) Interference pattern projected on an azofilm, the light wavelength is within the photo-isomerization band of the azobenzene derivative. (c) photo-generated surface-relief grating (SRG), image courtesy taken from [23].

On the other hand, it is also possible to optically deform the azobenzene-containing film by using a subwavelength light source. **Figure 1.3** illustrates the dots inscribed by a metal-coated, tapered optical fiber tip [24]. These dots exhibit a lateral size of $50nm$, which is ten times smaller than the wavelength of the inscribing light, and a height attaining $20nm$. The shapes of the surface structures depend on the tip-to-sample distance which conditions the distribution of the electromagnetic field [22]. Irradiating the sample in far-field produces a groove, surrounded by two lobes, which are aligned along the light polarization. This pattern is created by a displacement of matter away from the center of the illuminated area in the direction along the light polarization. On the other hand, a source held within the wavelength-scale distance from the surface "attracts" the matter towards it. This behaviour is attributed to the presence of a significant electric field component perpendicular to the surface. This component is, however evanescent and is thus absent in a far-field illumination scheme. The resulting structures are round protrusions whose diameter is equal to the size of the light source.

This observation demonstrates the possibility to optically inscribe surface structures in the subwavelength scale.

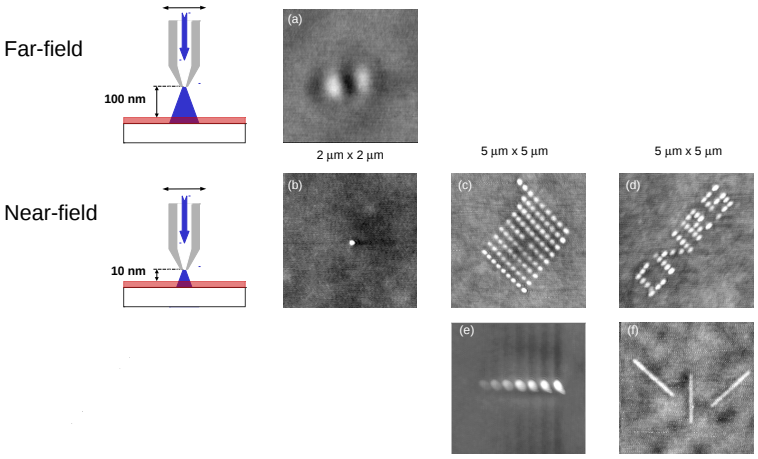

Figure 1.3: Surface deformation induced by a nanosource

An important effect of the photo-isomerization is the softening of the host film. Karageorgiev and the coworkers evidenced the reduction of the Young module and the plastic yield of the film during the photoizomerization which is unrelated to the thermal effect [25]. Moreover, it is possible to induce a spreading of the film in the parallel direction of the light polarization. The authors showed a strong evidence of this phenomenon by optically induce a filling up of a channel carved in azofilm. Only the channel perpendicular to the light polarization is filled while the parallel one is unaffected. The direction control of the mass transport is recently demonstrated in a striking way using optical vortex by Ambrosio and the coworkers [26, 27]. They were able to inscribe spiral patterns whose shapes reflects the topography of the beam, namely its orbital angular momentum of a Laguerre-Gauss-style optical vortex beams. This photo-softening effect is the crucial element in some of the theoretical models of the photo-induced mass transport, especially to facilitate the transport under the weak predicted photo-generated force.

1.2.3 Mechanism of the photo-induced mass transport in azofilms

The photo-induced mass transport is a specific property of materials incorporating azobenzene derivatives of the pseudo-stilbene class. The conformation cycling of the azobenzene derivatives enables the conversion of light energy into mechanical work that displaces matter. The exact conversion mechanism is however still debated since no existing theoretical model is capable of explaining all to experimental observations [28]. The kinetics, the

direction of the transport and the amount of matter involved depend on the optical pattern, the host materials and how the azobenzene derivatives are incorporated. The photo-isomerization of the azobenzene derivatives softens the film as is evidenced by load-penetration measurements [25]. Whether this softening is essential for the photo-generated driving force to overcome the materials' plastic yield is still unclear [29, 30]. The optical heating is negligible as the mass-transport happens at temperatures far below the glass transition temparature of the films [17, 18]. The photoexpansion, i.e. the increase of the free volume to accommodate the isomerizing azobenzene molecules, plays a minor role in the mass transport. It accounts only for several nanometers out of hundreds in the total height of the photo-generated SRGs [20]. Two features of the interference pattern independently drive the SRGs generation, namely, the intensity gradient and the polarization gradient. They simultaneously govern the photo-induced mass transport [20, 22] where the polarization gradient drive is usually predominant.

Table 1.1 summarizes the most prominent theories with their validity and drawbacks:

Model	**Assumption**	**Validity**	**Invalidity**	**Refs**
Field gradient (Kumar *et al.*)	Driving force $\propto$ gradient of electric field	Good qualitative agreement in most cases	Too weak predicted driving force; invalid in p-asssited $s-s$ interference	[29, 31, 32]
Orientation approach (Toshchevikov *et al.*)	Electrostriction-like effect due to the photo-reorientation	Photo-induced pressure $\parallel$ light polarization	Invalid in $s-s$ interference	[30]
Asymmetric diffusion (Lefin *et al.*)	Asymmetric random walk of azo-molecules	Good qualitative agreement in most cases	Polymer azo-materials; unclear microscopic origin	[33]
Permittivity gradient (Baldus *et al.*)	Driving force $\propto$ refractive index gradient	Transport direction in amorphous materials	The essential role of azobenzene does not manifested	[34]
Mean-field (Perdersen *et al.*)	Dipolar interaction between azo-molecules	Liquid-crystalline azo-materials	Amorphous azo-materials	[35]

Table 1.1: Theoretical models of the photo-induced SRGs generation in azofilm.

1.3 Materials fabrication and matter manipulation by light

1.3.1 photo-generation of SRGs

The photo-mechanical response azobenzene-containing films opens up the possibility of simple, rapid, reversible all-optical method for surface patterning. 1-dimensional (1D) or 2-dimensional (2D) photonic crystals of surface structures can be easily obtained by reversible, few-step processes without having to resort to chemical development. The same approach can be generalized to 3-dimensional (3D) structures through stacking [36]. Moreover, by combining azopolymer mask with plasma etching (RIE), one can extend the scope of this approach to conventional semiconductor materials such as ITO or silicon [37, 38]. The reversibility of the process is of particular interest since it allows adjusting in posterior the azobenzene-containing structures. The potential of this approach is demonstrated in a recent series of work on the so-called Directional Photofluidization Lithography (DPL) [39–41].

1.3.2 Transport of nano-objects using azobenzene

Large amount of matter can be optically transported over micron-distances in azobenzene-containing films. Monolayer of azobenzene auto-assembly allows to transport liquid droplets by optical gradient. Wrapping nano-objects with a monolayer of azobenzene provide them the capacity to swim in aqueous media under optical activation [42]. These are the most notable examples of employing azobenzene to assist the optical transport of matter. Even though the most spectacular transport is associated with polymer-like azobenzene-containing films, optical transport of nano-objects on this platform remains so far unfruitful.

1.4 Conclusion

Azobenzene-containing films exhibiting photo-induced mass transport can be used as a platform for the optical control of matter at the nanoscale. Even though the mechanism at the origin of this phenomenon is not fully clear, intensive effort has been put on exploiting these photo-mechanical properties. In Chapter 3, we will show that directional movement of nanoparticles can be optically induced on azobenzene containing films. The dependence of the movement on the azofilm and the illumination allows to attribute it to the photo-mechanical properties of the azofilm. This finding also gives deeper insight into the mechanism of the photo-induced mass transport in this medium.

Bibliography

[1] P. Rochon, E. Batalla, and A. Natansohn. Optically induced surface gratings on azoaromatic polymer-films. *Appl. Phys. Lett.*, 66(2):136–138, 1995.

[2] D. Y. Kim, S. K. Tripathy, L. Li, and J. Kumar. Laser-induced holographic surface-relief gratings on nonlinear-optical polymer-films. *Appl. Phys. Lett.*, 66(10):1166–1168, 1995.

[3] Kevin G. Yager and Christopher J. Barrett. *Azobenzene Polymers for Photonic Applications*, pages 1–46. John Wiley & Sons, Inc., 2008.

[4] Igor K. Lednev, Tian-Qing Ye, Ronald E. Hester, and John N. Moore. Femtosecond time-resolved uv-visible absorption spectroscopy of trans-azobenzene in solution. *The Journal of Physical Chemistry*, 100(32):13338–13341, 1996.

[5] Hermann Rau. *Photoisomerization of azobenzenes*, volume 2. CRC Press: Boca Raton, FL, 1990.

[6] A Natansohn, P Rochon, M Pezolet, P Audet, D Brown, and S To. Azo polymers for reversible optical storage. 4. cooperative motion of rigid groups in semicrystalline polymers. *Macromolecules*, 27(9):2580–2585, 1994.

[7] Rainer Hagen and Thomas Bieringer. Photoaddressable polymers for optical data storage. *Advanced Materials*, 13(23):1805–1810, 2001.

[8] Y. Zhao and T. Ikeda. *Smart Light-Responsive Materials: Azobenzene-Containing Polymers and Liquid Crystals*. Wiley, 2009.

[9] LM Siewierski, WJ Brittain, S Petrash, and MD Foster. Photoresponsive monolayers containing in-chain azobenzene. *Langmuir*, 12(24):5838–5844, 1996.

[10] D Gustina, E Markava, I Muzikante, B Stiller, and L Brehmer. Photoisomerisation process of self-assembled monolayers of some novel azobenzene. *Advanced Materials for Optics and Electronics*, 9(6):245–251, 1999.

[11] Kunihiro Ichimura, Sang-Keun Oh, and Masaru Nakagawa. Light-driven motion of liquids on a photoresponsive surface. *Science*, 288(5471):1624–1626, 2000.

[12] Yanlei Yu, Makoto Nakano, and Tomiki Ikeda. Photomechanics: directed bending of a polymer film by light. *Nature*, 425(6954):145–145, 2003.

[13] A. Natansohn and P. Rochon. Photoinduced motions in azo-containing polymers. *Chem. Rev.*, 102(11):4139–4175, 2002.

[14] Bruno Darracq, Frédéric Chaput, Khalid Lahlil, Jean-Pierre Boilot, Yves Levy, Valerie Alain, Lionel Ventelon, and Mireille Blanchard-Desce. Novel photorefractive sol-gel materials. *Optical materials*, 9(1):265–270, 1998.

[15] Damien Garrot. *Étude par microscopie en champ proche des phénomènes de migration de matière photo-induite dans les matériaux photochromiques*. PhD thesis, Université Paris-Sud Orsay, 2006.

[16] D. Garrot, Y. Lassailly, K. Lahlil, J. P. Boilot, and J. Peretti. Real-time near-field imaging of photoinduced matter motion in thin solid films containing azobenzene derivatives. *Appl. Phys. Lett.*, 94(3):033303, 2009.

[17] N. Mechau, D. Neher, V. Börger, V.ger, H. Menzel, and K. Urayama. Optically driven diffusion and mechanical softening in azobenzene polymer layers. *Applied Physics Letters*, 81(25):4715, 2002.

[18] Kevin G Yager and Christopher J Barrett. Temperature modeling of laser-irradiated azo-polymer thin films. *The Journal of chemical physics*, 120(2):1089–1096, 2004.

[19] Christopher J. Barrett, Jun-ichi Mamiya, Kevin G. Yager, and Tomiki Ikeda. Photo-mechanical effects in azobenzene-containing soft materials. *Soft Matter*, 3(10):1249, 2007.

[20] Filippo Fabbri. *Déformation photoinduite dans les films minces contenant des derivés d'azobenzene: effets de polarisation, effets de proximité et effets de contact*. PhD thesis, Ecole Polytechnique, 2009.

[21] N. K. Viswanathan, S. Balasubramanian, L. Li, S. K. Tripathy, and J. Kumar. A detailed investigation of the polarization-dependent surface-relief-grating formation process on azo polymer films. *Jap. J. Appl. Phys. Part 1*, 38(10):5928–5937, 1999.

[22] F. Fabbri, D. Garrot, K. Lahlil, J. P. Boilot, Y. Lassailly, and J. Peretti. Evidence of two distinct mechanisms driving photoinduced matter motion in thin films containing azobenzene derivatives. *The Journal of Physical Chemistry B*, 115(6):1363–1367, 2011.

[23] Almeria Natansohn, Paul Rochon, Mei-Sing Ho, and Chris Barrett. Azo polymers for reversible optical storage. 6. poly [4-[2-(methacryloyloxy) ethyl] azobenzene]. *Macromolecules*, 28(12):4179–4183, 1995.

[24] N. Landraud, J. Peretti, F. Chaput, G. Lampel, J. P. Boilot, K. Lahlil, and V. I. Safarov. Near-field optical patterning on azo-hybrid sol-gel films. *Appl. Phys. Lett.*, 79(27):4562–4564, 2001.

[25] Peter Karageorgiev, Dieter Neher, Burkhard Schulz, Burkhard Stiller, Ullrich Pietsch, Michael Giersig, and Ludwig Brehmer. From anisotropic photo-fluidity towards nanomanipulation in the optical near-field. *Nature materials*, 4(9):699–703, September 2005.

[26] Antonio Ambrosio, Lorenzo Marrucci, Fabio Borbone, Antonio Roviello, and Pasqualino Maddalena. Light-induced spiral mass transport in azo-polymer films under vortex-beam illumination. *Nature communications*, 3:989, January 2012.

[27] Antonio Ambrosio, Pasqualino Maddalena, and Lorenzo Marrucci. Molecular model for light-driven spiral mass transport in azopolymer films. *Physical Review Letters*, 110(14):146102, April 2013.

[28] Kevin G. Yager and Christopher J. Barrett. *Amorphous Azobenzene Polymers for Light-Induced Surface Patterning*, pages 145–175. John Wiley & Sons, Inc., 2008.

[29] J. Kumar, L. Li, X. L. Jiang, D. Y. Kim, T. S. Lee, and S. Tripathy. Gradient force: The mechanism for surface relief grating formation in azobenzene functionalized polymers. *Appl. Phys. Lett.*, 72(17):2096–2098, 1998.

[30] V Toshchevikov, M Saphiannikova, and G Heinrich. Microscopic theory of light-induced deformation in amorphous side-chain azobenzene polymers. *The Journal of Physical Chemistry B*, 113(15):5032–5045, 2009.

[31] K. Yang, S. Z. Yang, and J. Kumar. Formation mechanism of surface relief structures on amorphous azopolymer films. *Physical Review B*, 73(16):165204, 2006.

[32] Naoki Inoue, Manabu Nozue, Osamu Yamane, and Shinsuke Umegaki. Driving force for formation of a surface relief grating on an azobenzene-containing polymer. *Journal of Applied Physics*, 104(2):023106, 2008.

[33] P. Lefin, C. Fiorini, and J. M. Nunzi. Anisotropy of the photo-induced translation diffusion of azobenzene dyes in polymer matrices. *Pure And Applied Optics*, 7(1):71–82, 1998.

[34] O. Baldus and S.J. Zilker. Surface relief gratings in photoaddressable polymers generated by cw holography. *Applied Physics B*, 72(4):425–427, 2001.

[35] Thomas Garm Pedersen, Per Michael Johansen, Niels Christian Rømer Holme, P. S. Ramanujam, and Søren Hvilsted. Mean-field theory of photoinduced formation of surface reliefs in side-chain azobenzene polymers. *Phys. Rev. Lett.*, 80(1):89–92, 1998.

[36] Y Gritsai, L M Goldenberg, O Kulikovska, and J Stumpe. 3D structures using surface relief gratings of azobenzene materials. *Journal of Optics A: Pure and Applied Optics*, 10(12):125304, December 2008.

[37] S Yang, K Yang, L Niu, and R Nagarajan. Patterning of substrates using surface relief structures on an azobenzene-functionalized polymer film. *Advanced . . .*, (8):693–696, 2004.

[38] Aleksandr Kravchenko, Andriy Shevchenko, Victor Ovchinnikov, Arri Priimagi, and Matti Kaivola. Optical interference lithography using azobenzene-functionalized polymers for micro and nanopatterning of silicon. *Advanced Materials*, 23(36):4174–4177, 2011.

[39] Seungwoo Lee, Hong Suk Kang, and Jung-Ki Park. High-resolution patterning of various large-area, highly ordered structural motifs by directional photofluidization lithography: Sub-30-nm line, ellipsoid, rectangle, and circle arrays. *Advanced Functional Materials*, 21(10):1770–1778, May 2011.

[40] Hong Suk Kang, Seungwoo Lee, and Jung-Ki Park. Monolithic, hierarchical surface reliefs by holographic photofluidization of azopolymer arrays: Direct visualization of polymeric flows. *Advanced Functional Materials*, 21(23):4412–4422, December 2011.

[41] Hong Suk Kang, Seungwoo Lee, Sol-Ah Lee, and Jung-Ki Park. Multilevel micro\nanotexturing by three-dimensionally controlled photofluidization and its use in plasmonic applications. *Advanced materials (Deerfield Beach, Fla.)*, pages 1–8, July 2013.

[42] Jean-Pierre Abid, Michel Frigoli, Robert Pansu, Jacob Szeftel, Joseph Zyss, Chantal Larpent, and Sophie Brasselet. Light-driven directed motion of azobenzene-coated polymer nanoparticles in an aqueous medium. *Langmuir*, 27(13):7967–7971, 2011.

Chapter 2

Sample fabrication and experimental setup

2.1 Fabrication of the photochromic films

The samples we use in this study consist of a photochromic layer coated with either a metal layer or a layer of nanoparticles (NPs). The photochromic layer is a polymeric thin film grafted with azobenzene-derived molecules. We take advantage of the photo-induced mass transport in this layer to elaborate arrays of surface structures and to manipulate NPs deposited there upon. In this section, we present the fabrication of the photochromic layer and the surface patterning process. We will discuss the metal deposition method which consists the first step in our study of the optical and plasmonic properties of metal/polymer hybrid thin films. The deposition of NPs will be described in the chapter dedicated to the study of the photo-induced motion of NPs.

2.1.1 Azobenzene molecules

The photochromic layer is a polymeric matrix incorporated with an azobenzene derivative of the pseudo-stilbene family, the Disperse Red 1 (DR1), which is represented in **Figure 2.1**. The presence of the electro-donor (N(C_2 H_5)(C_2 H_4 OH)) and electro-acceptor (NO_2) groups para-substituted in the phenyl rings causes the partial superposition of the trans and cis isomers absorption spectra [1]. Besides, the lifetime of the thermal relaxation from cis to trans is relatively short [2], therefore contributes to the trans $\rightarrow$ cis $\rightarrow$ trans cycling of the molecules. For thin film fabrication, the photochrome molecules are inserted into either mineral or organic matrices. The organic matrix is obtained from commercially available PMMA-DR1 (polymethilmethacryalte polymer backbone grafted with molecules of Disperse Red 1

(DR1) azobenzene derivative). The mineral matrix is a silica backbone obtained using a sol-gel process.

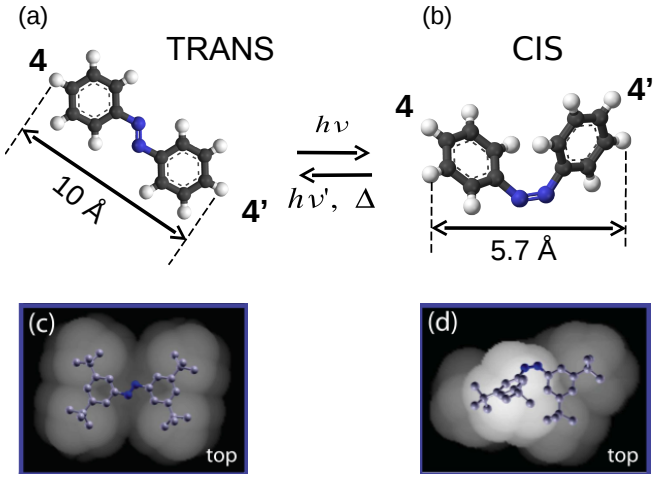

Figure 2.1: (a,b) Azobenzene isomers: Trans & Cis. (c-d) Azobenzene molecule incorporated in a material matrix.

2.1.2 Polymeric film preparation

We use commercially available PMMA-DR1 compound presented in **Figure 2.2**. The DR1 unit is grafted to the polymer backbone in a molar concentration of 15%. The compound comes in form of a red powder. We dissolve this powder into dichloromethane in a proportion of $25mg$ of PMMA-DR1 to $1mL$ of dry dichloromethane (obtained ideally through distillation). The solution is next filtered with $0.45\mu m$ sieve to remove residual particles and then deposited by spin-coating on a clean substrate at $4000rpm$ during $80s$. The substrates we used are made of either glass or silicon. The films obtained are typically $250nm$ thick.

The films obtained by the above process exhibit a surface roughness of about $0.5nm$ (see **Figure 2.3** (a)). In some cases, we have observed a large number of pinhole-like defects of $20nm$ depth and $500nm$ width (see **Figure 2.3** (b)). It has been reported that such defects are formed by the non-complete removal of solvent after the deposition process [3]. In our case, such pinhole-like defects are observed when dichloromethane is still hydrated or when the spin-coating time is too short. Thus the evacuation of water or other residual volatile substance, such as dichloromethane, after the deposition is crucial in controlling the formation of surface pinhole defects.

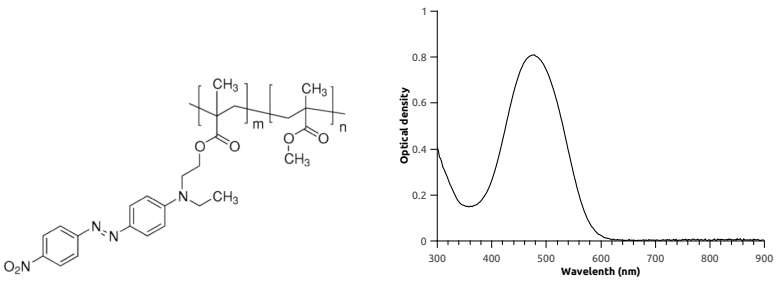

(a) (b)

Figure 2.2: PMMA-DR1. (a) Azobenzene molecule grafted as a side-chain to the polymer backbone. (b) The absorption spectrum of a PMMA-DR1 film showing the absorption band $400nm - 600nm$ associated with the photomerization of azobenzene.

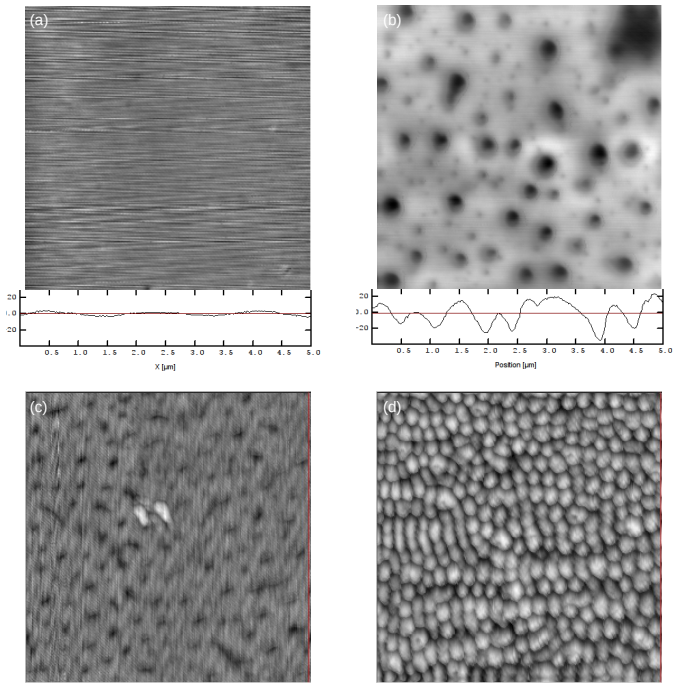

Figure 2.3: PMMA-DR1 film obtained by spin-coating at $4000rpm$. (a) Spin-coating during $80s$. (b) Spin-coating during $20s$, the film presents pinhole defects. (c) PMMA-DR1 solution is contaminated by water, the final film present defect pinhole defects. (d) Sample (c) upon exposure to a laser beam $\lambda = 488$ of power $10mW/mm^2$ during 30 minutes

2.2 Scanning near-field optical microscope

We are interested in the interaction between light and objects and how they influence the optical field distribution. Therefore, it is crucial to obtain simultaneously the physical shape of the objects and the optical field distribution in its proximity. The size of the objects of interest is usually comparable to the optical wavelength of the active light which is in the visible to near infrared range ($400nm - 1100nm$). In these conditions, conventional optical microscopy is not adapted since its resolution is diffraction limited. Indeed, the so-called Rayleigh's criterion asserts a lower limit to the lateral resolution of the conventional optical imaging instrument, due to the diffraction of the optical components, namely:

$$\Delta x = \frac{0.61\lambda}{nsin(\theta)} \qquad k_x = \frac{2\pi}{\lambda} nsin\theta \tag{2.1}$$

where

λ is the wavelength of light in vacuum

n is the optical index of the medium in which the experiment is embedded

θ is the half aperture angle of the objective, $nsin(\theta)$ represents therefore the numerical aperture of the microscope

Δx is the minimal distance between two discernible points on the object plane

In 1928, E. H. Synge pointed out that the resolution limit imposed by diffraction could be circumvented by working with the evanescent instead of the progressive wave. His original approach involved the use of a sub-wavelength light source, for instance a hole in a perfectly opaque screen, to illuminate a sample at a close enough distance and register the scattered light [4]. Indeed, the small source-to-sample distance brings into interaction the studied object and the evanescent light and the fingerprint of this process is contained in the scattered progressive light. This is because the evanescent wave possesses a complex wavevector component in the normal direction to the surface, the absolute value of its in-plane wavevector $\mathbf{k}_{\parallel}$ is no longer limited by the one of the propagative light in the surrounding medium:

$$k_{\parallel}^2 + k_{\perp}^2 = k_0^2 = \left(n\frac{2\pi}{\lambda}\right)$$

where n is the optical index of the medium in which the experiment is immersed, $k_{\parallel}$ and $k_{\perp}$ are the normal and the in-plane components of the wavevector, respectively. The large $k_{\parallel}$ carries information on the high frequency modulation of the surface, even higher than that of the incident light, which explains the high spatial resolution of the near-field microscopy. In theory, the resolution is only limited by the size of the probe [5].

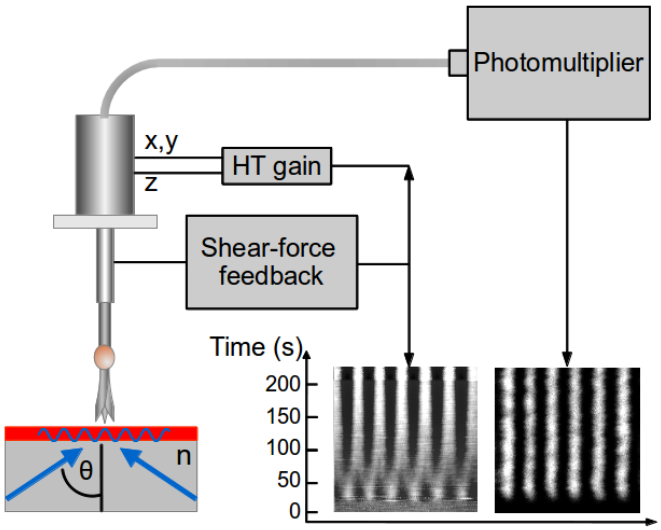

Figure 2.4: Scanning near-field optical microscopy (SNOM).

Since the evanescent field only extends to a distance of the order of a fraction of the wavelength (or of the observed object's size) from its source, all the difficulty relies on maintaining the probe-to-sample distance in the relevant range and on the detection of the usually low signal. One had to wait until 1984 to see the first optical near-field experiment in the visible range by Pohl and the coworkers [6]. In the meantime, other local probe techniques, such as Atomic Force Microscopy, or Scanning Tunnelling Microscopy, have been developed allowing to attain atomic resolution [7]. The realization of the first optical near-field microscopy experiment was largely thanks to the instrumental progress brought about by these two techniques. Practical issues prevent optical near-field microscopy to ultimately reach resolution much smaller than the working wavelength, this technique is mandatory to study the interaction between objects and the optical field at submicroscopic scale, which is of great importance in nanophotonics and nanotechnology.

In this work, we used a home-made scanning near-field optical microscopy (SNOM). The system makes use of a tapered optical fiber fabricated using a home-developed heat-pulling process. The probe-to-sample distance is controlled by shear-force feedback. The optical signal is scattered and guided inside the optical fiber and measured using photon counting to avoid additional noise in the signal amplification. By raster scanning the probe over the sample surface, one is able to simultaneously acquire a topographic image and an optical image.

This section reviews the principles and the characteristics of our home-made microscopy system. We begin by presenting the probe fabrication

process. This is followed by a description of the implementation of the shear-force feedback. Finally, we describe the photon counting technique.

2.2.1 Probe fabrication

The nano-probe is obtained by heat-pulling of an optical fiber. The principle of the process is depicted in **Figure 2.5a**. The optical fiber is clamped on two rails and stretched by a constant load. The heating of the fiber is carried out by a $CO2_2$ laser delivering a computer controlled series of laser pulse (ms). This produces a step-by-step pulling of the fiber. The pulling length produced by each pulse is measured with a quadrant photodiode which detects the displacement of the reflection spot of a laser beam from a mirror soldered on one rail. At each step, the next pulse width is calculated in order to maintain constant the pulling length. The pulling is monitored using a video camera mounted with a microscope objective which allows measuring in real-time the fiber diameter.

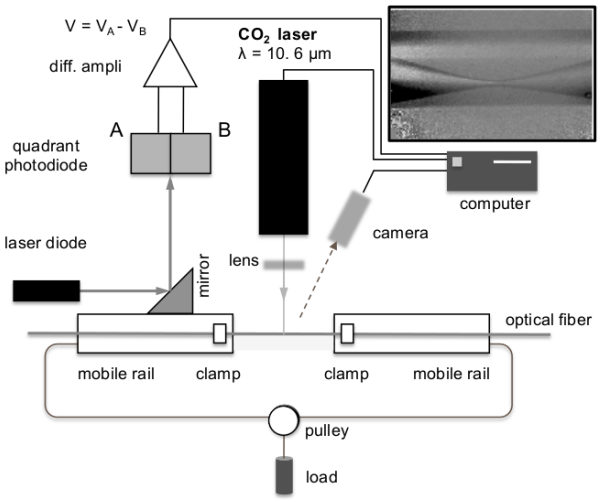

(a)

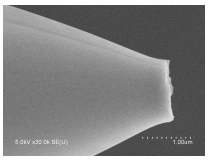

(b)

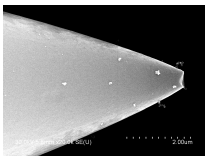

(c)

Figure 2.5: The heat-pulling procedure. (a) The experimental set-up. (b) The tip preformed by heat-pulling. (c) The probe after etching in HF solution

The pulling procedure has been set empirically to obtain, with high

repeatability, tapered optical fiber tips whose diameter may attain $0.5\mu m$ [8]. The apex of the tip is approximately that of a truncated cone. Subsequent chemical etching in HF further reduces the tip apex diameter. The final size of the tip is determined by the concentration of the HF solution, the temperature and the etching time. For example, dipping a preformed tip in HF 25% solution maintained at the triple point of water ($\approx 0.01°C$) results in a tip diameter reduction rate of $4.3nm/s$.

2.2.2 The microscope head

The probe is mounted on the microscope head depicted in **Figure 2.6**. The head combines two piezo tubes, a (x, y, z) scan piezotube ($30 \times 10mm$) and a small dither piezotube ($8 \times 1.3mm$) which oscillates the probe to enable the shear-force feedback system. The fiber is glued into a syringe needle fixed into the dither piezotube. The needle, the dither piezotube and the scan piezotube are held together by Araldite glue. The whole ensemble is fixed on the head body. The probe slides inside the syringe apex and the two piezotubes, and comes out at the back of the head. The tapered extremity is fixed on the syringe apex by means of a wax droplet, while the other end of the fiber is cleaved and connected to a photomultiplier.

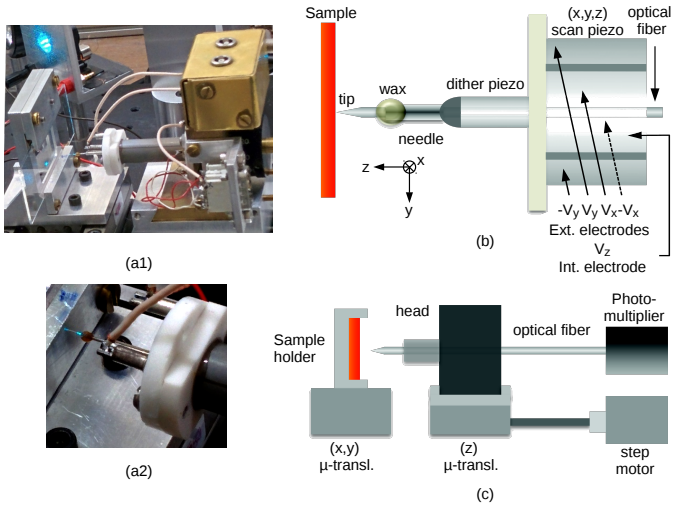

Figure 2.6: The head of the microscope. (a1) The head. (a2) Close look at the extremity of the head, showing the optical fiber tip fixed by a wax droplet on the needle. (b) Schema of the electric connections. (c) Global view.

The (x, y, z) scan piezotube has four external electrodes and one internal electrode, driven by a voltage between 0 and $400V$. Its maximum excursion is about $18\mu m$ along the x, y axes and $2\mu m$ along the z-axis. The head

body is mounted on a translation stage coupled to a step motor. Each step corresponds to a $200nm$ displacement along the z-axis, thus allowing a precise setting of the tip-to-sample distance within the range of the (x, y, z) piezotube extension.

The sample is mounted in front of the tip, on a sample holder equipped with manual translational stages with $10\mu m$ precision along the x and z directions of the sample surface plane. The setting of the tip close to the sample is first achieved by a visually controlled coarse approach, bringing the tip to about $10\mu m$ to the sample surface, and subsequently, by an automatic approach based on the shear-force feedback described below, bringing the tip to $1\mu m$ to the sample surface, i.e. within the excursion range of the scanning piezotube.

2.2.3 Feedback mechanism/Shear-force microscopy

The probe is raster scanned above the sample surface while its distance to the sample surface is kept constant. This is achieved by shear-force feedback which measures the damping of the tip oscillation at resonance when it comes within the atomic force interaction range with the sample surface. Since in our set-up, the tip is vibrated in plane parallel to the median plane of the surface, the interaction produces a shear force on the tip. The extent of the shear-force, as measured in [8], is of about $1.6nm$ giving thus access to the nanoscopic scale sensitivity. The tip can therefore be maintained at about $1nm$ to the surface and dip into the optical near-field which extends upto hundreds of nanometers into the surrounding medium.

Tip-surface distance detected via shear-force damping

The tip and dither piezo tube is oscillated by means of an alternating voltage V_0 applied to the dither piezo tube. When the whole system of dither piezotube, syringe needle and tip oscillates, the resonant properties can be modelled by a compound pendulum system whose resonant frequencies depend the length of each component. The resonant frequencies associated with the tip is given by to the tip-ending free length L, for the $i-th$ harmonic frequency f_i, by the equation:[1]

$$f_i = \frac{{k_i}^2}{2\pi}\sqrt{\frac{EI}{\rho S}}\frac{1}{L^2} \tag{2.2}$$

where

E is the Young modulus of the fiber

I is its inertia moment

ρ is the material density

[1] See for example [9]

S is the fiber cross section
$k_i = \alpha_i L$ where α_i is solution of:

$$cosh(\alpha_i L).cos(\alpha_i L) + 1 = 0$$

We drive the tip-ending free length of the optical fiber at its first harmonic.[2] The fundamental vibration mode gives a very strong mechanical constraint and a large vibration amplitude.

Dimensioning of the electric components

In electronic terms, the dither piezotube behaves mainly like a capacitor. The oscillations of the piezotube itself or other elements that it carries (the needle and the tip) impose mechanical constraints on the tube that can be detected as a change in its capacitance. The rate of change of the capacitance is modified when the oscillation is damped by the shear-force. To further increase the sensitivity, we drive the piezotube at the resonant frequency of the tip.

The balanced Wheatstone bridge circuit is a convenient tool with great sensitivity to measure such a change in the piezotube capacitance. The change in the capacitance unbalances the bridge and produces an output signal related to the amplitude and the phase of the vibration of the tip-piezo tube system with respect to the input signal. There exists another method based on the measurement of the deviation of a reflected beam from the fiber. However, we prefer the Wheatstone bridge method for two reasons: first, it limits optical disturbance to other optical measurement and allows to obtain a more compact microscope head; second, the optical detection is affected by the displacement of the head during the scan.

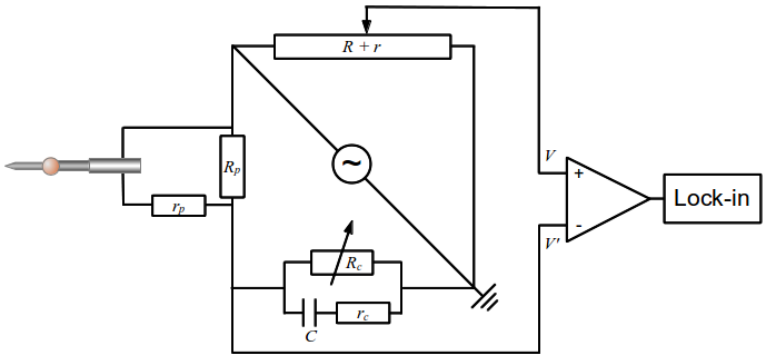

Figure 2.7: Wheastone bridge set-up to detect the oscillation of the dither piezotube

The Wheatstone bridge circuit, depicted in **Figure 2.7**, consists of two branches driven by a common input signal V_0. The voltage measured be-

[2]The tip-ending length is of about $3mm$

tween the midpoints of the branches is called the bridge voltage. One branch contains the piezotube which is equivalent to a non-ideal capacitor.[3] The parasitic resistance suffers thermal drifts. At a low working frequency, a lower resistance R_p is placed in parallel to eliminate its effect on the circuit. The value of R_p is chosen high enough to be shorted by the piezotube impedance ($Z_p = \frac{1}{C_p\omega}$) in the frequency range of interest (typically above $10kHz$). The thermal dissipation on the piezotube is accounted for by a small resistance r_p in series with the piezotube. On the counterpart of this branch is an equivalent circuit consisting of R_c, r_c and C. The other branch is purely resistive, constituting of a potentiometer $(R + r)$. The total resistance $(R + r)$ is chosen large enough to limit the current flowing into this branch, but low enough to limit the thermal noise compared to the full scale resonance signal. Detailed information on the values of each component is given in [10] (page 29).

Bridge balancing

The bridge is balanced far from the tip-piezotube resonances. Only at resonance a significant voltage is measured on the bridge, allowing to further increase the sensitivity. This is achieved by adjusting $R + r$ and R_C following these steps:

- Set the two potentiometer $R + r$ and R_C at about their midpoint to avoid short circuit.
- Drive the bridge at the highest frequency accepted by the lock-in ($120kHz$) and adjust the $R + r$ potentiometer to minimize the output signal. Under this condition, the current flow principally through the piezotube and C, the capacitive impedance is thus balanced.
- Drive the bridge at low frequency ($10Hz$ is reasonable) and adjust R_C in order to minimize the output signal. Under this condition, the current flows predominantly through R_p and R_C, the resistive impedance of the detection branch is thus balanced.

Signal conditioning for the feedback

At resonance, the bridge voltage is proportional to the change of the piezotube capacitance:

$$\Delta V \approx \frac{\Delta C_p}{2C_p} V_0$$

When approaching the tip to the sample surface, shear-force damping modifies the rate of change of the capacitance C_p. This damping depends on the tip-to-sample distance. Therefore, the bridge signal depends on this

[3] A capacitor in parallel with a large resistance to account for the leakage current.

distance and can be modelled by [11]:

$$\Delta V = \Delta V_R \left[1 - exp\left(-\frac{d}{d_0}\right)\right] \tag{2.3}$$

where d is the tip-surface distance, $d_0 \approx 1.6nm$ is the characteristic shear-force interaction distance [8], ΔV_R is the bridge voltage when the tip is at infinite distance to the surface which is practically the bridge voltage when it is at d_0.

The position of the tip is controlled by the scan piezotube whose elongation depends on the applied voltage V_z. In first order approximation:

$$z = \gamma |V_z|$$

Hence:

$$\Delta V = \Delta V_R \left[1 - exp\left(\frac{V_z - V_{surf}}{V_0}\right)\right] \tag{2.4}$$

where V_{surf} is the voltage required to approach the tip into contact with the surface and $V_0 = \frac{d_0}{\gamma} = Cte$.

This signal, amplified through a gain $G = 100$, serves as the input of the electronic feedback loop whose purpose is to maintain a constant bridge signal. During tip scanning above the sample surface, the surface relief manifests as a change of V_{surf}. The feedback loop consists of maintaining $V_z - V_{surf}$ (hence, ΔV) constant via the control of V_z.

Electronic implementation of the feedback loop

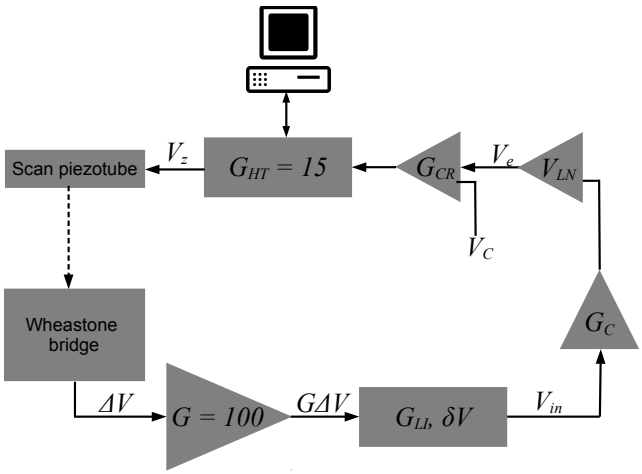

Figure 2.8: Schema of the feedback electronics.

A schema of the feedback loop is given in **Figure 2.8**. The bridge signal is an a.c. voltage at the resonance frequency of the free fiber end. The signal entering the feedback loop is a d.c. voltage V_{in} proportional to the

amplitude of $(\Delta V - \Delta V_R)$. It is obtained by demodulating ΔV in Lock-in amplifier:

$$V_{in} = G.G_{LI}.\Delta V_R.exp(\frac{V_z - V_{surf}}{V_0}) + \delta V$$

This voltage is amplified by the lock-in gain $1/G_C$ and input into a logarithmic amplifier allowing to extract V_z from the exponential. The δV was added into the above expression to assure non-zero input at the logarithmic gain resulting in oscillation of the feedback loop. The logarithmic amplifier compares the signal to a fixed voltage V_C and output $V_{LN} ln\left(\frac{V_C}{V_{in}G_C}\right)$ where V_LN is constant. We call the output of the logarithmic amplifier V_e. This signal is again amplified by a feedback gain G_{CR} and the goal now consists of maintaining V_e close to zero by adjusting V_z, i.e.:

$$\begin{aligned} 0 &= G_{CR}V_{LN} ln\left(\frac{V_C}{V_{in}G_C}\right) \\ &= G_{CR}V_{LN} ln\left[\frac{V_C G_C}{GGLI\Delta V_R} exp\left(-\frac{V_z - V_{surf}}{V_0}\right)\right] \\ &= G_{CR}V_{LN}\left[ln\left(\frac{V_C G_C}{GGLI\Delta V_R}\right) + \frac{V_{surf} - V_z}{V_0}\right] \\ &= G_{CR}V_e \end{aligned} \tag{2.5}$$

G_C can be manually adjusted to modify the median tip-to-surface distance. Decreasing of G_C increases this distance and vice versa.

Finally, to obtain a two dimensional topographic image, the tip is raster scanned in two directions, one fast and one slow, the feedback control is divided into fast and slow components. The fast component provides the surface topography and the slow one is used to set the average tip position. This is implemented in the electronic set-up in the G_{CR} which is the combination of two low-pass filters of different cut-off frequencies:

$$G_{CR} = \left[\frac{G_{fast}}{1 + i\omega\tau_{LI}}\right]_{\omega \ll \tau_{LI}^{-1}} + \left[\frac{G_{slow}}{1 + i\omega\tau_{slow}}\right]_{\omega \ll \tau_{slow}^{-1}}$$

The G_{slow} gain acting at low frequency ($\tau_{slow} \approx 1s$) is fixed at $G_{slow} = 10$, the G_{fast} gain acts at higher frequencies, τ_{LI} is the time constant of the lock-in (τ_{LI} is practically $10ms$). G_{fast} is adjusted manually to adapt the sensitivity of to the specific imaging purpose. Pratically, for a constant input signal, the higher is G_{fast}, the higher is the applied reaction voltage V_z. The higher limit of the tip's sensitivity is set by the value above which the tip start to oscillate in the z direction.

The overall feedback loop is implemented via a modified commercial STM electronics fabricated by Park Scientific Instruments (STM-SU2-210

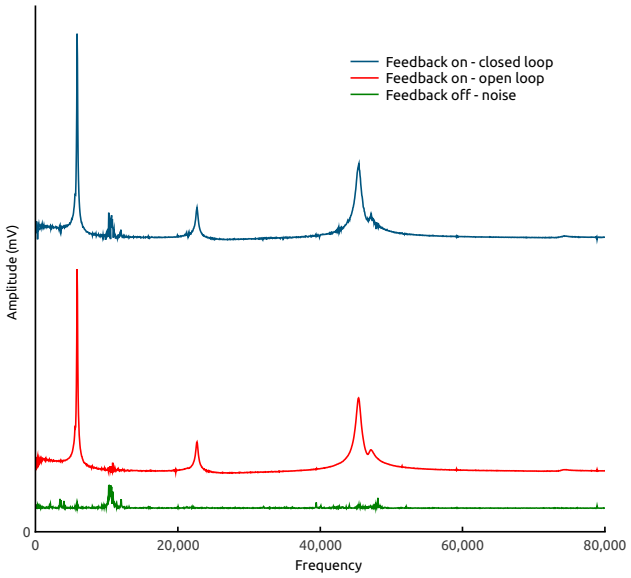

Figure 2.9: Noise spectrum of the shear-force probe.

and SPC-400, 1992). Data are recorded using a home-developed Labview 7.1^{TM}routine, which also generates the (x, y) scan voltages. Topography images are stored into a 256×256 matrix, in binary file format.

Response spectrum and working frequency

The tip is driven at its first harmonics. Under this condition, the oscillation amplitude of the tip is about $10nm$ which defines the lateral resolution of the microscope. The oscillation frequency of the tip is adjusted by changing its free length ($f = \alpha L^{-2}$). Experimental data give $\alpha \approx 600mHz$ for our microscopy system [10]. When choosing the oscillation frequency of the tip, one must avoid the oscillation frequency of the piezotube. Its high mechanical rigidity makes it hardly sensitive to the influence of the shear-force applied to the tip.[4]

The working frequency should be chosen to avoid the frequency range where the system is the most coupled to environmental noise. **Figure 2.9** shows typical responses of the microscope head for different configurations:

Feedback electronics off The oscillation of the dither piezotube and the voltage powering the (x, y, z) piezotube are off. In this condition, one measures the inherent noise of the head.

[4]The same observation can be made when comparing our set-up to another set-up in which the tip is fixed on a tune fork and vibrates at the resonant frequency of the tuning fork. Working at the resonance of the tip seems to give better overall sensitivity to the shear-force detection. Atomic step imaging has indeed been achieved with our system as shown in [8].

Feedback electronics on - open loop The dither piezotube is put on oscillation but the (x, y, z) piezotube is off. One observe the resonance of the piezotube and the syringe.

Feedback electronics on - closed loop Condition the closest to the experimental condition.

2.2.4 Optical near-field detection

Optical signal acquisition

The evanescent light at the sample surface is scattered by and partially guided inside the optical fiber to a photomultiplier tube (PMT). When the photodetector of the PMT, made of $GaAs$, receives a photon of energy larger than its bandgap, an electron/hole pair is generated and the photoexcited electron is emitted into the vacuum. In order to minimize thermionic electron emission, the PMT is kept in contact with a thermostat kept at $-70°C$ by dry ice. The signal carried by the emitted electrons goes through seven successive dynodes which multiplies the number of incident electron by a factor of 10. Thus, the signal arriving at the anode consists of a pulse of approximately 10^7 electrons. The PMT output also contains pulses generated by thermoionic electron coming from the intermediate dynodes causing a background noise, also called dark noise. For the detection of low signal, this dark noise should be eliminated by using photon counting technique. In fact, the PMT signal pertaining to an incident photon, as previously mentioned, is a well-defined pulse of $\sim 10^7$ electrons. The dark noise passing through fewer dynodes is less amplified and is hence weaker by orders of magnitude. One can thus eliminate the dark noise by simply putting a threshold to the output signal. The selected pulses are then converted to TTL form and transported to the dedicated counting device. In our set-up, the TTL pulses are acquired via a National Instrument DAQ. The same Labview 7.1^{TM}routine in each time interval required for the acquisition of a topographic pixel counts the number of TTL pulses received, normalized into the number of pulses per second and store into a 256×256 matrix, in a binary file. One thus obtains for each scan the simultaneous topographic and optical images of the sample surface.

Specificity of optical near-field detection

The following points should be kept in mind when one interprets the near-field images:

Tip asymmetry The fabrication process described in Section 2.2.1 produces asymmetric tips. In particular, the light intensity captured by

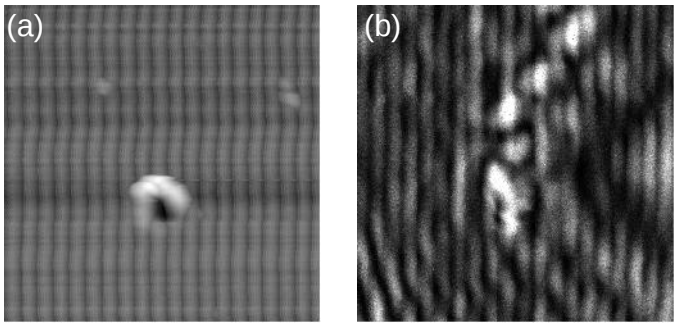

Figure 2.10: Parasitic optical diffraction due to a surface defect. (a) Topographic image of a metal grating presenting a defect. (b) Near-field optical image of the surface in (a) showing the effect of the defect on the collected near-field.

the tip depends on the incident angle of light with respect to the tip axis. When imaging an interference pattern produced by two beams, this may result in a reduced effective intensity contrast. The solution is to choose the orientation of the tip to capture equally the light coming from each interfering beam. In concrete terms, we use a clean glass plate as a sample and project an interference pattern on the surface. Next, the tip is approached to a few μm to the surface. We then measure, for each interfering beam, the light collected for various azimutal orientations of the tip. The tip captures the most effectively each beam at opposite orientations. Turning the tip 90° from one of these orientations puts the tip in the configuration to capture equally light from the two interfering beams. More detail on this procedure can be found in [10].

Polarization dependency The asymmetry of the tip also makes its detection capability depend on the light polarization. This is more difficult to correct since the polarization difference varies with incidence angle and whether the detection is in far-field or near-field (this is related to the change of the detection cross section which will be discussed in the following paragraph.) An ultimate solution would require coating the tip with an opaque metallic layer, leaving a well-defined aperture at its extremity. The truncated conic shape of our tip makes it relatively simple to obtain such metallic coating through thermal evaporation at an oblique angle while rotating the tip. The detail of this procedure is reported in [12]. In all of our near-field measurements, we used non metalized tips, the interpretation of the results taking into account the polarization dependency will be provided on purpose.

Effective cross section The tip couples the external light field to its internal guided mode. The coupling process depends critically on the exact portion of the tip where the coupling takes place. For a non metallic-coated tip, light can couple to the internal mode at the extremity or on the side. Thus the coupling efficiency depends strongly on the field profile, for instance, the tip detects differently a Gaussian beam and an evanescent field.

Parasitic diffraction The detection of a near-field optical signal requires a clean sample surface to avoid parasitic optical diffractions, see **Figure 2.10**.

2.3 Conclusion

We have described the fabrication method of the photochromic films as well as the characterization of their morphology. We have also reviewed the principle of our shear-force/SNOM measurement system. The feedback mechanism and the probe made of tapered optical fiber are the central elements of the microscopy technique and have been discussed.

Bibliography

[1] Jan F Rabek. *Photochemistry and photophysics*, volume 4. CRC Press, 1991.

[2] C Barrett, A Natansohn, and P Rochon. Cis-trans thermal isomerization rates of bound and doped azobenzenes in a series of polymers. *Chemistry of materials*, 7(5):899–903, 1995.

[3] N.G. Semaltianos. Spin-coated pmma films. *Microelectronics Journal*, 38(6–7):754 – 761, 2007.

[4] EH Synge. Xxxviii. a suggested method for extending microscopic resolution into the ultra-microscopic region. *The London, Edinburgh, and Dublin Philosophical Magazine and Journal of Science*, 6(35):356–362, 1928.

[5] D. Courjon and C. Bainier. *Le champ proche optique.: Théorie et applications*. Collection technique et scientifique des télécommunications. Springer, 2001.

[6] D. W. Pohl, W. Denk, and M. Lanz. Optical stethoscopy: Image recording with resolution $\lambda/20$. *Applied Physics Letters*, 44(7):651–653, 1984.

[7] Gerd Binnig, Heinrich Rohrer, Ch Gerber, and E Weibel. Surface studies by scanning tunneling microscopy. *Physical review letters*, 49(1):57, 1982.

[8] Philippe Bertrand. *Microscopie optique en champ proche. Réponse optique à l'échelle submicronique*. PhD thesis, Ecole Polytechnique, 1999.

[9] S.S. Rao and F.F. Yap. *Mechanical Vibrations*. Always learning. Prentice Hall, 2011.

[10] Filippo Fabbri. *Déformation photoinduite dans les films minces contenant des derivés d'azobenzene: effets de polarisation, effets de proximité et effets de contact*. PhD thesis, Ecole Polytechnique, 2009.

[11] Damien Garrot. *Étude par microscopie en champ proche des phénomènes de migration de matière photo-induite dans les matériaux photochromiques*. PhD thesis, Université Paris-Sud Orsay, 2006.

[12] N. Landraud, J. Peretti, F. Chaput, G. Lampel, J. P. Boilot, K. Lahlil, and V. I. Safarov. Near-field optical patterning on azo-hybrid sol-gel films. *Appl. Phys. Lett.*, 79(27):4562–4564, 2001.

Chapter 3

Photo-induced transport of nanoparticles on the surface of an azo-polymer thin film

3.1 Introduction

Thin films containing azobenzene derivative present the spectacular properties of photo-induced mass transport which has been demonstrated by the photo-inscription of surface relief gratings [1, 2]. The mass transport takes place over a distance of the order of microns which is much larger than the size of the azobenzene molecules themselves. This opened up the perspective of using azobenzene-containing films to convert directly light energy into mechanical work, (see the photomodulation of the water contact angle [3, 4], the optical bending and unbending of a free standing azopolymer film [5] or the light driven motion of an oil droplet on a monolayer of azobenzene [6]). In this chapter, we are interested in harnessing the property of photo-induced matter transport of azo-containing films to put into motion nanoparticles (NPs).

The conventional methods for matter transport at nanoscale involve either a nanosize microscopy probe or the optical trapping, also known as optical tweezers. The approach with the nanoprobe consists of using a scanning microscope's probe to address one by one the nano-objects. Since the interaction between the probe and objects is tunable, for instance, by controlling the voltage applied on the former, one can use the probe to catch, carry and release the nanobject at specific places. This approach is however hardly scalable since the nanoobjects are addressed sequentially. Using the probe to move the nanoobjects also presents the risk of damaging the probe and consequently the quality of the microscopy image.

On the other hand, optical tweezers work since transparent particles with a higher refractive index than their surrounding medium are attracted towards the region of maximum laser intensity [7]. By moving the focus of the laser beam, it is possible to transport dielectric particles. However, high-power focused laser is usually required with the risk of affecting the nature of objects under examination [8].

A novel approach pursued by Watanabe *et al.* in 1999, reproduced in **Figure 3.1** consists of using the photo-induced deformation of photosensitive material, such as urethane-urea azo copolymer. A compactly packed monolayer of monodispersed polystyrene spheres is deposited on the surface of a urethane-urea azo copolymer film through a self-assembly process. The sample is next irradiated by a laser beam ($\lambda = 488nm$, power density of $5mW/mm^2$) through the monolayer of NPs which acts as a mask in this process. A surface pattern is revealed after rinsing the NPs whose shape and size depend on the geometry of the NPs. The irradiation must be in the absorption band of the azobenzene units of the thin film to produce the surface pattern. The patterning of the surface is explained by a model based on the competition between the gradient force of the induced optical near-field of monodispersed polystyrene spheres and the radiation pressure. In practical terms, there is a relative penetration of the NP into the sample surface which is triggered by the irradiation in the absorption band of the azobenzene derivatives.

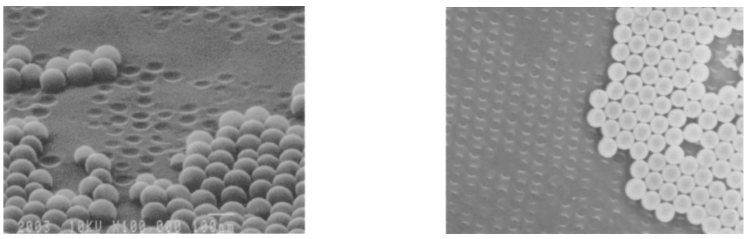

(a) (b)

Figure 3.1: Imprint of polystyrene spheres deposited on an azofilm after illumination. SEM images of azofilms covered by (a) $100nm$ spheres and (b) $500nm$ spheres. The samples are exposed to laser light (power $5mW/mm^2$ and wavelength $\lambda = 488nm$). Image courtesy of [9].

In this chapter, our goal is to use the direct conversion of light energy to mechanical force occurring in azobenzene containing thin films to achieve nano-objects transport with nanoscopic precision. Watanabe's experiment rises the following questions: how does the surface deformation depend on the illumination parameters (angle of incidence, polarization, intensity) and could it be employed to induce a NP's movement. We hence will address

these questions in a series of experiment on the systems of NPs deposited on an azopolymer surface. Allowing to take simultaneous topographic and optical images of the sample surface, the SNOM is the most adapted tool for this study.

The chapter is organized as follow: first, we will discuss our experimental set-up based on local probe technique, then we will investigate the behaviour of two types of NPs (gold and polystyrene) deposited on azobenzene containing films, by playing with the relative orientation of the vectors **E** and **k**.

3.2 Experimental set-up and sample preparation

3.2.1 Experimental set-up

Figure 3.2 shows schematically our experimental set-up. The sample is mounted in front of the SNOM tip. A blue laser ($\lambda = 488nm$, beam size $1mm$) is used to induce photo-isomerization of azobenzenes. Its polarization is controlled by a half-wave plate which performs a polarization change in negligibly time ($10s$) compared to the image scan time ($86.46s - 256s$). The incident beam, divided by a beam splitter cube, can follow two different optical paths (denoted by path 1 and path 2) before impinging on the sample surface at variable angle of incidence. Topographic and optical images of the sample surface are taken in real time during the irradiation. We refer to the sample side facing the SNOM tip as the front side or the front surface whereas the opposite side of the sample as the rearside or the rear surface.

The scan piezo of the microscope is subjected to drift resulting in relative spatial shifts of the imaged area. A yardstick is required to track down the change in the position of the NPs. For this purpose, a red laser beam ($\lambda = 650nm$, out of the absorption band of the azofilms) is used to project an optical pattern on the same surface. The mechanical stability between the light sources and the sample is verified by the photopatterning experiments. Empirically, the vibration magnitude is much smaller than $100nm$ since surface patterns with pitches equal to $200nm$ can be realized (reported in the previous chapter). SNOM image of the red laser spot on a glass surface confirms the stability of the red wavefront pattern during the timescale of the experiments. The NPs used in this study are not larger than $100nm$ in diameter and they are well separated to reduce disturbance to the red optical pattern. The optical pattern comes from the inhomogeneity of the sample substrate and from the laser beam itself. In cases where the spontaneous surface structures induced by the blue laser may disturb the red pattern, we take advantage of these defects as landmarks on the sample surface. An adapted optical filter is used to eliminate the optical signal due to the blue

laser.

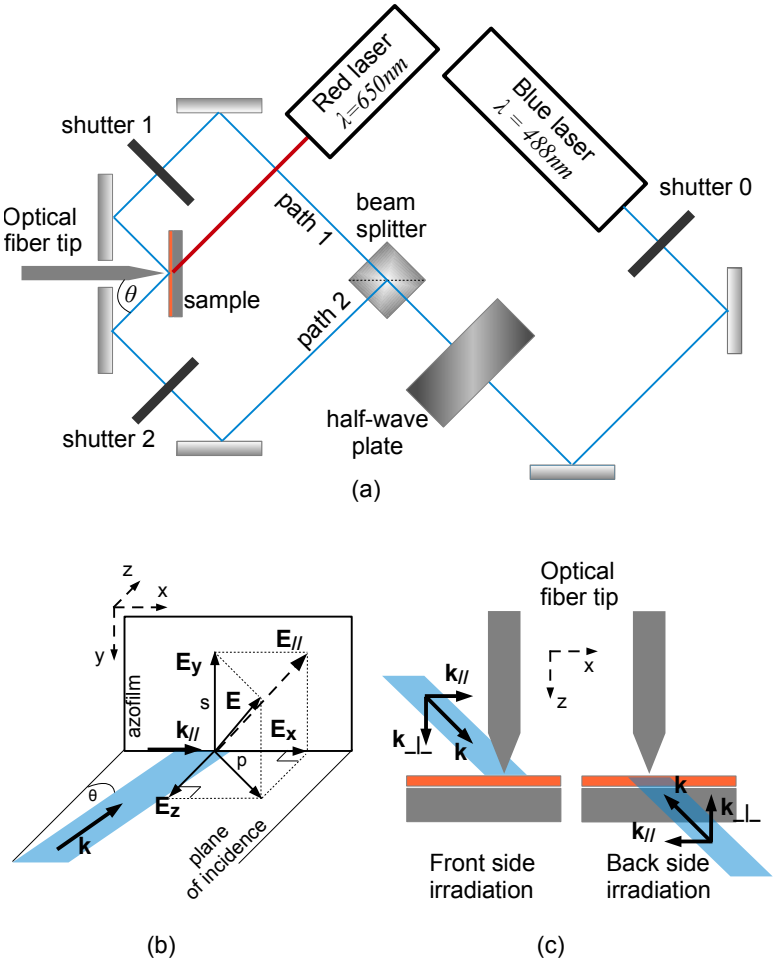

Figure 3.2: Experimental set-up. (a) The optical and microscopy set-up. (b) Geometry at the sample surface: θ angle of incidence, $\mathbf{E}_{\|}$ in-plane component of the incident polarization, s polarization is given by the component $\mathbf{E_y}$, p polarization is characterized by the two components ($\mathbf{E_x}$, $\mathbf{E_z}$), 45° oriented polarization has 3 components ($\mathbf{E_x}$, $\mathbf{E_y}$, $\mathbf{E_z}$). In our experimental configuration $\theta = 45°$, meaning that $E_x = E_z$ for p and 45° oriented polarizations. (c) Front side irradiation and rearside irradiation.

3.2.2 Details of the NPs

We use commercial-available $50nm$-diameter gold spheres (Au NPs) and $100nm$-diameter polystyrene spheres (polystyrene NPs). These NPs are diluted in ethanol solution and spin-coated ($3000rpm$ during $30s$) on the desired substrate. The solution concentrations are chosen so that the sample surfaces are covered with about 1 NP per μm^2 which is sufficient for imaging purpose with the SNOM and is small enough to minimize disturbance to the red laser pattern. The preparation of the solutions is slightly different for Au and polystyrene NPs.

- **Au NPs**

  The monodispersed $50nm$-diameter Au NPs are initially diluted in water. The Au NPs are first extracted by centrifugation and then diluted in ethanol with twice the initial concentration to obtain to solution for spin-coating.

- **Polystyrene NPs**

  The commercial $100nm$-diameter polystyrene NPs are initially diluted in ethanol. The initial concentration is reduced, by diluting $25\mu l$ of the initial solution into $10ml$ of ethanol, to obtain the spin-coating solution.

3.3 The route towards NP's motion

3.3.1 Moving NPs on glass substrate

We first consider NPs spread on a raw glass substrate. **Figure 3.3** (a) shows an SEM image of the sample surface revealing the monodispersed polystyrene NPs of diameter equal to $100nm$ well separated from one another. We irradiate the sample with a blue laser beam and concurrently perform shear-force microscopy. Under this condition, it is highly difficult to obtain reliable topographic images of good quality, a typical topographic image is shown in Figure 3.3 (b) showing several trails blurring the NPs.

By following line by line the image scan process, we can identify the nature of these parasitic trails. Topographic images are obtained by raster scan, each image is constructed from the scan lines showing the successive topographic profiles. In these scan lines, the shape of the parasites and the NPs are identical. Besides, the parasites often disappear when the slow scan is reversed. This suggests that the parasite are taken out of the imaged area by the tip. It is thus reasonable to attribute the trails to the NPs as being displaced by the shear-force tip. The true scale representation of the

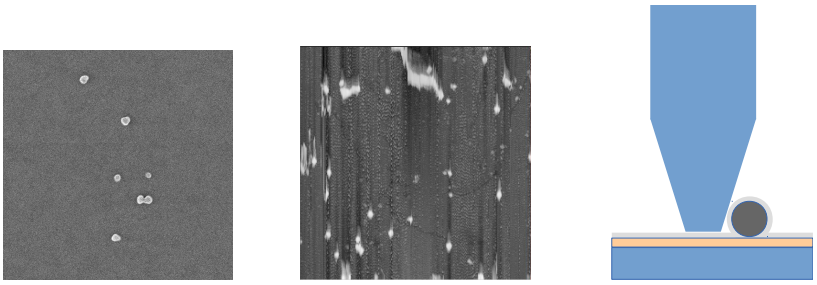

(a) (b) (c)

Figure 3.3: Polystyrene nanoparticles of diameter $100nm$ deposited on a clean glass substrate shown in (a) $4\mu m \times 4\mu m$ SEM image, (b) $10\mu m \times 10\mu m$ shear-force topographic image. (c) Tip-particle interaction

tip and a nanoparticle given in Figure 3.3 (c) supports this vision. The tip and the substrate are both made of glass and thus can exert equally strong interaction with the NPs. This is further evidenced by the dark stripes appearing next to a NP when the latter replaces a image a parasite in the image succession (see **Figure 3.3** (b)). In fact, the previous SEM imaging of this sample requires the deposition of a $6nm$-thick Au layer.[1] The NPs, moved by the tip, sweep away the Au cover and produce the dark stripes seen in the topographic image in **Figure 3.3** (b).

Concerning the light-nanoparticles interaction, we do not observed any evidence of such process for the irradiation as large as $40mW/mm^2$. This interaction, if exists, is so small that it is hidden by the disturbance of the tip.

3.3.2 Moving NPs on azobenzene-containing thin films

We first consider NPs on a PMMA-DR1 thin film. Without other notification, the substrate is composed of a $200nm$ thick PMMA-DR1 film supported by a glass substrate. **Figure 3.4** (a) shows the SEM image of a sample coated with $100nm$-diameter polysterene spheres. There is an appreciable variation in the size of the NPs indicating an aggregation phenomenon. This should be kept in mind in the interpretation of the latter light-induced phenomena. **Figure 3.4** also shows the shear-force images (this time without the Au cover) of the surface in dark (b) or under $2.4mW/mm^2$ irradiation from the blue laser. In dark, the shear-force image (b) also presents the trails caused by NPs being dragged by the tip. But under blue irradiation,

[1] The sample surface was non-conductive, a metallic cover is required avoid charge accumulation due to the electronic irradiation. The Au deposition were performed by $Ar+$ plasma sputtering

the obtained topography image shows well-defined NPs.

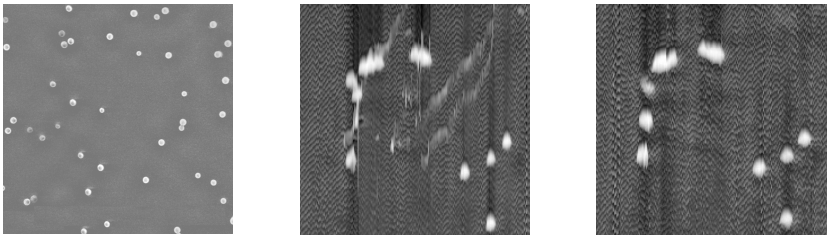

(a) (b) (c)

Figure 3.4: Polystyrene NPs of diameter $100nm$ deposited on PMMA-DR1/glass substrate shown in (a) $4\mu m \times 4\mu m$ SEM image, (b) $4\mu m \times 4\mu m$ shear-force image without irradiation and (c)$4\mu m \times 4\mu m$ shear-force image with irradiation

The same phenomenon is observed on PMMA-DR1 thin film coated with Au NPs. **Figure 3.5** (a) shows the SEM image of a sample having $50nm$-diameter Au NPs. The corresponding shear-force images of a sample of the same batch are shown in **Figure 3.5** (b), taken in dark, and (c) taken under $2.4mW/mm^2$ blue laser irradiation. While the tip drag is present in (b), image (c) shows distinct white spots associated with the NPs. The PMMA-DR1 film under irradiation prevents the dragging of the NPs by the tip.

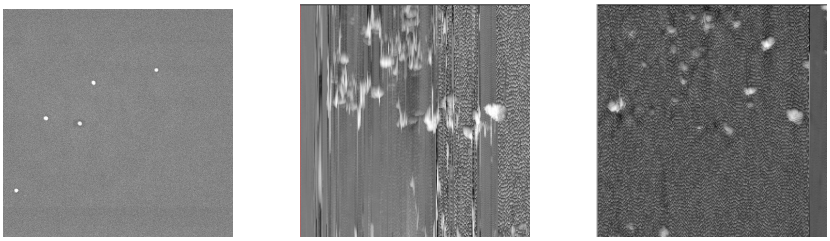

(a) (b) (c)

Figure 3.5: Au nanoparticles of diameter $50nm$ deposited on PMMA-DR1/glass substrate shown in (a) $4\mu m \times 4\mu m$ SEM image, (b) $5\mu m \times 5\mu m$ shear-force image without irradiation and (c)$5\mu m \times 5\mu m$ shear-force image with irradiation

First conclusion

At this level of investigation, we can draw the conclusion that NPs are not dragged by the tip motion when enlightening the azopolymer

film. Somehow, NPs are stuck on the surface during the illumination which means that the surface of the photosensitive film acquires some viscosity under blue light illumination.

3.3.3 Moving NPs on "weakly" photoresponsive azo sol-gel thin film

Let us consider now an intermediate situation in which the NPs are deposited on the surface of an azofilm which is "weakly" photoresponsive. It means that the film is rigid enough to almost inhibit the photo-induced surface patterning. For this purpose, we use DR1 grafted silica films obtained from sol-gel process. The rigidity of the sol-gel film is achieved by controlling the reticulation degree. The photoactivity of the azobenzene molecules is preserved throughout the process as shown by the UV-visible transmission spectrum. The sol-gel films are about $350nm$ thick.

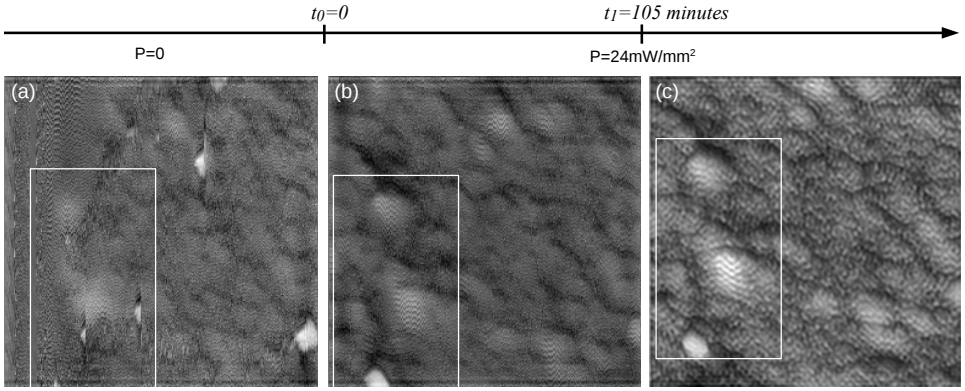

Figure 3.6: Series of $5\mu m \times 5\mu m$ shear-force images of a sample containing a polystyrene nanoparticle on $350nm$-thick sol-gel-DR1 thin film. The sample is irradiated by a laser beam of power density $24mW/mm^2$ under 45°-polarization at 45°. (a) The irradiation is off (b) First image under irradiation. (c) Image after 105 minutes of continuous irradiation. Each image is taken in $85s$.

Figure 3.6 shows three topographic images of the surface of the sol-gel-DR1 film coated with polystyrene NPs, taken (a) in dark, (b) under $24mW/mm^2$ blue laser irradiation at the initial time, and (c) after 105 minutes of irradiation. The laser beam is 45°-polarized and impinges on the surface at 45°. These images recorded on the same sample area present a small drift of the microscope tip which can be corrected by comparing the surface corrugation. The imaged area in (c) is slightly shifted compared to

the area in (b) as visualized by the white-border rectangle. In image (a), we see several white spots associated with the polystyrene NPs. Some of them disappear after a first scan (image (b)) and a new NP shows up at the bottom of the white-border rectangle, probably deposited by the tip. We focus next on the area enclosed by the white-border rectangle in image (b) and (c). The irradiation helps to retain the NP on the surface throughout the scanning process (105 minutes). Moreover, the relative position between the NP and the surface corrugation does not change between the images (b) and (c).

Second conclusion

We can conclude that when the photo-induced mass transport is mostly inhibited, we do not observe light-driven NP transport on azo-containing film.

3.3.4 NP's burying upon photo-isomerization of PMMA-DR1 thin film

We now go back to the system with NPs deposited on PMMA-DR1 thin film. As shown by Watanabe *et al.*, surface patterning are expected to develop beneath polystyrene NPs upon azobenzene photo-isomerization.[2] The shape and the size of these structures are linked to the ones of the NPs. In this section, we present an *in situ* study of this phenomenon using the experimental set-up shown in **Figure 3.2**. The polystyrene NPs loaded PMMA-DR1 sample is irradiated by *s*-polarized blue laser beam impinging on the sample surface at $\theta = 45°$ from the front side (containing the nanoparticles). The angle of incidence must be out of normal to leave enough space for the microscopy set-up. The *s* polarization allows also to reproduce around the NPs the same electric field profile as in the study of Watanabe *et al.*.

Figure 3.7 shows the evolution of polystyrene NPs coated PMMA-DR1 film under irradiation by an *s*-polarized $2.4 mW/mm^2$ laser beam of $\lambda = 488nm$ impinging the sample surface at $\theta = 45°$. In the image (a1) taken in dark, we observe again the drag phenomenon on the NPs caused by the microscope tip. When the irradiation is turned on (image (a2)), NPs can be clearly distinguished in image (a2). [3] The subsequent images (a2-6) reveal

[2] In their study, the polystyrene NPs are assembled in a compactly packed monolayer on the surface of azofilm. The photo-isomerization is next excited by illuminating the sample through the NP mask. The surface, after the NPs being rinsed, present structure associated with the NPs lattice

[3] Note that the irradiation intensity now is 10 times smaller than the one used in the experiments involving weakly photoresponsive azofilm or glass substrate.

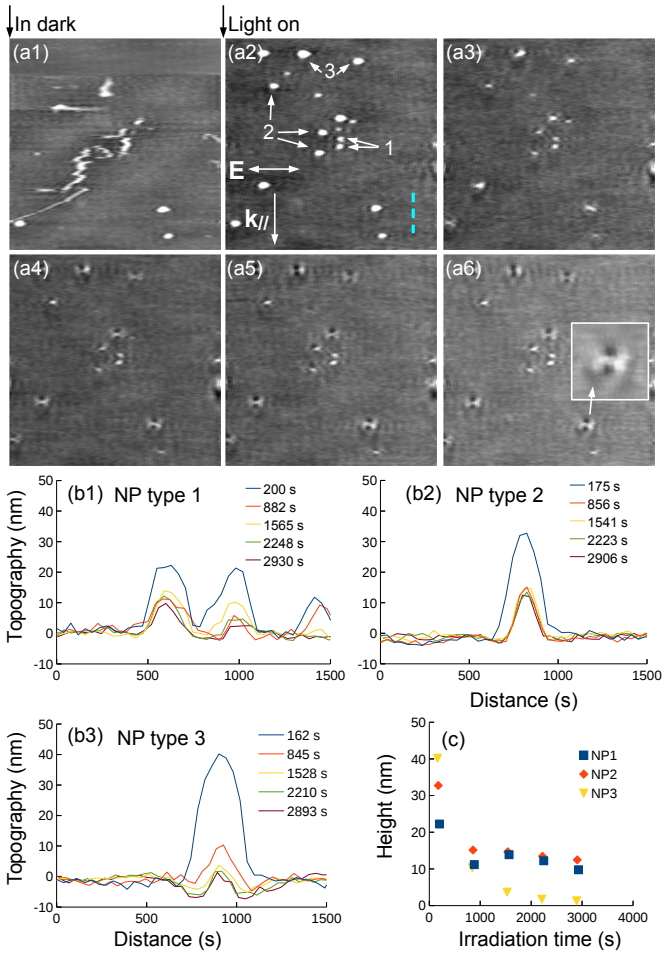

Figure 3.7: "Sinking" of polystyrene NPs into PMMA-DR1 surface upon exposure to irradiation of s-polarized $2.4mW/mm^2$ laser beam of $\lambda = 488nm$ at 45°. (a1-6) $10\mu m \times 10\mu m$ shear-force images showing the time-evolution of the sample surface. The light polarization $\mathbf{E}$ and the in-plane wavevector $\mathbf{k}_{||}$ are indicated in (a2). The NPs are classed into 3 types according to their penetration. (b1-3) Surface profiles across the center of the NPs of type 1, 2 and 3, respectively, taken in the direction of the blue dashed line in (a2). (c) time-evolution of the NPs' height.

a so far unseen phenomenon in our experiments, the penetration of the NPs into the azofilm. We can class the NPs in (a2) into three types according to their final appearance. Considering the NPs of type 1, the penetration manifests as a reduction in lateral size, seen in the topographic images, and height, evidenced by the profile plot (b1). The same observation can be made for the NPs of the type 2. In addition, one sees around these NPs

the appearance of surface deformations. Lobes are formed in the direction of **E** accompanied by depletion of surface matter on the remaining sides of the NPs. The surface profile across a NP of type 2 in (b2) shows small grooves on both sides of the NP. This phenomenon is more prominent for NPs of type 3. In image (a5-6) the NPs become even smaller than their lobes. The profile plot (b3) shows two grooves of $5nm$ depth on both sides of the NP which only emerges of $1nm$ above the surface. The NPs of the type 3 exhibit complete immersion into the film. The level of penetration seems to depend on the size of the NPs. The time-evolution of the NPs size plotted in (c) shows that the NPs of type 1 and 2 reach about the same height above the surface whereas the NPs of type 3, initially the largest, are almost completely buried into the film.

The polystyrene NPs on PMMA-DR1 film in our experiment show much larger immersion than in Watanabe's report [9] in which the NPs only penetrate into the film by at most half of their diameter. Apart from the difference of the photosensitive film, the compact packing of the NPs in Watanabe *et al.*'s work may contribute to prevent the NPs from immersing further into the film. Watanabe *et al.* also propose a theoretical model based on the gradient force theory to explain the surface imprint observed in their experiment [9]. However, this model only predicts a surface growth as high as half of the NP's diameter. The formation of lobes and grooves around the NPs may have the same origin as the near-field surface patterning described in [10–12] in which the mass transport takes from area where the optical electric field is parallel to the surface to the area where it is perpendicular.

The same study is carried out on Au NPs deposited on PMMA-DR1 thin film. The results are shown in **Figure 3.8**. When the laser's power density is the same as in the experiment on polystyrene NPs ($2.4mW/mm^2$), after $1792s$ the NPs' height drop from $50nm$ to $30nm$ with no appreciable surface deformation. Comparing to the polystyrene NPs, over the same time, their heights drop down to less than $20nm$ from the initial value of $100nm$, some of them are surrounded by surface lobes. We next boost up the laser by 10 to $24mW/mm^2$ during $512s$. Now we see two lobes develop around the Au NPs along the direction of **E**. These lobes have narrower forms than the lobes seen around polystyrene NPs while no matter depletion is seen on the remaining sides of the Au NPs. In the profile plot in (b) corresponding to the images (a3-4), the NP is a little raised due to a surface spontaneous deformation underneath this NP.

We conclude that the increase in the laser power density boosts the surface deformation but does not accentuate the penetration of the Au NPs into the film. Under s-polarized irradiation, the Au NPs show less penetration under than the polystyrene NPs. This is in part predictable from the results

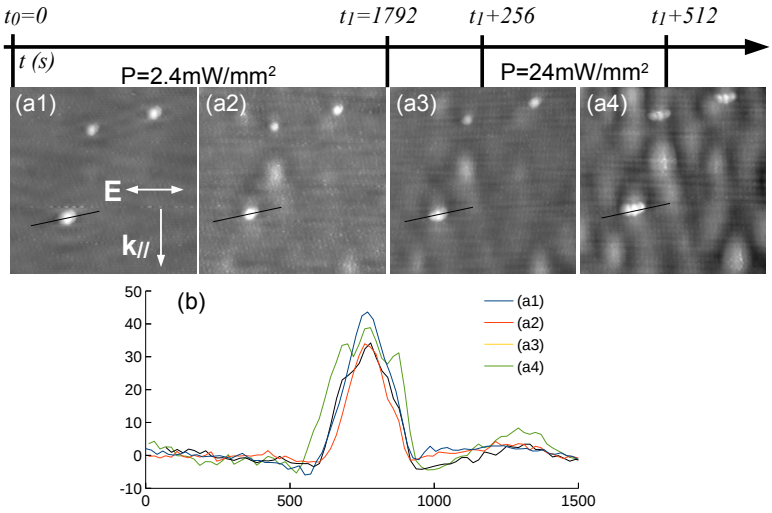

Figure 3.8: *Au* NPs on PMMA-DR1 surface under s-polarized irradiation. The irradiation power density is intially $2.4mW/mm^2$and after $1752s$, it is increased ten-fold. (a) $3\mu m \times 3\mu m$ shear-force images taken at the indicated time. The light polarization $\mathbf{E}$ and the in-plane wavevector $\mathbf{k}_{||}$ are indicated in (a1). (b) Plot of the surface profiles along the black line across one of the NPs

on size dependence of the penetration of the polystyrene NPs. However, the more localized shape of the lobes and the absence of the matter depletion on the other sides of the NPs may signify other subtle mechanism of the surface patterning process.

Azobenzene-containing thin films covering metal NPs have been employed to visualize the Localized Surface Plasmons Resonance (LSPR) of the latter.[13] Our results shows that NPs surface pattern also develop around metal and dielectric NPs when they are on top of the azofilms.

3.4 Directional movement of the NPs

The photo-isomerization of the PMMA-DR1 film under *s*-polarized irradiation induces the burying of the NPs accompanied by the appearance of two surface deformations aligned along the light polarization. It is thus interesting to observe the behaviour of the NPs under different light polarizations. The studied samples consists of spherical NPs, $50nm$-diameter *Au* or $100nm$-diameter polystyrene, deposited on PMMA-DR1 thin films on glass substrate. The samples is illuminated by collimated laser beam having ($\lambda = 488nm$, at an angle of incidence $\theta = 45°$ if no other notification is

given).

3.4.1 *Au* NPs

We first investigate samples coated by *Au* NPs. Since the irradiation wavelength $\lambda = 488nm$ is within the Localized surface plasmon resonance (LSPR) range of the *Au* NPs, we expect strong near-field scattering which would amplify the nanoparticle-mediated light matter interaction.

The illumination configuration is depicted in **Figure 3.2**b. The laser beam is 45°-polarized with the intensity $2.4mW/mm^2$ and impinges on the sample surface from the front side. The in-plane projection of the polarization $\mathbf{E}_{\parallel}$ makes 54° with respect to the plane of incidence. **Figure 3.9** presents a series of $5\mu m \times 5\mu m$ topographic images obtained while the sample is under irradiation. The time required to scan each image is $256s$. The time between consecutive images is $512s$. The whole image serie is acquired in $1h20'$.

We can identify two kinds of topographic features. The first one is the optically induced spontaneous growth of surface defects. Their existence, size and shape depend on the PMMA-DR1 thin film under study. These defects are recognizable since they only appear under irradiation and stay immobile. The grid system is attached to one of the defects. The 2nd type of topographic object is *Au* NP. In this experiment, all the protrusions (NPs and defects) appear as a pair of particles because of the imperfection of the used tip. Nevertheless, the obtained images are good enough to evidence a gradual change in the relative positions of the *Au* NPs with respect to the cross hair throughout the images. The in-plane components of the polarization $\mathbf{E}_{\parallel}$ and of wavevector $\mathbf{k}_{\parallel}$ are indicated by the arrows in **Figure 3.9**(a). We note that the movement of the NPs is closely parallel to the in-plane component $\mathbf{E}_{\parallel}$ and the movement direction makes an angle of 48° with $\mathbf{k}_{\parallel}$.The movement is given by $\mathbf{k}_{\parallel}$ since the in-plane polarization is a spatial oscillating vector. We observe that all the NPs move with the same speed in the same direction. The directional movement exhibits thus a collective feature.

Third conclusion

We can qualitatively interpret the directional motion of *Au* NPs using Watanabe's model. The near-field of the NPs (probably enhanced by the LSPR effect of *Au* NPs) induces the surface deformation underneath NPs. An asymmetric near-field pattern induces an asymmetric surface deformation beneath the NPs and provides a "push" toward the direction of smaller surface deformation. This model thus explains the

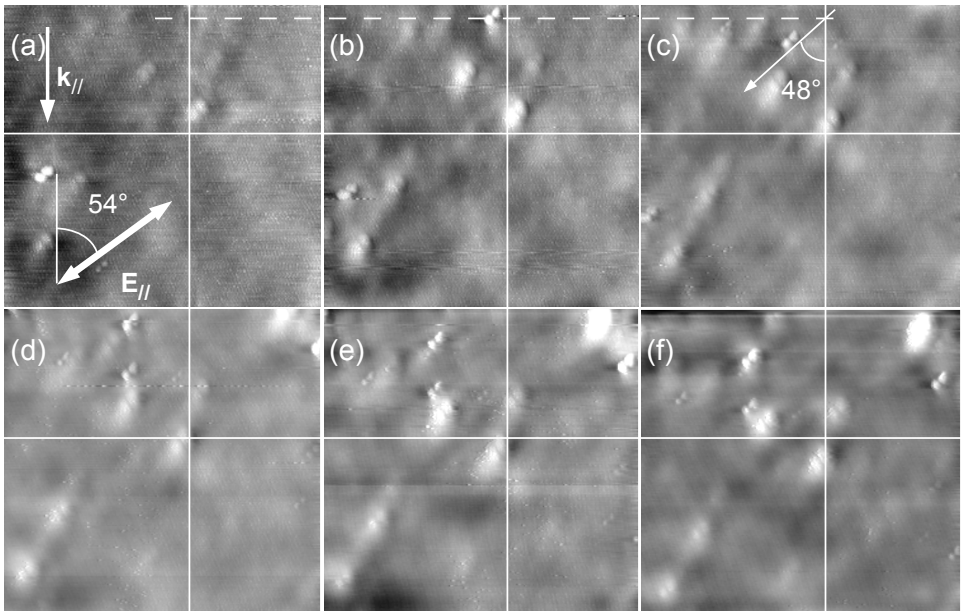

Figure 3.9: Directional movement of Au NPs ($\phi = 50nm$) on PMMA-DR1 film under 45°-polarized irradiation. $2.4mW/mm^2$ 45°-polarized laser beam of $\lambda = 488nm$ impinges on the surface at 45°. The series of $5\mu m \times 5\mu m$ shear-force images show the evolution of the Au NPs on the sample surface over time. The image scan takes $256s$. The NPs have a double feature due to the large apex of the tip. The in-plane component of the electric field $\mathbf{E}$ and of the wavevector $\mathbf{k}_{\parallel}$ are indicated in image (a). The cross-hair is attached to a surface defect. The movement direction is indicated by the arrow in (c).

dependence on the light polarization $\mathbf{E}_{\parallel}$ and wavevector $\mathbf{k}_{\parallel}$. The identical movement of the NPs would be the result of their similar shape. To check this interpretation, we need to perform the same experiment on dielectric polystyrene NPs which do not exhibit field enhancement associated with the LSPR. According to our arguments, we should expect to observe a much weaker directional movement.

3.4.2 Testing the third conclusion with polystyrene NPs

Our sample is the same as the one presented in **Figure 3.4** presenting both isolated and aggregated nanoparticles. Since they scatter differently the incident light, they are expected to exhibit different movements under irradiation.

In **Figure 3.10**, we report a series of $5\mu m \times 5\mu m$ topographic images of a sample of polystyrene NPs on PMMA-DR1 thin film. The experimental conditions are identical to the previous experiment except that the polarization of the same incident beam is rotated by 90°. The in-plane component of the electric field $\mathbf{E}_{\|}$ and of the wavevector $\mathbf{k}_{\|}$ are indicated in **Figure 3.10** a. The image scanning rate is $85.33s$ per image. The time between two consecutive images is $512s$. The acquisition time for whole series of images is $1h56'$. The cross-hair is fixed with respect to the surface defects but is centered on a NP in (a) to reveal its movement.

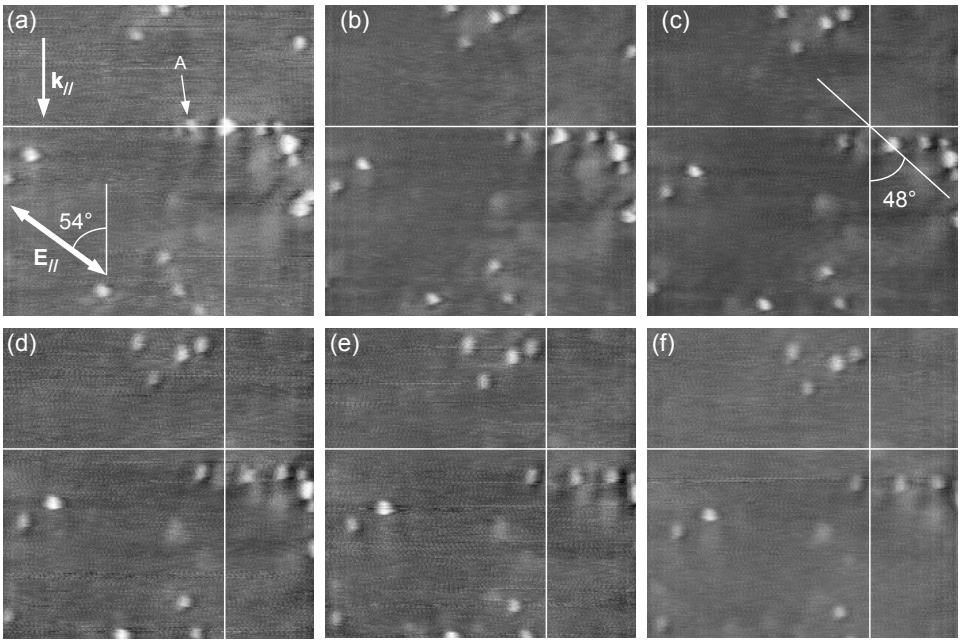

Figure 3.10: Directional movement of polystyrene NPs ($\phi = 100nm$) on PMMA-DR1 film under 45°-polarized irradiation. $2.4mW/mm^2$ 45°-polarized laser beam of $\lambda = 488nm$ impinges on the surface at 45°. The series of $5\mu m \times 5\mu m$ shear-force images shows the evolution of the polystyrene NPs on the sample surface over time. The image scan takes $85.33s$. The in-plane component of the electric field $\mathbf{E}_{\|}$ and of the wavevector $\mathbf{k}_{\|}$ are indicated in image (a). The cross-hair is fixed with respect to the surface defects but is centered on a NP in (a) to reveal its movement.

The image series also reveal a collective movement of the polystyrene NPs. The direction of the movement is closely parallel to the new direction of $\mathbf{E}_{\|}$. The direction of the movement makes an angle 48° relative to the plane of incidence. This is in agreement with our previous remark on the respective roles of these parameters on the direction of the movement. Contrary to our expectation, the movements of the polystyrene and Au NPs are of the same

order. Indeed, the time between two consecutive images is the same for the two series and the NPs exhibit similar change in position between the images. This is better illustrated in **Figure 3.11** (a-b) where we plot the distance travelled by *Au* and polystyrene NPs as a function of time. We further note that despite the size differences of the NPs (isolated or aggregated), they all follow parallel trajectories and their relative distance is preserved throughout the experiment.

Finally, we also observe the penetration of the polystyrene NPs during their movement to a certain extent according to the different NPs. But it is remarkable that the movement is unaffected by the penetration even for the NPs which seem to enter deeply into the film. Such is the case, for instance, for the NP denoted by A in **Figure 3.10**a. During its movement, two lobes develop on its sides in alignment with $\mathbf{E}_{\parallel}$. These lobes have initially the same size. Then, the lobe on the left becomes gradually predominant, it overcomes the NP from image (b) to (c) while maintaining the movement (speed and trajectory) of the primary NP.

Those results suggest that the scattered optical field by the nanoparticles is not the principal mechanism driving the NPs' movement. First, the polystyrene NPs cross the same distance as the *Au* NPs. Second, the movement speed is independent of the NPs' sizes. Third and most importantly, the movement is not influenced by the degree of burying of the NPs into the film. At the beginning of this experiment, all the NPs show a size reduction indicating that they are entering the film. For most of the NPs, their size rapidly stabilized. Part of them is beneath the film surface. Their optical near-field, being dependent on the refractive index contrast between the NPs and its environment, would be modified. However, no appreciable effect is observed. Furthermore, in the case of a complete burying, the photo-induced surface deformation is simply irrelevant to the NPs' movement.

3.4.3 Sensitivity of the NP's motion to the azofilm quality

Before further exploring the influence of the irradiation configuration on the NPs' movement, let us present here a more quantitative account of the NPs' movement under 45°-polarized irradiation.

Figure 3.11a shows the NPs' trajectories. The particles of *Au* and polystyrene follow a straight line inclined by roughly 48.6° with respect to the plane of incidence. This angle is slightly smaller than $(\widehat{\mathbf{E}_{\parallel}, \mathbf{k}_{\parallel}}) \approx 54°$. This is explained by the fact the half wave place rotates the light polarization by about 39.3° instead of the intended angle 45° respect to the plane of incidence. The in-plane projection of the light polarization makes actually an angle of 49° with respect to the x-axis which is in good agreement with our experimental observation.

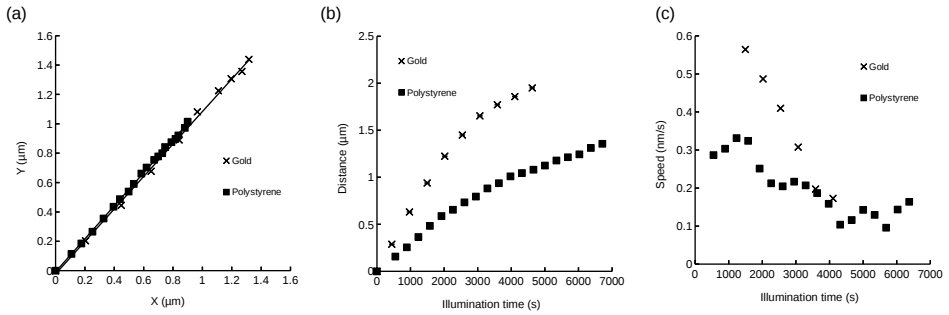

Figure 3.11: Comparison between Au and polystyrene NP's displacement versus time. (a) Under the same irradiation condition, Au NPs and polystyrene NPs follow the same trajectories. (b) Distance travelled by Au NPs and polystyrene NPs as a function of the illumination time. (c) The NPs' speed as a function of the irradiation time.

Figure 3.11 (b) and (c) plot the displacement distance and the speed of the NPs as a function of time. The speed of the NPs is evaluated by the following formula:

$$v = \frac{1}{2}\left(\frac{s_{i+1} - s_i}{t_{i+1} - t_i} + \frac{s_i - s_{i-1}}{t_i - t_{i-1}}\right)$$

As previously mentioned, the distance travelled by the Au NPs and the polystyrene NPs are of the same order of magnitude. The movement speed decreases with time and the accumulated travelled distance approaches $2\mu m$ for Au NPs and $1.5\mu m$ for polystyrene NPs.

However, this result is dependent on the film itself. For the NPs of the same nature, the movement speed can be up to 3 times larger on one film than on another. The experiment is repeated with polystyrene NPs on another sample under irradiation during more than 8h.[4] The illumination configuration is depicted in **Figure 3.12** (a). To this point, the photo-induced NPs' movement is established, **Figure 3.12** (b) shows the successive position of the NPs on the same topographic image to better visualize their trajectories. Each NP is tagged by a major letters. The numbers indicate the NPs for different acquisition time. The objects denoted by the same number are extracted from the same topographic image. The time between two successive positions is $768s$. One sees clearly that trajectories are identical, the motion speeds are equal (the distance between each pair of number is the same for all the NPs), the trajectories are straight and parallel to one another. They are tilted this time by roughly $48.6°$ with respect to the plane of incidence which is close to the angle of $\widehat{(\mathbf{E}_{\parallel}, \mathbf{k}_{\parallel})} \approx 54°$. The movement

[4]The experiment was carried out overnight.

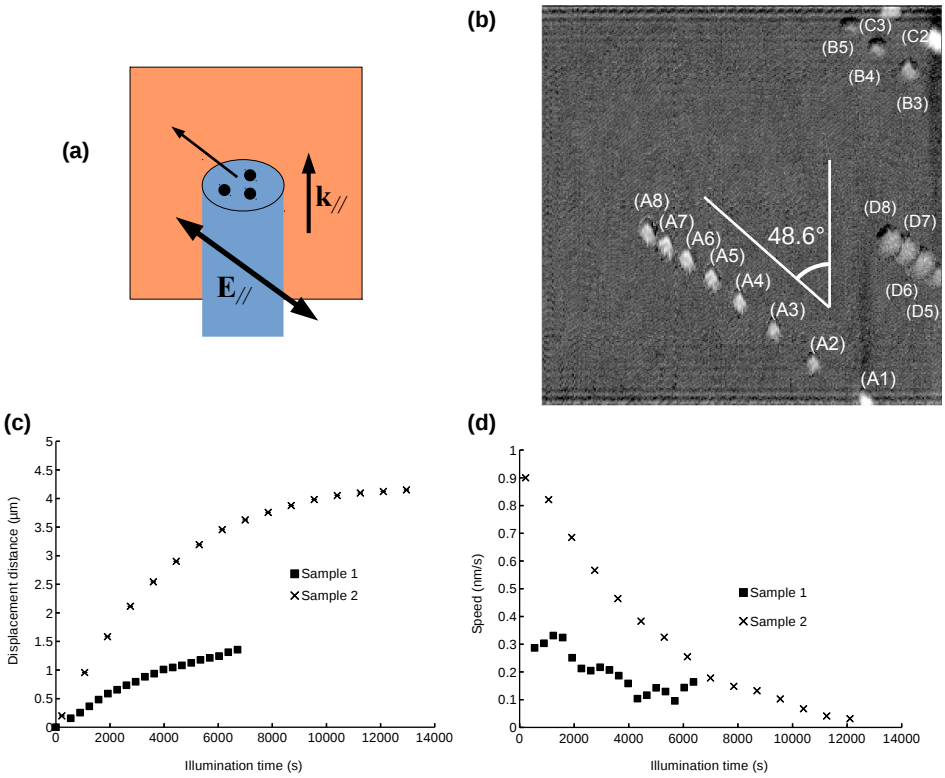

Figure 3.12: Dependence of the polystyrene NPs' motion to the PMMA-DR1 thin films' quality. Sample 1: sample with polystyrene NPs in **Figure 3.11**, sample 2: a different sample coated with polystyrene NPs. The samples are illuminated from the front surface at the angle of incidence $\theta = 45°$ by a 45°-polarized blue laser beam of wavelength $\lambda = 488nm$, power density $2.4mW/mm^2$. (a) The directions of $\mathbf{E}_{\parallel}$, $\mathbf{k}_{\parallel}$ and the NPs' motion. (b) Data taken for sample 2: Polystyrene NPs' position extracted from shear-force topographic images. The successive positions of the NPs are reported on the same image. The objects pertaining to the same NPs are labelled by the same letters and their temporal order is indicated by the numbers. The NPs' positions are measured every $768s$. (c) The displacement as a function of the irradiation time. (d) The dependence of the movement speed on the illumination time.

speed decreases with time resulting in a denser appearance of the NPs at the end of their trajectories. **Figure 3.12** (c) and (d) compare the movement of polystyrene NPs of this sample (sample 1) and of the sample in **Figure 3.11** (sample 2). Between these two samples, it appears a factor 3 in the distance travelled by the NPs during the same time. The movement saturates at about $12000s$ on the sample 1. On the sample 2, the acquisition time is not

sufficient to observe the saturation.

Given that the polystyrene NPs are of the same nature, the difference in their behavior would stem from the properties of the PMMA-DR1 film. One indication of the film's quality is the number of defects. On the sample 2, no photo-induced spontaneous defects is observed during the irradiation suggesting that the PMMA-DR1 film is more homogeneous to give a faster motion of the NPs.[5]

Fourth conclusion

Based on these results, we can assert that the displacement of the NPs comes from the motion of the azofilm itself. The film acts as a conveyor belt for the NPs. This motion depends on the irradiation configuration (the in-plane components $\mathbf{E}_{\parallel}$ and $\mathbf{k}_{\parallel}$) and the film quality but is independent of the electronic properties of the NPs.

3.4.4 Motion dependence on the light polarization components

To single out the role of the polarization components ($\mathbf{E_x}, \mathbf{E_y}, \mathbf{E_z}$) (i.e. for 45° oriented polarization) on the NPs' motion, we carry out an experiment in which the light polarization is changed by 90° during the irradiation. **Figure 3.13** presents the irradiation configuration and two sets of $4\mu m \times 4\mu m$ shear-force images showing the NPs' motion. These images are arranged in two rows, each is obtained under the indicated polarization configuration. The last image of the first set and the first image of the second set are the same. The light polarization is rotated by turning a half-wave plate placed between the light source and the sample. This operation produces some noise visible in these images indicating the moment the polarization changes. In this experiment, a sample coated with Au NPs is used. The laser power density is $2.4mW/mm^2$. Each image is taken in $85.33s$. Two successive images are separated by $512s$. One of the Au NP is marked by a red dot. A grid attached to one of surface defects allows visualizing the NPs' motion.

The first polarization configuration is the same as in the previous experiment involving Au NPs. In the first image set, the Au NPs move along $\mathbf{E}_{\parallel}$. The indicated Au NP moves towards the right bottom of the images, approaching the surface defect on which the grid is attached. The movement direction makes about 49° with respect to the plane of incidence. In the

[5] This complicated the drift correction process. An optical pattern projected by a red laser was used to mark the sample surface.

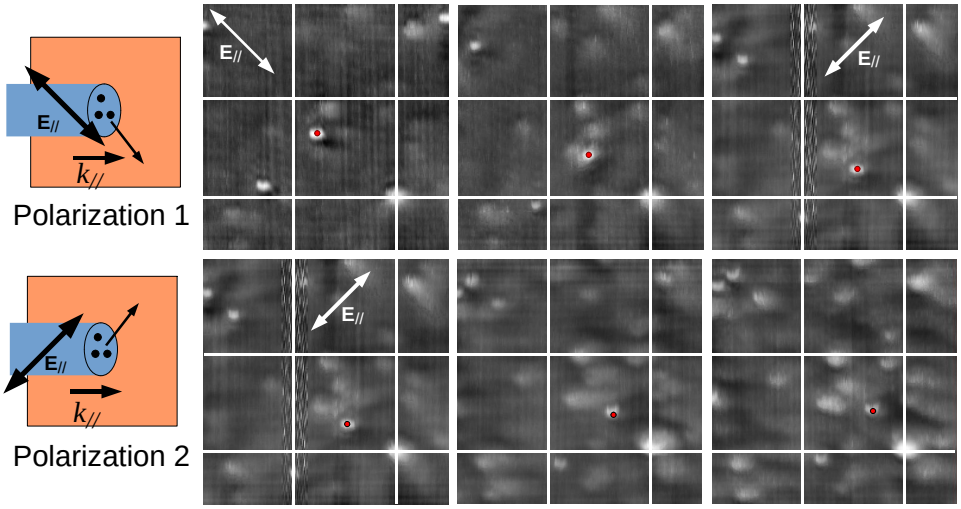

Figure 3.13: Effect of the polarization components on the NPs' motion. Series of $4\mu m \times 4\mu m$ images. The laser (power density $2.4mW/mm^2$) is 45°-polarized. Each image is taken in $85s$. Two successive images are separated by $512s$. The red dot visualizes the motion of a Au NP. The light polarization **E** is rotated by 90° at the last image of the first image line.

second image set corresponding to the second polarization, the Au NPs now move towards the top-right of the images along the new direction of $\mathbf{E}_{\|}$.

The movement direction also makes an angle of about 49° with respect to the plane of incidence. In both cases, the directions of the movement make an acute angle with respect to $\mathbf{k}_{\|}$ of the incident light. The change in the movement direction following the rotation of the incident light polarization strongly confirms the role of the laser polarization on the movement of the NPs.

Let us now compare the NP's motion induced by p and 45° oriented polarized light, both experiments being achieved on the same sample and with the same power density. In **Figure 3.14** (a), the distance crossed by the NP's versus the illumination time is drawn for both polarizations. The motion is faster under p polarization. It is worthwhile to extract from **Figure 3.14** (a) the speed ratio of the motions induced by both polarizations. As shown on **Figure 3.14** (b), the speed ratio, which slightly increases versus time is between 1.35 and 1.45.

Note that under s polarization, no movement is induced on the NPs and that:

$$\frac{E_x^p}{E_x^{45°}} = \frac{E_z^p}{E_z^{45°}} = 1.41$$

We can draw two possible explanations for the dependence of the movement

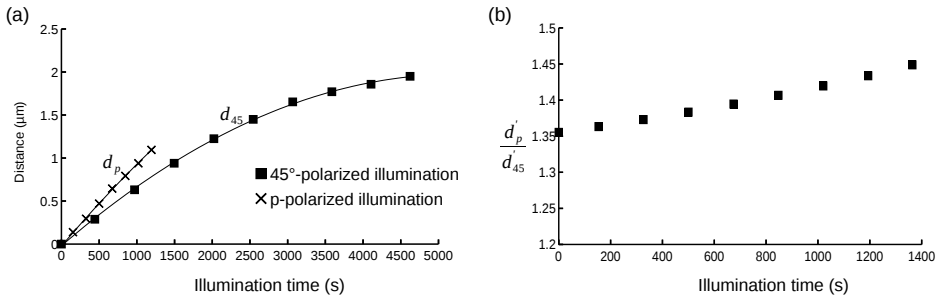

Figure 3.14: Comparison between the movement under p-polarized and 45°-polarized irradiation. The sample is irradiated from the sample's front side. The laser beam $\lambda = 488nm$ of power $2.4mW/mm^2$ irradiated the sample at 45°. (a) Distance crossed by the NPs vursus illumination time. (b) speed ratio for both polarization versus time.

on the polarization of the incident light in attributing the motion either to $\mathbf{E_z}$ or to $\mathbf{E_x}$. Both of these components are zero under s polarization. They are also larger under p polarization than under 45° oriented polarization by the factor 1.41 which is close to the value found experimentally for the speed ratio.

3.4.5 Role of the k vector in the NP's motion

Let us now address the role of $\mathbf{k}_{\parallel}$ in the NPs' directional motion. We study the dependence on $\mathbf{k}_{\parallel}$ by changing successively the optical paths in the experimental set-up of **Figure 3.2**a. In this experiment, the laser beams are polarized in the plane of incidence (p-polarization). Both beams impinge on the sample surface at 45°. The in-plane component of the polarization $\mathbf{E}_{\parallel}$ remains identical and aligned along $\mathbf{k}_{\parallel}$ for the two beams whereas the sign of $\mathbf{k}_{\parallel}$ is reversed at the same surface position. The experiment consists in irradiating successively the sample with each laser beam. The sample used in this experiment is coated with very few Au NPs. The result of this experiment is reported in **Figure 3.15** containing a set of $2.3\mu m \times 2.3\mu m$ experimental shear-force images arranged in one column, separated in two groups, a and b, corresponding to the two irradiation configurations. The vertical time axis indicates the recording time of each image.

We focus on the behaviour of the NP followed by the white arrow in **Figure 3.15** (a). Since $\mathbf{E}_{\parallel}$ is colinear to $\mathbf{k}_{\parallel}$, one expects the NP to move in the direction of $\mathbf{k}_{\parallel}$. This is, indeed, what we observe in the experimental images. The NP exhibits very little change in its vertical position but shows a clear movement along the horizontal direction parallel to $\mathbf{k}_{\parallel}$: when $\mathbf{k}_{\parallel}$ is set to the right (in (a)), the NP moves to the right; conversely, when

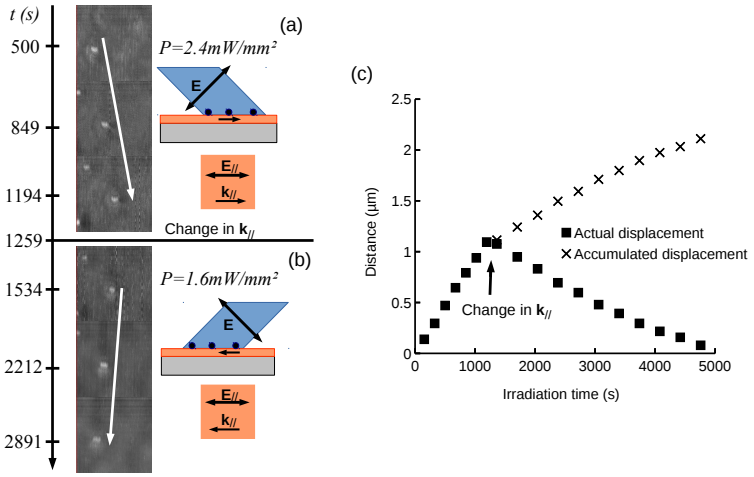

Figure 3.15: Effect of $\mathbf{k}_{\parallel}$ on the Au NPs' motion when inverting the direction of $\mathbf{k}_{\parallel}$. Blue p-polarized laser beam $\lambda = 488nm$ illuminating the sample (a) from the top with the light intensity of $2.4mW/mm^2$ and (b) from the bottom with the light intensity of $1.6mW/mm^2$. (c) Distance crossed by the Au NPs versus time.

$\mathbf{k}_{\parallel}$ is inverted, the NP moves to the left. The distance traveled by the NP is summarized in **Figure 3.15** (c), the time at which $\mathbf{k}_{\parallel}$ is inverted is indicated by an arrow. In this graph, we see that the time required for the NP to invert its movement is not larger than the time of an image frame ($85.33s$). If we consider the accumulated displacement of the NPs, we see that the return displacement is associated to a kink in the slope of the curve. It could be attributed to a light intensity effect since the second beam has a lower intensity ($1.6mW/mm^2$) compared to the first beam ($2.4mW/mm^2$). These results seem to underline the role of $\mathbf{k}$ in determining the direction NPs' motion. However, further study in 3.4.6 will discard this vision as it reveals a new complexity of the NPs' motion.

Application: Optical displacement of NPs at will!

We have so far established the dependence of the movement on $\mathbf{E}_{\parallel}$ and $\mathbf{k}_{\parallel}$. In the previous section, we have shown that an s-polarized illumination does not induce NPs' movement. However, one may combine several short movements to make a resultant movement in the direction parallel to the s polarization. One possible configuration is the alternating illumination by two laser beam polarized at $45°$ and $-45°$ (**Figure 3.16**).

The experiment is carried out on a sample having Au NPs. In the left image, the two alternating laser beam with their respective polarization are represented. The power density of the first and the second beam are respectively $1.6mW/mm^2$ and $2.4mW/mm^2$. In the image on the right, we

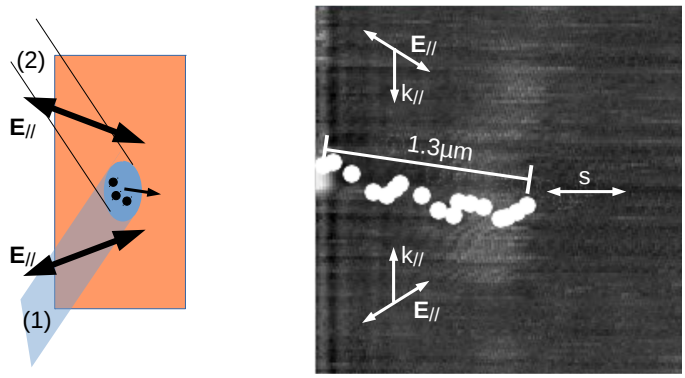

Figure 3.16: Combination of two directional motions resulting in a NP's motion along the *s*-component of **E**: Motion obtained by alternate illuminations of two laser beams polarized at 45° and −45°.

show the successive positions of one nanoparticles under this illumination. The trajectories of the NPs are composed of small straight movements which result from the individual illumination of each laser beams. The resultant zig-zag movement is close to the vertical direction which in this case is the direction of the s polarization. We demonstrate thus a complete optical control to displace NPs along customized directions.

3.4.6 Illumination through the substrate

We have interpreted in 3.4.3 the directional motion of the NPs as a phenomenon of fluidification of the azoploymer film upon photo-isomerization of the azobenzenes. The photo-isomerization induces an expansion stress in the material, the magnitude of which depends on the intensity and polarization of the light [14]. The direction of matter flow being given by the orientation of the light field vector, the flow can thus pull away the NPs. The flow extends to at least the diameter of the NPs beneath the film surface, since the immersed NPs are still subjected to the same motion. So the question to be answered is whether the fluidity of the layer and the resulting NPs' motion is affected when the excitation light is transmitted through the glass substrate. In this irradiation configuration, the fluidized layer is now in contact with the substrate. Moreover, this study should provide a new insight into the role of $\mathbf{k}_{\|}$.

For this purpose the sample is first irradiated from the front side (**Figure 3.17** (a) and then from the rearside (b). The sample is coated by polystyrene NPs. The laser polarization is in the incidence plane, i.e. p-polarized with an incident angle of 45°. We check that in each optical configuration the laser beam hits the surface under the same angle of incidence by superposing both

beams. Under this illumination conditions, the light polarization (not the intensity) remains the same, while the sign of the component $\mathbf{k}_{||}$ is opposite. As a consequence as previously shown by reversing the sense of the $\mathbf{k}$ vector of p-polarized light, we are entitled to expect the reversal of NPs' motion.

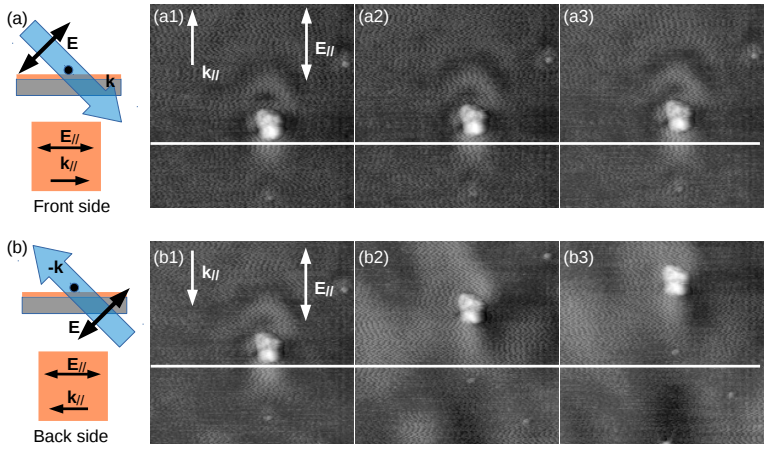

Figure 3.17: NPs' motion induced by the irradiation from the front and the rearside of the sample. p-polarized blue laser beam $\lambda = 488nm$ illuminates the sample (a) from the front side ($\mathbf{k}$) with the light intensity $1.6mW/mm^2$ and (b) from the rearside ($-\mathbf{k}$) with the light intensity $2.4mW/mm^2$.

The experiment starts with the front side illumination with an intensity of $1.6mW/mm^2$. After $3000s$ we switched off the front side laser beam and turned on the rearside laser beam with an intensity of $2.4mW/mm^2$. The switching time is short compared the time of imaging. The distance travelled by the NP's is shown in **Figure 3.18**. Surprisingly no return motion of the NP is measured, despite the inversion of the $\mathbf{k}$ vector. Moreover the NP's displacement speed is strongly boosted with an 11-fold increase when enlightening the azopolymer film from the rearside of the substrate. This result is even more puzzling if we estimate the respective light intensities absorbed by the azobenzene molecules. The absorptivity of the DR1 film is about 0.7-0.8 at $488nm$. Therefore the light intensity reaching the sample surface after being transmitted through the substrate is 15% of the incident intensity. Knowing the incident light intensities for both optical configurations, we find that DR1 molecules receive 4.5 times more light under the front side illumination. Thus paradoxically the NP's motion does not slowdown in spite of the lower incoming light intensity.

The above described experiment has consisted in two successive illuminations of p-polarized light. We can wonder whether the net increase in the NP's motion speed obtained in the rearside illumination still occurs without any pre-illumination history. In **Figure 3.19**, we compare the kinetics

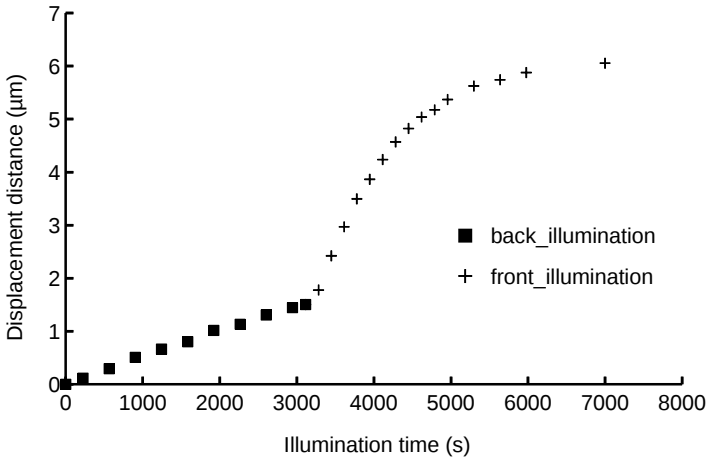

Figure 3.18: Comparison between the front side and the rearside illumination of the sample. p-polarized blue laser beam of wavelength $\lambda = 488nm$ impinges on the sample surface at $\theta = 45°$. The respective power densities of the front side and rearside illumination are $1.6mW/mm^2$ and $2.4mW/mm^2$, respectively.

of NPs displacement versus time between 45°-polarized illumination from the front side and p-polarized illumination from the rearside. We did not have enough time to perform the front side illumination using p-polarized light. NPs' displacement is strongly enhanced when the light goes first through the substrate (**Figure 3.19** (a)). As compared to NPs' displacement obtained by the front side illumination with p and 45°-polarized light, the NPs' displacement remains larger in the rearside illumination. From the **Figure 3.19** (a), we can extract the time variation of the NP's speed (**Figure 3.19** (b) and (c)).

Conclusion

This observation confirms once more that the NPs' motion is not due solely to the local induced field of the NPs since this field is the same in these two illumination geometry. Moreover, this phenomenon is not a surface process but rather a bulk process. Indeed, using the same laser power density, although the nanoparticles receive less optical power under the irradiation from the rearside because of the azopolymer film's absorption, the NPs travel faster. While the NPs' motion operates along $\mathbf{E}_{\parallel}$, its orientation is not ruled by $\mathbf{k}_{\parallel}$. The result of this section

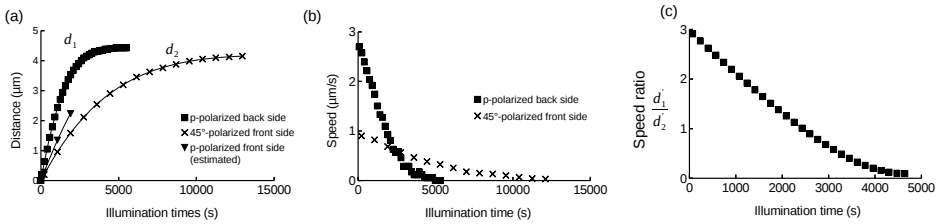

Figure 3.19: Comparison of kinetics of motion induced by irradiations from the front and the rearside of the sample. The laser beam of $2.4mW/mm^2$ irradiates the sample at 45°. (■): rearside illumination under p polarization. (×): front side illumination under 45° polarization. (▼) front side $2.4mW/mm^2$ illumination under p polarization from the data and the ratio found in **Figure 3.14**.

then implies that the direction of the flow depends only on the angle between the light polarization and the normal vector of the surface.

The difference in the movement speed between the frontside and the rearside illumination highlights the role of absorption. By these considerations, it is important to investigate the dependence of the movement of the NPs on the film thickness. This will be reported in the next paragraph.

3.4.7 Dependence of the motion on the film thickness

In all of the previous experiments, we have worked on PMMA-DR1 thin film having the same thickness of about $200nm$. Since the moving fluid stems from the absorption of the azobenzene molecules, its dynamics would depend on the film thickness. In this section, we report an experiment of the optical induced movement of the nanoparticles deposited on a $70nm$-thick PMMA-DR1 film.

Figure 3.20 presents a series of $2.6\mu m \times 2.6\mu m$ topographic images obtained from the experiment with the $70nm$-thick PMMA-DR1 film. The images, separated by $341.32s$, reveal the evolution of the film topography under 45°-polarized irradiation at 45° within the absorption band of the azobenzene molecules ($\lambda = 488nm$). Four objects are recognized in these images: three NPs (of either Au or polystyrene since both types were present on the surface) of similar size and one bigger object ($400nm$ in diameter). We observed that while the NPs exhibit the expected movement according to the previously established relation with the illumination, the big object remains immobile throughout the experiment. This object is probably a defect at the glass substrate with a height larger than the film's thickness.

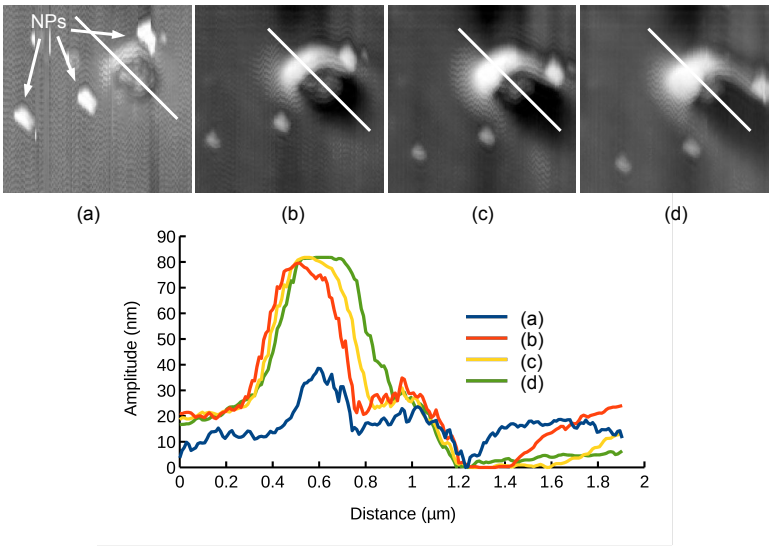

Figure 3.20: Evidence of the flow around a defect localized at the surface of a polystyrene NPs coated PMMA-DR1 film of $70nm$ thickness. Shear-force images and the corresponding topography profile along the white line. 45°-polarized blue laser beam $\lambda = 488nm$ impinges on the sample surface at 45°. During the experiment, the illumination is changed from the rear-side (of power density $2.4mW/mm^2$) to the frontside (of power density $1.6mW/mm^2$) without inducing visible change in the movement speed.

The flow of the film is demonstrated by observing the evolution of matter surrounding this this defect. During the irradiation, the film surface in the proximity of the defect changes gradually its shape. A large structure builds up at the top-left to gradually wrap the defect. The material is progressively depleted at the lower-right of the defect leaving a downstream wake.

The topographic profile along the white line crossing the defect is provided in the graph help to clarify the film behaviour around the defect. The surface defect appears in the middle of the profile curves (at $1\mu m$) having a stable height of about $30nm$. The surface profiles on both side of this defect changes as one goes from (a) to (d). The height of the structure to the left of the defect grow strongly by $40nm$ from $40nm$ to $80nm$, the change is abrupt between the first and the second image and then is more stabilized. To the right of the defect, the bump structure at the boundary between the defect and the film surface is gradually flatted. A frequent picture of this phenomenon is seen in the case of a liquid flow disturbed by a fixed object. The liquid on the upstream side of the object can move over this object while on the downstream side close to the object, the liquid level is lower than the medium. The presented profiles were also taken in the flow direction (given

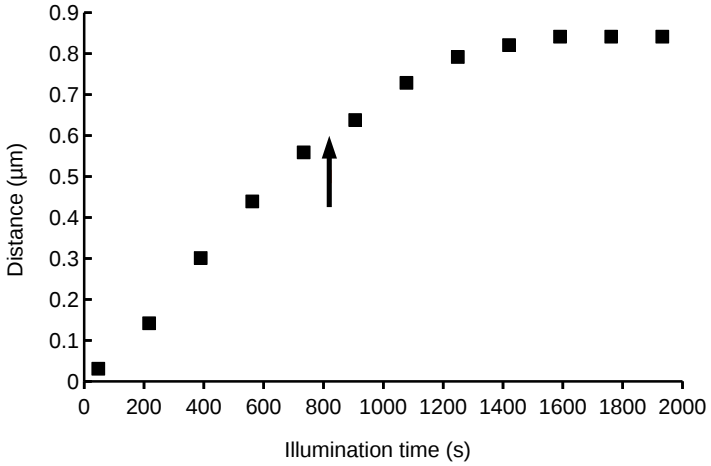

Figure 3.21: Time-evolution of the movement of the nanoparticles deposited on a PMMA-DR1 film of thickness $70nm$. The light is 45°-polarized and irradiated the sample at 45°. At the position indicated by the arrow, the illumination is switched from the rearside, $2.4mW/mm^2$ to the frontside $1.6mW/mm^2$

by the movement of the nanoparticles). Thus it gives a rather conclusive evidence of a photo-induced flow of the azofilm which is responsible for the movement of the NPs.

Figure 3.21 shows the time-evolution of the movement of the nanoparticles seen in the previous figure. The light is 45°-polarized and irradiated the sample at 45°. At the position indicated by the arrow, the illumination is switched from the rearside, $2.4mW/mm^2$ to the frontside $1.6mW/mm^2$. This change takes place before the saturation of the nanoparticles' movement. From the result of 3.4.6, it is expected a large decrease in the movement speed. This is clearly not what happens. Thus the relative efficiency between the rearside and the frontside irradiation on the movement of the NP, on the film flow, depends on the film thickness. It may be linked to the fact that the film thickness is inferior to its absorption length due to azobenzene molecules ($124nm$ for $\lambda = 488nm$). It will be fruitful to establish a more exhaustive comparison by studying the complete time-evolution of the NPs' movement for the two irradiation condition and also for other film thicknesses.

Conclusion

This experiment on thinner films brought the convincing proof that the light polarization induces a directional matter flow in the azofilm. Actually, the NPs, which are dragged away by the flow play the role of marker allowing thus to directly visualize the matter flow. Moreover the observed burying of NPs under illumination argues in favor of the change in the mechanical properties of the photosensitive film and the occurrence of a fluid, whose viscosity affects the flow dynamics.

To end up our investigation on NPs' motion on illuminated azofilms, we will present complementary experiments, which do corroborate our conclusions. The first experiment addresses the issue of changing the amplitude of the active electric field component $\mathbf{E_x}$ by varying the angle of incidence θ. The second set of experiments deals with the increase in the incident power density.

3.4.8 Complementary experiments

Dependence on the illumination intensity

In this section, the dependence of the particles' movement on the light intensity is studied. In **Figure 3.22**, the comparison is made between two irradiation density (■) $1.6mW/mm^2$ and (×) $16mW/mm^2$. The studied sample is a PMMA-DR1 of standard thickness (about $200nm$) with polystyrene nanoparticles deposited above. In both cases, the sample is illuminated at 45° under p polarization from the frontside. In this experiment, the data are obtained only for the initial state of the movement where it exhibits an approximately linear time dependence. The slope of the fitted line gives the speeds of the movement which are $0.5nm/s$ for the $1.6mW/mm2$ case and $6.8nm/s$ for the $16mW/mm^2$ case. The speed ratio between these cases is 13.6 which is slightly larger than the ratio of the power densities. Thus, within this range of power density, the initial movement rate or the flow within the film depends almost linearly on the irradiation intensity.

On the same sample, we obtain the complete time-evolution of the movement for a slightly different illumination condition. The light polarization is now turned to 45° and the compared power densities are (■) $p = 24mW/mm^2$ and (×) $p = 2.4mW/mm^2$. In **Figure 3.23**, under high irradiation intensity, $p = 24mW/mm^2$, the displacement depends linearly on time during the first $800s$ with the rate of displacement of about $8.25nm/s$. Then it slows down and beyond $1000s$, the movement rate is stabilized at about $0.17nm/s$ while the displacement distance reaches $4.5\mu m$. Under low illumination intensity, the displacement rate starts at

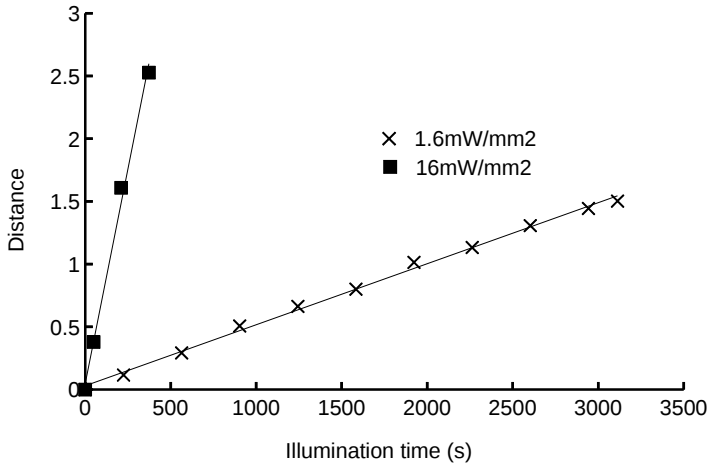

Figure 3.22: Displacement of the nanoparticles under p-polarized illumination. The sample is illuminated from the front surface at the angle of incidence $\theta = 45°$ by blue collimated laser beam of wavelength $\lambda = 488nm$. The light power density is (■) $1.6mW/mm^2$, (×) $16mW/mm^2$

about $0.97nm/s$ which is about 8.5 times smaller than in the case of large power density. Even though this ratio is smaller than in the previous study, it is still close to the ratio between power densities and a linear dependence of the NPs movement, or the film flow, on the irradiation intensity can still apply. This applies moreover to the time required to saturate the movement. The displacement saturates at the same value of about $4\mu m$ and the time required to attain this saturation is about 10 times larger for $p = 2.4mW/mm^2$ ($t_{s1} \approx 1000s$) than for $p = 24mW/mm^2$ ($t_{s2} \approx 12000s$).

Dependence on the angle of incidence

Figure 3.24 shows the time-evolution of movement of the nanoparticles under a p-polarized illumination at 71.6° from the frontside with the power density $24mW/mm2$. The movement distance depends linearly on time during the first $800s$ which is about the same time under the irradiation with the same power density at 45° reported in **Figure 3.23** (a). The time-evolution curve is practically flat beyond $2000s$ as the cumulated distance reaches $4.8\mu m$. This movement starts with a rate of $5.5nm/s$. We have shown in **Figure 3.14** (b) that the speed ratio between the movements induced by the p-polarized and 45° irradiation in the initial instant is comprised between 1.35 and 1.45. By multiplying by the factor, the speed of the movement is between $11.1nm/s$ and $12nm/s$. The speed ratio between

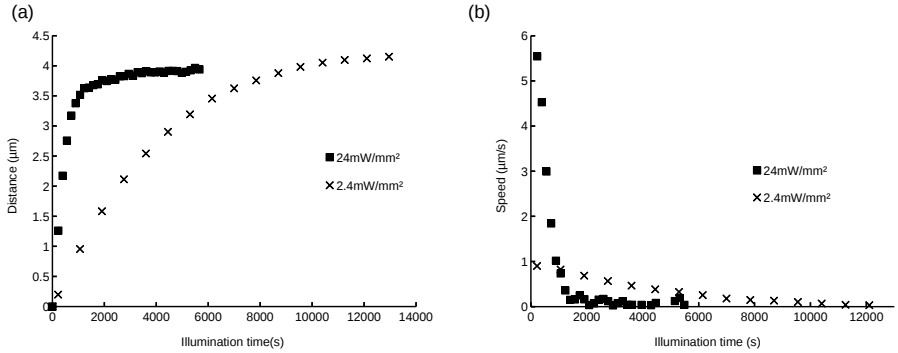

Figure 3.23: Displacement of the nanoparticles under 45°-polarized illumination. The sample is illuminated from the front surface at the angle of incidence $\theta = 45°$ by 45°-polarized blue collimated laser beam of wavelength $\lambda = 488nm$. The light power density is (■) $24mW/mm^2$, (×) $2.4mW/mm^2$

the movement under p-polarized irradiation at 45° and 71.6° is between 2 and 2.2. Given that under a p-polarized illumination, the ratio between the in-plane projection of the light polarization when the angle of incidence is 45° to when this angle is 71.6° is:

$$\frac{E_x^{45°}}{E_x^{71.6°}} = \frac{cos(45°)}{cos(71.6°)} \approx 2.24$$

It shows that the movement rate is proportional to the projection of the light polarization on the x-direction (see **Figure 3.2**).

3.5 Exploratory conclusion

Figure 3.25 summarizes the different illumination configurations, which contribute to put into motion NPs deposited on azobenzene-containing film. It turns out:

1. The NPs' motion is the direct consequence of the fluidification of the photosensitive film under polarized light. It is not related to an optical tweezer effect and to a mechanism of electric field exaltation.

2. The direction of the matter flow is along the in-plane electric field component. More precisely, the direction of the flow depends on the angle between the light polarization and the normal vector of the surface. The configuration (d) (front-side and rearside illuminations) helps to exclude the dependence of the flow on **k**.

Let us now develop each of these features.

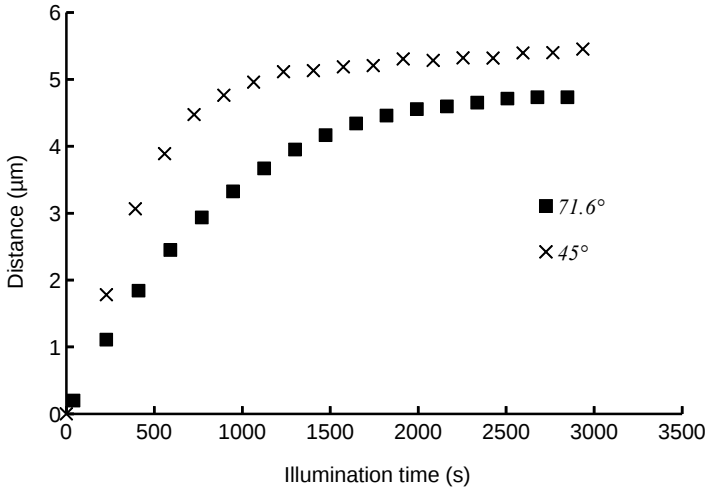

Figure 3.24: Dependence of the photo-induced NPs' motion on the angle of incidence of the irradiation. p-polarized blue laser beam $\lambda = 488nm$ impinges on the sample from the front surface. The light power density is $24mW/mm^2$. (■): motion induced by an irradiation at $\theta = 71.6°$. (×): estimated motion induced by an irradiation of the same power density and polarization at $\theta = 45°$. The estimation is made from the data in **Figure 3.23** and the normalization factor between p and 45° polarization is extracted from **Figure 3.14**.

1 - Previous experiments performed in the laboratory have investigated the mechanisms of formation of SRG in photochromic thin films containing azobenzene molecules. In these experiments, the photosensitive film is exposed to optical interference patterns with specific spatial distributions of the light polarization. The existence of such a polarization gradient results in a directional motion of matter. The kinetics of surface relief grating formation shows a saturation similar to that observed in the kinetics of NPs' motion. The saturation effect of the deformation is due to the photo-reorientation under polarized light and also to the photo-bleaching of the molecules. It also reflects the viscous elastic character of the photosensitive film under illumination. We also retrieve behaviours inherent to the azofilms under illumination, such as the increase in the kinetics of deformation when increasing the power density and the dependence of the kinetics on the film thickness. The novelty of our experimental approach is that by using a single polarized beam the matter flow can be detected by tracking the displacement of NP deposited on the film surface. Interference pattern gives a growth rate of the surface grating formation of a few tens of nm/s,

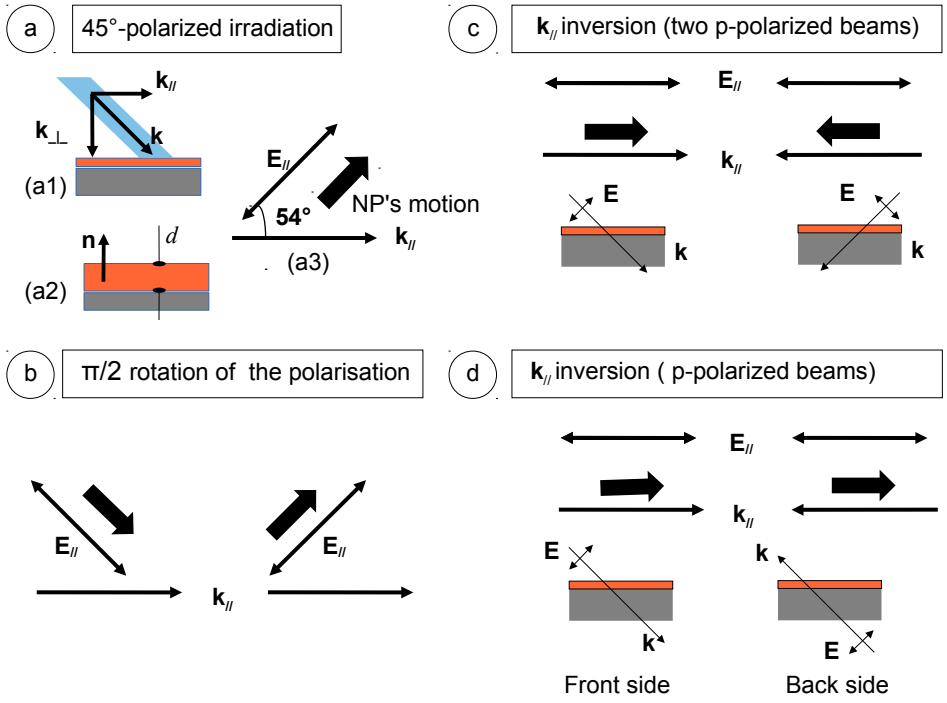

Figure 3.25: Summary of the experimental configurations to observe NPs' motion.

while the NPs deposited on the azofilm moves with a velocity in the range of a few $\mu m/s$. Actually the formation of surface relief grating requires two opposite matter flows due to the gradient of polarization, contrary to our experiment where NP move steadily in an uniform electric field.

Considering the NPs displacement, the role of inertia is negligible. Indeed, when the light is turned off, the NPs stop immediately which means the flow of the azofilm drops to zero. The ratio of inertial to viscous forces is usually described by the dimensionless Reynolds number. Small Reynolds numbers correspond to slow viscous flows because viscous forces, arising from shearing motions of the fluid, predominate over inertial forces. Our azofilm flow is associated to a low Reynolds number. In this condition we can estimate the drag force acting on a moving spherical NP in the fluid, derived from the creeping motion equations $F = -6\pi\eta Rv$, where v and η represent, respectively the velocity of the sphere of radius R and the viscosity. Since it is difficult to know exactly the value of η under illumination (η being typically equal to $10^5 m^2/s$ for basic PMMA), the range of the force is between $1nN$ and $10nN$ for a viscosity under illumination between $10^3 m^2/s - 10^4 m^2/s$.

2 - As shown by Navier-Stokes equation, in order to have a viscous flow in films, a driving force is required. In our experiment, the origin of this force could be due to the light gradient resulting from absorption of the azobenzene molecules, to the stretching of the molecular chains under illumination and/or to the stress due to field discontinuity at the borders of the film with the glass plate and free space.

We evidence a flow of the azofilm under homogeneous radiation by a laser beam. This proves that the light projected on the surface of the azofilm does not require an inherent optical variation to induce the mass transport.[6] Note that in all the theoretical models summarized in 1.2.3, a gradient of the optical pattern is needed to explain the mass transport.

We can reconcile this observation with the existing theoretical models by two possible ways:

- The light gradient is produced by the absorption of the azofilm related to the photo-isomerization. The light intensity decreases across the film along the direction of propagation. This effect is so far neglected in all the theoretical models of the photo-induced mass transport. However, in the experiment described in **Figure 3.25** (d), the change of illumination from the front to the rearside of the sample

[6]The light beams have gaussian distribution which present an axial gradient over the illuminated area. However, the flow is not driven by this gradient. Indeed, the intensity gradient varies linearly as one recedes from the center of the beam while the movement of the NPs does not depends on the spatial displacement.

turn up side down the light intensity across the film without changing the direction of the driving force. This makes this mode not viable to explain the flow of the film. The film absorption may however explains the fact that difference in the movement rate of the flow is induced more efficiently by an illumination from the rearside than from the frontside. Indeed, when the film is illuminated from the substrate side, the fluidization takes place mainly close to the substrate. This may relieve better the stress imposed by the substrate to the film that resists against the flows.

- The flow is induced by the field discontinuity at the boundary of the azofilm, that is its interfaces with the substrate and the free space. This field discontinuity is only present when the incidence is oblique and the polarization is appropriately oriented, that is not the case for s polarization. The field discontinuity at the film borders gives rise to faster flow in the film in the horizontal direction if both the in-plane component ($\mathbf{E_x} + \mathbf{E_y}$) and the out-of-plane component ($\mathbf{E_z}$) are large. Therefore, for a given field amplitude E_0, the flow is the most efficiently generated when the light polarization is inclined 45° with respect to the film surface. This corresponds to the case of p-polarized illumination at the incidence 45°. At the same incidence but under 45° oriented polarization, the incident electric field make an angle 60° with respect to the normal of the film. At the incidence 71.6° under p polarization, the incident electric field make an angle 18.4° with respect to the normal of the film. In both these configurations, we observe smaller movement velocity. Moreover, the movement velocity is, to a good approximation, proportional to the smaller field between ($\mathbf{E_{in-plane}} = \mathbf{E_x} + \mathbf{E_y}$) and $\mathbf{E_z}$. In the case of the photo-generation of SRG in azofilm, similar relation between the efficiency of the SRG generation and the polarization of the incident light has been reported in [11].

  The mathematical description of light-induced viscous flow including boundary conditions (free surface, and solid interfaces) is beyond the scope of this thesis. Nevertheless we propose to describe the velocity by the following phenomenological formula:

$$\mathbf{v} \propto E_0 min(E_z, \sqrt{E_x^2 + E_y^2})\hat{\mathbf{e}}_{xy} \tag{3.1}$$

  where E_0 is the amplitude of the electric field, E_i is the i-component ($i = x, y, z$, see **Figure 3.2** (b)), $\hat{\mathbf{e}}_{xy}$ is a unity vector parallel to the in-plane component of the incident electric field. The factor of proportion depends on the film thickness (see **Figure 3.25** (a2)).

Finally, let us compare our observation with the directional photofluidification described in [14]. In this report, two orthogonal canal carved on the surface of an azofilm. The photo-isomerization is next excited by irradiating the film under normal incidence. One observes the dilatation of the film in the direction of polarization. This dilatation fills up the canal perpendicular to the light polarization and leave the other canal (parallel to the polarization) intact. Thus, the stress that induces this dilatation seems to also stem from the field discontinuity at the boundaries of the structures.

The results in the study on the dependence on the power density and on the angle of incidence, is rather exploratory. More data points are thus required to confirm thisz suggested model.

Bibliography

[1] P. Rochon, E. Batalla, and A. Natansohn. Optically induced surface gratings on azoaromatic polymer-films. *Appl. Phys. Lett.*, 66(2):136–138, 1995.

[2] DY Kim, SK Tripathy, Lian Li, and J Kumar. Laser-induced holographic surface relief gratings on nonlinear optical polymer films. *Applied Physics Letters*, 66(10):1166–1168, 1995.

[3] LM Siewierski, WJ Brittain, S Petrash, and MD Foster. Photoresponsive monolayers containing in-chain azobenzene. *Langmuir*, 12(24):5838–5844, 1996.

[4] D Gustina, E Markava, I Muzikante, B Stiller, and L Brehmer. Photoisomerisation process of self-assembled monolayers of some novel azobenzene. *Advanced Materials for Optics and Electronics*, 9(6):245–251, 1999.

[5] Yanlei Yu, Makoto Nakano, and Tomiki Ikeda. Photomechanics: directed bending of a polymer film by light. *Nature*, 425(6954):145–145, 2003.

[6] Kunihiro Ichimura, Sang-Keun Oh, and Masaru Nakagawa. Light-driven motion of liquids on a photoresponsive surface. *Science*, 288(5471):1624–1626, 2000.

[7] A. Ashkin, J. M. Dziedzic, J. E. Bjorkholm, and Steven Chu. Observation of a single-beam gradient force optical trap for dielectric particles. *Opt. Lett.*, 11(5):288–290, May 1986.

[8] Liselotte Jauffred, Andrew C. Richardson, and Lene B. Oddershede. Three-dimensional optical control of individual quantum dots. *Nano Letters*, 8(10):3376–3380, 2008.

[9] Taiji Ikawa, Takuya Mitsuoka, Makoto Hasegawa, Masaaki Tsuchimori, Osamu Watanabe, and Yoshimasa Kawata. Azobenzene polymer surface deformation due to the gradient force of the optical near field of

monodispersed polystyrene spheres. *Physical Review B*, 64(19):195408, October 2001.

[10] N. Landraud, J. Peretti, F. Chaput, G. Lampel, J. P. Boilot, K. Lahlil, and V. I. Safarov. Near-field optical patterning on azo-hybrid sol-gel films. *Appl. Phys. Lett.*, 79(27):4562–4564, 2001.

[11] F. Fabbri, D. Garrot, K. Lahlil, J. P. Boilot, Y. Lassailly, and J. Peretti. Evidence of two distinct mechanisms driving photoinduced matter motion in thin films containing azobenzene derivatives. *The Journal of Physical Chemistry B*, 115(6):1363–1367, 2011.

[12] Filippo Fabbri. *Déformation photoinduite dans les films minces contenant des derivés d'azobenzene: effets de polarisation, effets de proximité et effets de contact*. PhD thesis, Ecole Polytechnique, 2009.

[13] Christophe Hubert, Anna Rumyantseva, Gilles Lerondel, Johan Grand, Sergeï Kostcheev, Laurent Billot, Alexandre Vial, Renaud Bachelot, Pascal Royer, Shih-hui Chang, Stephen K Gray, Gary P Wiederrecht, and George C Schatz. Near-Field Photochemical Imaging of Noble Metal Nanostructures. *Nano Letters*, 5(4):615–619, 2005.

[14] Peter Karageorgiev, Dieter Neher, Burkhard Schulz, Burkhard Stiller, Ullrich Pietsch, Michael Giersig, and Ludwig Brehmer. From anisotropic photo-fluidity towards nanomanipulation in the optical near-field. *Nature materials*, 4(9):699–703, September 2005.

Part II

Hybrid metal/dielectric nanostructures with adjustable optical and plasmonic properties

Chapter 4

Basics on surface plasmon

This section provides the theoretical background of surface plasmon (SP) and serves as basis for the study of plasmonic structure in Chapter 6. Resonant surface plasmon, also called surface plasmon or surface-plasmon-polariton (SPP), is an electromagnetic wave propagating at a metal/dielectric interface [1] and is associated with the oscillation of the density of electric change at the metal surface. The electromagnetic field of SP is maximal at the interface and decays exponentially along the interface's normal giving rise to field confinement in this direction. The large field confinement allows squeezing electromagnetic wave into subwavelength volume therefore reducing the size of the optical devices. Moreover, the resonant nature of SP makes it extremely sensitive to the minuscule change of its medium. SP is thus a prominent candidate for sensing application [2].

The first reported manifestation of SP is Wood's anomalies, named after R. W. Wood who observed, in 1902, the extraordinary variation of the diffraction spectrum of a metallic gratings for certain polarization of the illumination [3]. Lord Rayleigh provided, in 1907, the first interpretation of Wood's anomalies based on diffraction optics as he attributed them to the "passing-off of a spectrum on higher order" [4]. However, latter experimental data revealed the dependence of Wood's anomalies on the metal and contradicted this diffraction picture [5]. Only until 1941 that Fano provided the first satisfactory explanation for Wood's anomalies by predicting the existence of a leaky surface wave which is only excited by the incident light under specific condition [6]. This wave is later dubbed SP. In 1968, using energy-loss electronic spectroscopy experiment, Ritchie revealed the electronic nature of SP and by this completed the picture on the nature of SP [7]. Renewed interest in SP has been triggered recently, on the one hand, by the discovery of the extraordinary optical transmission through subwavelength holes array [8] and on the other, by the progress in the techniques of nanostructure fabrication and characterization.

4.1 Collective electronic oscillations in metals

SP can be understood within the framework of the electromagnetic theory based on the Maxwell's equations. The optical properties of metals are described by their dielectric function ϵ_m which is a complex function of the incident wavelength. The Drude's model of free electrons provides a simple analytic expression for the ϵ_m of noble metals [1]:

$$\epsilon(\omega) = 1 - \frac{\omega_p^2}{\omega^2 + i\gamma\omega} \tag{4.1}$$

where $\omega_p = \frac{ne^2}{\epsilon_0 m}$ is the plasma frequency (i.e. the resonant frequency of the free electrons' collective oscillation in the metal), n is the free electron density, γ is the characteristic collision frequency of the free electrons and m is their effective mass. In the case of noble metals (e.g. Au, Ag, Cu), the filled d band close to the Fermi surface causes a highly polarized environment giving rise to ϵ_∞ instead of 1 as the first term in equation 4.1. Inter-band transitions can be described by Lorentz-oscillators. Thus, in order to include the effect of the inter-band transition in the dielectric function, one can add terms of the form $\frac{A_i}{\omega_i^2 - \omega^2 - i\gamma_i\omega}$ to the equation 4.1 [9]. The value of ω_p for several metals are given in table 4.1. In general, noble metals, such as Au, Ag, Cu, which have low Ohmic loss are good candidates for SP applications.

Metal	Plasma wavelength (nm)	$\omega_p(THz)$
Ni	77.89	3852
Al	82.78	3624
Cu	114.50	2620
Cr	115.35	2601
Au	137.32	2185
Ag	137.62	2180

Table 4.1: Plasma frequency for common metals

4.2 Surface plasmons at metal/dielectric interface

The existence of SP as a surface electromagnetic mode can be shown by solving the Maxwell's equations with the boundary conditions corresponding to a metal/dielectric interface supporting a transverse magnetic (TM) electromagnetic wave (p polarization). In the case of a semi-infinite metal medium, the dependence between the in-plane wavevector $k_{||}$ and the wavelength of

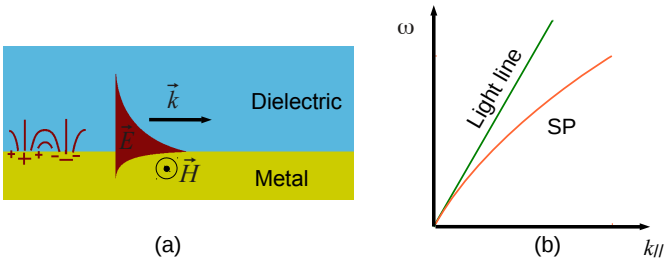

Figure 4.1: Surface plasmons at a metal/dielectric interface (SP). (a) Electric field variation across the interface. (b) SPs dispersion curve lying to the right with respect to the light line of the same dielectric.

the incident light reads as [1]:

$$k_{\parallel} = k_0 \sqrt{\frac{\epsilon_d \epsilon_m}{\epsilon_d + \epsilon_m}} \tag{4.2}$$

where ϵ_m and ϵ_d are the dielectric function of the metal and the dielectric, respectively, k_0 is the wavevector of the incident light coming from the dielectric side. ϵ_m depends on the incident wavelength. Optically, metal is distinguished from dielectric by the fact that ϵ_m can assume negative values when the incident frequencies is smaller than ω_p (see equation 4.1). This stems from the interaction between the electromagnetic wave and the free electron cloud and is the reason for the characteristic strong reflectivity of metal. If ϵ_m is smaller than $-\epsilon_d$ then $k_{\parallel}$, according to 4.2, becomes larger than k_0 and obliges the perpendicular wavevector component to take imaginary value. Such solution of the Maxwell's equations, a SP, propagates along the metal surface and decays exponentially in the direction normal to this surface. A SP is represented in **Figure 4.1**. The wavevector, equivalent to the momentum, of SP is always larger than the one of the photon in the same dielectric. In order to couple SPs with light, it is essential to compensate this momentum difference. This, together with the specific polarization of SP, imposes two conditions for the light-SP coupling [1]:

C1 on the light polarization. Since SPs are collective oscillations of the density of surface charge, the electromagnetic boundary conditions impose that the incident electric field must have a component perpendicular to the interface. In most cases, this implies the incident light to be polarized in the plane of incidence (TM or p polarization).

C2 The difference in momentum must be compensated. In optics, this can be achieved by employing prism or surface scattering. Two variations in the use of prism, known as Kretschmann's [10] and Otto's [11], are

shown in **Figure 4.2**. Scattering by surface defects can also compensate the wavevector difference. Grating-coupler is a special case of the surface scattering approach which allows the phase-match condition to be fulfilled by grating diffraction. In fact, the Wood's anomalies is explained by the SP excitation due to surface gratings. One should note that in both coupling methods, the reverse process that converts SPs into propagating light is also possible. The phase-match condition can be summarized in equation 4.3.

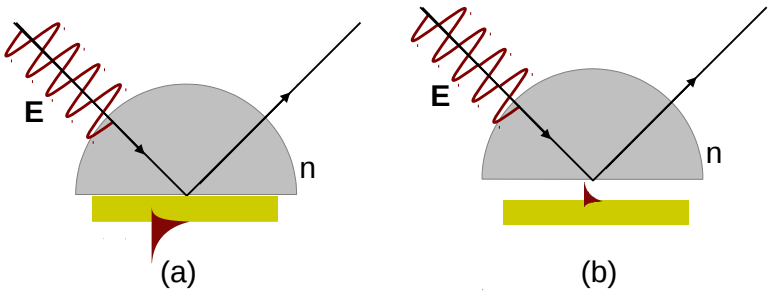

Figure 4.2: (a) Kretschmann's configuration. (b) Otto's configuration

$$k_{sp} = n\frac{\omega}{c}sin(\theta) \pm Nk_a \tag{4.3}$$

where a is the grating constant, $k_a = \dfrac{2\pi}{a}$ is the grating vector and n is the optical index of the incident medium.

SPs, as they propagate on metal/dielectric interface, lose energy through Ohmic damping (by generating heat) and radiation damping. The Ohmic damping, also called internal loss, depends on the conductivity of the metal. The radiation damping is due to the conversion of SPs to propagating wave therefore depends on the efficiency of this process.

4.3 Plasmonic bandgap

Like electrons in solid crystals, scattering of photons by periodic structures may prohibit their propagation over a range of energy (or angular frequency ω) giving rise to the so-called "photonic band gap" (PBG). The depletion of optical modes inside the band gap and the accumulation of the modes at the band edges point to the possibility of engineering the local density of optical states (LDOS) by playing with the energy and the width of the gap. Therefore, PBG and the intimate relation between the LDOS and the spontaneous emission are the central concepts in nano-optics. The same

paradigm applies for SPs and periodically corrugated surfaces giving rise to the so-called "plasmonic band gap". The first observation of full plasmonic band gap in the visible range, between $1.9eV$ and $2.00eV$, was reported by Kitson *et al.* in 1996 [12], illustrated in **Figure 4.3**.

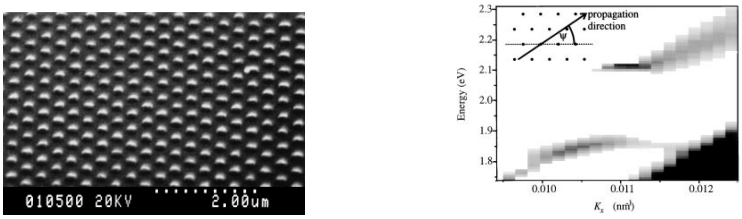

(a) (b)

Figure 4.3: Plasmonic bandgap. (a) Scanning electron micrograph of hexagonal array of dots of lattice constant $300nm$ on Ag surface. (b) Reflectivity data showing dispersion curves of SPs and a plasmonic band gap between $1.9eV$ and $2.00eV$. Image courtesy of [12].

4.4 Extraordinary optical transmission

The discovery of the Extraordinary optical transmission (EOT) through subwavelength hole arrays has recently triggered tremendous research interest [8]. The authors rapidly pointed out the connection between the EOT with SPs. In simple terms, the incident light couples with the SPs of the front face thanks to the periodic hole array. The SPs helps funneling the light energy impinging on the surface outside of the holes towards the latter, couples with the SPs on the opposite surface via the hole mode. The SPs on the opposite surface can next be reconverted into propagating light also by grating scattering. This early interpretation of the EOT is however challenged because the EOT is also observed in the microwave range where SPs are poorly excited [13]. This debate has only recently been resolved by the identification of two types of surface waves participating in the EOT, one is SP, and the other is a quasi-cylindrical surface wave mode [14]. Respective contribution of these modes contribute to the EOT depends on the incident photon energy. In the visible range, they contribute equally to the EOT [14].

4.5 Coupled SPs on metal thin film

A metal film can support SPs at both of its interfaces. If a metal film is surrounded by the same dielectric material and is sufficiently thin, the SPs

of the two interfaces have the same wavevector SPs. They can couple and give rise to symmetric and anti-symmetric modes [15]. If the surrounding dielectrics have different refractive indices, the wavevectors of the SPs are different. They are thus in general not coupled. However, if the surface is periodically corrugated, grating diffraction can again compensate the wavevector difference as long as [16, 17]:

$$k_{SP1} \pm k_a = \pm k_{SP2}$$

where k_{SPi}, $i = 1, 2$ are the wavevectors of the two SPs and k_a is the grating vector. Then these SPs can interfere. This phenomenon, referred to as cross-coupling, offer a possible mechanism to enhance the light transmission through continuously metallic thin film without recourse to hole arrays. Barnes, and the coworkers, described two regimes of cross-coupling, namely weak and strong [17]. In the weak coupling, the SPs exchange energy across the metal film but their dispersion curves are not affected, no anti-crossing occurs at their intersection [16–18]. In the strong coupling, lifting of degeneracy, i.e. anti-crossing of the dispersion curves, occurs [19, 20]. One should keep in mind that some case, the dominant effect of loss may hinder the observation of the anti-crossing [21].

4.6 Conclusion

SP offer the enhancement and the confinement of electric field into subwavelength volume. SP is support by metal/dielectric interface therefore is influenced by its structure. Metal grating is an important building brick of plasmonic devices because it supports the SPs, help fulfilling the phase-match condition and thus plays fundamental role in light-SP coupling, plasmonic band gap generation and SPs cross-coupling. Existing methods of metal grating fabrication are mainly based on lithography. As powerful as it is, this technique usually requires multi-step processes and costly installation. In this context, photo-generation of SRGs in azofilm constitutes and interesting alternative. Moreover, it can be easily combined with metal deposition to offer a simple and fast solution to obtain metal gratings. More interestingly, this fabrication process is reversible and nondestructive. One can continuously adjust the optical or the plasmonic properties of the metal structures by illumination. This study will be the subject of chapter 6.

Bibliography

[1] Heinz Raether. *Surface plasmons on smooth surfaces*. Springer, 1988.

[2] William L WL Barnes, Alain Dereux, and Thomas W TW Ebbesen. Surface plasmon subwavelength optics. *Nature*, 424(August):824–830, 2003.

[3] RW Wood. On a remarkable case of uneven distribution of light in a diffraction grating spectrum. *Proceedings of the Physical Society of London*, 269, 1902.

[4] Lord Rayleigh. Iii. note on the remarkable case of diffraction spectra described by prof. wood. *The London, Edinburgh, and Dublin Philosophical Magazine and Journal of Science*, 14(79):60–65, 1907.

[5] John Strong. Effect of evaporated films on energy distribution in grating spectra. *Phys. Rev.*, 49:291–296, Feb 1936.

[6] U Fano. The theory of anomalous diffraction gratings and of quasi-stationary waves on metallic surfaces (Sommerfeld's waves). *JOSA*, 928(1935), 1941.

[7] R. H. Ritchie, E. T. Arakawa, J. J. Cowan, and R. N. Hamm. Surface-plasmon resonance effect in grating diffraction. *Phys. Rev. Lett.*, 21:1530–1533, Nov 1968.

[8] TW Ebbesen, HJ Lezec, HF Ghaemi, and T Thio. Extraordinary optical transmission through sub-wavelength hole arrays. *Nature*, 1998.

[9] Stefan Alexander Maier. *Plasmonics: Fundamentals and Applications*. Springer, 2007.

[10] E. Kretschmann and H. Raether. Radiative decay of nonradiative surface plasmons excited by light. *Z. Naturforsch. A*, 23:2135, 1968.

[11] Andreas Otto. Excitation of nonradiative surface plasma waves in silver by the method of frustrated total reflection. *Zeitschrift für Physik*, 216(4):398–410, 1968.

[12] SC Kitson, William L Barnes, and JR Sambles. Full photonic band gap for surface modes in the visible. *Physical review letters*, 77:2670–2673, 1996.

[13] Stefan Enoch and Nicolas Bonod. *Plasmonics: from basics to advanced topics*. Springer, 2012.

[14] Frerik van Beijnum, Chris Rétif, Chris B Smiet, Haitao Liu, Philippe Lalanne, and Martin P van Exter. Quasi-cylindrical wave contribution in experiments on extraordinary optical transmission. *Nature*, 492(7429):411–414, 2012.

[15] Dror Sarid. Long-range surface-plasma waves on very thin metal films. *Phys. Rev. Lett.*, 47:1927–1930, Dec 1981.

[16] Rw Gruhlke, Wr Holland, and Dg Hall. Surface plasmon cross coupling in molecular fluorescence near a corrugated thin metal film. *Physical review letters*, 56(26):2838–2841, June 1986.

[17] S. Wedge, I. Hooper, I. Sage, and W. Barnes. Light emission through a corrugated metal film:?the role of cross-coupled surfaceplasmon polaritons. *Physical Review B*, 69(24):245418, June 2004.

[18] S. Ushioda, J. E. Rutledge, and R. M. Pierce. Prism-coupled light emission from tunnel junctions. *Phys. Rev. Lett.*, 54:224–226, Jan 1985.

[19] I Pockrand. Coupling of surface plasma oscillations in thin periodically corrugated silver films. *Optics Communications*, 13(3):311–313, 1975.

[20] Sachin Kasture, Prasanta Mandal, SD Gupta, and AV Gopal. Strong coupling of in-plane propagating plasmon modes and its control. *Optics express*, 21(11):13187–13192, 2013.

[21] M. G. Weber and D. L. Mills. Determination of surface-polariton minigaps on grating structures: A comparison between constant-frequency and constant-angle scans. *Phys. Rev. B*, 34:2893–2894, Aug 1986.

Chapter 5

Sample preparation and experimental setup

5.1 Photo-inscription of surface pattern

The set-up in **Figure 5.1** is used to optically inscribe surface patterns on PMMA-DR1 thin films. A linearly polarized laser of wavelength $\lambda = 488nm$ close to the absorption peak of the azobenzene derivative is used. In order to produce an interference pattern on the sample surface, the laser light beam is split into two beams of equal intensity which follow two optical paths of equal length, arrive at the sample from the substrate side and recombine at the sample surface. The light polarization is controlled by a half-wave plate mounted in front of the beam-splitter. The sample substrate is either in contact with air or is optically coupled to a glass prism (of optical index $n \approx 1.51$). The sample plane is perpendicular to the incident plane and the interfering beams are symmetric with respect to the normal axis drawn at the interference spot. This is achieved by making sure that the spots generated by the two beams on each optical component coincide. The output laser power is below $10mW$ to avoid destructive heat effect. The period of the interference pattern on the sample surface is given by:

$$\Lambda = \frac{\lambda_{laser}}{2nsin(\theta)} \tag{5.1}$$

where λ is the laser wavelength, $n \approx 1.51$ is the optical index of the glass prism, θ is the incident angle at the sample surface.

The inscription of surface relief pattern is monitored *in situ* by the SNOM which allows correlating the optical pattern with the optically generated surface structure. In particular, the structure shown in **Figure 5.1b** was fabricated by two successive projections of interference fringes which are perpendicular to one another. The *in situ* monitoring of surface topography

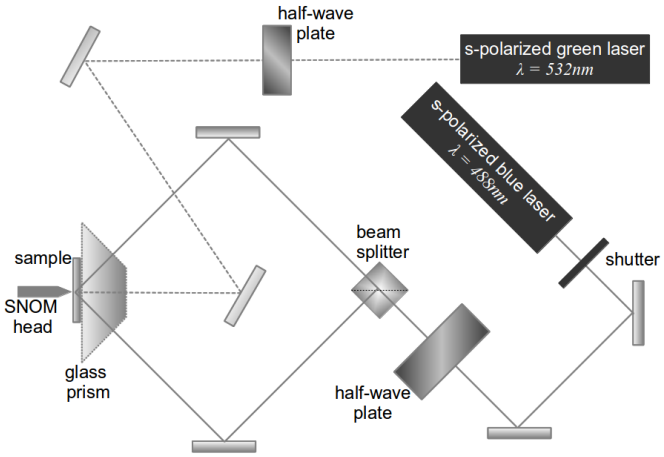

(a)

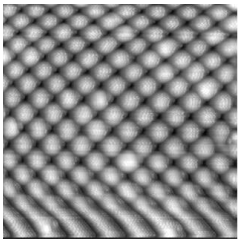

(b)

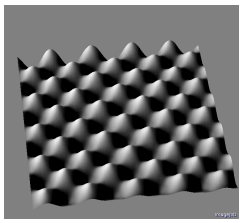

(c)

Figure 5.1: Surface patterning process. (a) Experimental set-up. (b) Fabrication of 2D pattern. (c) 3D representation of (b).

allows adjusting the dose of each projection in order to obtain the symmetric surface modulation.

5.2 Metal deposition

As we are interested in the optical and plasmonic properties metal gratings elaborated on photo-structured azomaterial films, metal deposition is a crucial fabrication step. In this study, we use Au because its low Ohmic loss and its chemical stability make it a good material in plasmonics. A schema of the Au deposition process is given in **Figure 5.2a**. The deposition is carried out by thermal evaporation under secondary vacuum ($p \approx 10^{-5} torr$). Au is loaded into a tungsten crucible which is heated, via Ohmic effect, by a D.C. current current $I \approx 35A$. The Au is heated to its boiling temperature to generate a Au vapor flux towards the sample. The deposition rate is controlled by means of a quartz crystal microbalance which measures the frequency shift of a quartz crystal resonator caused by the deposition of Au.

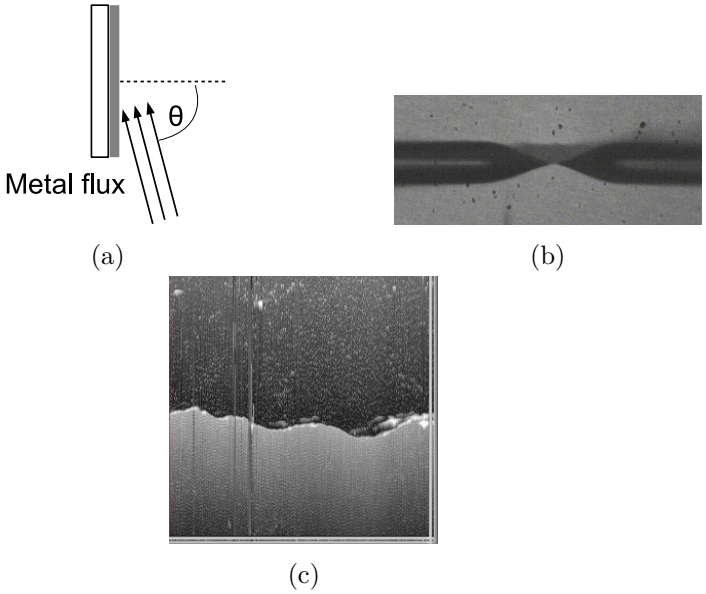

Figure 5.2: Deposition of metal. (a) The position of the sample surface with respect to the metal flux, defined by the angle θ. (b) The shear-force tip is place at the edge of a scratch on the metal surface. (c) Shear-force image showing the edge of the metal layer.

The quartz crystal microbalance gives a nominal thickness of the deposited Au amount. We calibrated the Au thickness by three complementary techniques: shear-force microscopy, surface profiler and Xray reflectometry (XRR). For a homogeneous film, XRR gives the most reliable measurement but the thickness is averaged over the area given by the size of the X-ray spot (about $1mm^2$). Surface profiler, consisting of scanning a tip across a scratch in the Au surface, gives rapid but less precise measurement of the thickness. Moreover, the commercial system of our disposition does not offer fine control of the tip force which is however required in dealing with Au film for its softness. Finally, shear-force microscopy (depicted if **Figure 5.2b and 5.2c**) which has close function principle to the surface profiler offers a middle solution between simplicity and the precision of the measurement.

The growth of Au film by thermal deposition is a complex process which is determined by the evaporation rate, the mobility of the metal atoms at the surface, the sample temperature, its heat dissipation and the incident angle of the Au flux. Depending on the Au evaporation rate, the surface morphology may show important topographic asymmetry. In **Figure 5.3**, the Au films are obtained by two different evaporation speeds and two different substrate, glass and glass-like sol-gel silica containing azobenzene. A

higher evaporation rate results in elongated Au grains. As will be discussed later, such asymmetry in the morphology of the Au film is also reflected in its optical and plasmonic properties.

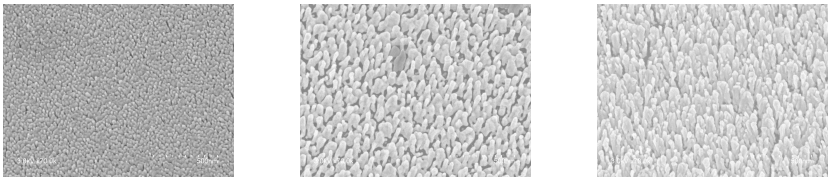

(a) (b) (c)

Figure 5.3: Morphology of Au films deposited at oblique incidence with different deposition rates and on different substrates. (a) Glass substrate, nominal rate $0.14nm/s$. (b) Glass substrate, nominal rate $1nm/s$. (c) Sol-gel-DR1 substrate, nominal rate $1nm/s$. All the depositions are carried out during $400s$.

If the surface is patterned prior to the Au deposition, more complicated structures can be obtained whose size and shape are determined by the template surface structure and the incident angle of the Au flux. The study of the optical properties of some of these structures will reported in chapter 6.

5.3 Patterning of metal/dielectric hybrid system

Metal structures deposited on azofilms can be optically structured by the bias of the azofilm. This constitutes a great advantage compared to the conventional lithography which require multiple *ex situ* steps and is generally non-reversible. In particular, one may modify gradually one structural parameter and observe in parallel how this change affects the optical properties of the sample. However, it is important to take into account the change of the azofilm's refractive index of the azofilm during the photoinscription due to photo-degradation and the angular hole-burning described in 1.1.3.

Figure 5.4 compares the efficiency of the surface patterning on a bare azo-polymer film and a similar film covered with $20nm$ of Au. We use the so-called p-assisted $s-s$ interference scheme [1, 2] to photo-inscribe the surface relief structure. Here, s-polarized interference is chosen in order to avoid the complicated angle-dependent distribution of the optical field inside the azofilm (which happens for p-polarized interference).

The Au over-layer does not inhibit the photo-induced mass transport but it reduces strongly the height of the photo-inscribed surface structures compared to the uncoated film. This indicates that the photo-induced mass

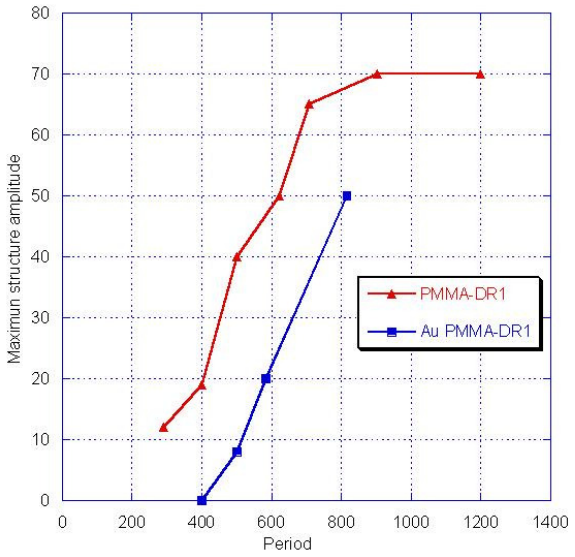

Figure 5.4: Surface relief amplitude as a function of the pattern's pitch: PMMA-DR1 film vs Au/PMMA-DR1 system. The patterning is performed by a $s-s$ interference pattern of $\lambda_1 = 488nm$ assisted by a p-polarized laser beam of $\lambda_2 = 532nm$ impinging the sample surface at normal incidence.

transport also occurs in the bulk of the azofilm. The reduction of the maximum photo-inscribed structure height can be explained by the mechanical constrain from the metal coating and its influence on the optical field distribution inside the photochromic film. It is interesting to note that the dependence of the maximum structure height on the interference period exhibits almost the same slope in the two cases. Below $400nm$, no structure was optically inscribed in the Au-covered azofilm.

In addition to patterning Au-coated azofilm, it is possible to optically modify existing Au structure supported by azofilm as illustrated in **Figure 5.5**. Here, starting from a sample having a period pattern of Au lines, we projected an interference pattern such that the fringes are perpendicular Au lines. We observed that along the Au lines developed an over-modulation having the same period as the interference.

5.4 Measurement of the optical index

The photo-patterning, by causing the angular hole burning (see 1.1.3) and photo-degradation of the azobenzene molecules, modifies the refractive index $n + ik$ of the azofilms. Precise information on the refractive index is crucial to understanding the optical and plasmonic properties, especially as the

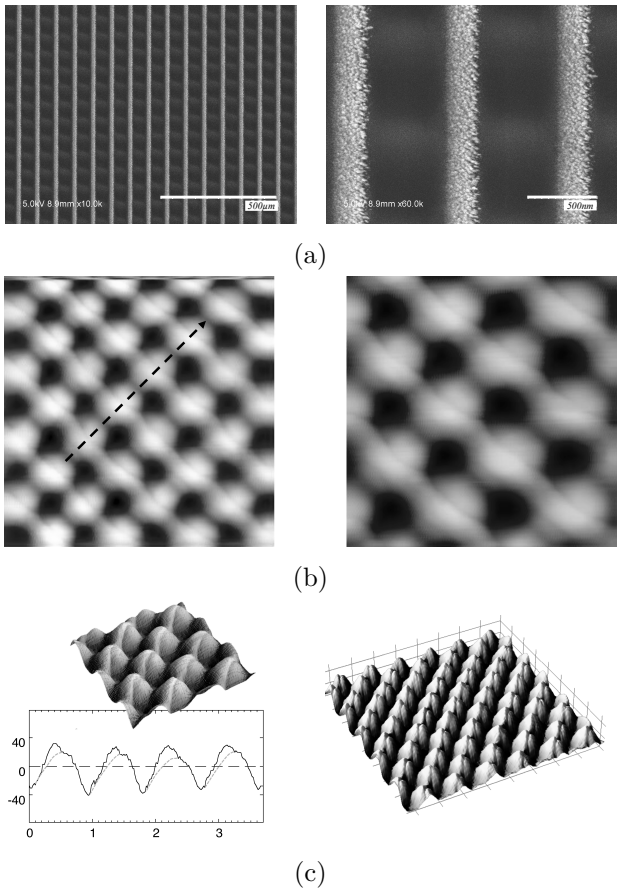

Figure 5.5: Complex pattern obtained by sequential patterning process. (a) SEM images. (b) Shear-force images. (c) 3D representation of the shear-force images. The profile plot in (c) shows the lateral metallic structures, the edge of the gold deposition are indicated by a grey dashed line. Images (b) (c) are reproduced with acceptance of the authors from [3].

surface plasmons resonance is extremely sensitive to environment change (see Chap 6). For an isotropic homogeneous flat thin film, the imaginary part k of the refractive index can be directly determined from the the absorptivity of the azofilm. The real part n can be obtained by ellipsometry measurement which consists of measuring the reflectivity ratio between the p and the s polarization for various angle of incidence. We used the Tauc-Lorentz model [4] to fit the ellipsometry measurement.

Figure 5.6 (a) compares the absorptivity measured by absorption spectroscopy and the data deduced from k measured by ellipsometry. Good fit is obtained for our wavelength range of interest $400 - 1100nm$. Discrepancy is present at short wavelength in the UV because the model we used did

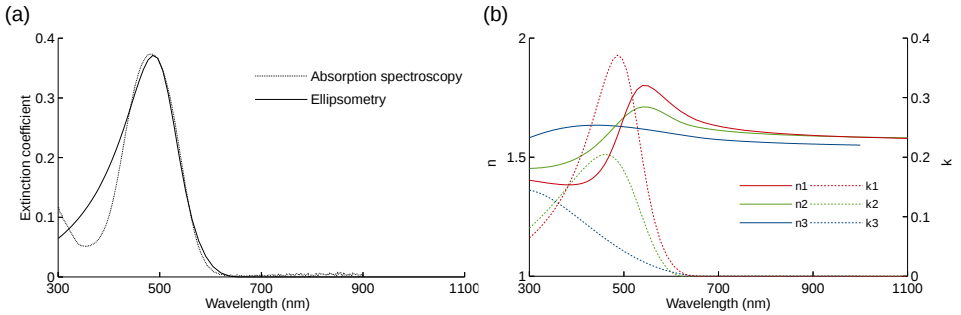

Figure 5.6: Measurement of refractive index. (a) Absorptivity: direct measurement vs ellipsometry. (b) Evolution of the refractive index with the photo-isomerization: $(n1, k1)$ initial film, $(n2, k2)$ after exposure to $7.2J$ and $(n3, k3)$ after exposure to $57.6J$ of a laser beam $\lambda = 488nm$.

not take into account the $n - \pi$ transition of azobenzene. **Figure 5.6** (b) compares the refractive index of PMMA-DR1 film in three cases: initial film $(n1, k1)$, after exposure to 7.2J of a $\lambda = 488nm$ laser beam $(n2, k2)$ and after exposure to $57.6J$ of the same laser beam $(n3, k3)$. We observed changes in both the real and the imaginary part of the refractive index caused by the laser beam used for the photo-inscription.

5.5 Angular-resolved reflectance spectroscopy

The interaction between light and a structured thin film depends not only on the light energy but also on the incident angle of the light beam at the sample surface. In particular, the coupling between the incident light and the proper guided modes of the sample is critically determined by the matching between their phases which only occurs under specific angle of incidence. We thus constructed an experiment set-up (depicted in **Figure 5.7**) which allows measuring the reflectivity spectrum of a collimated light beam under variable angle of incidence. The experiment is mounted on a goniometer, the light source is fixed and the detector is mounted on a movable stage. A glass (BK-7) prism of haft-cylindrical shape is placed at the center of the goniometer. The sample, having $1mm$-thick glass substrate, is optically coupled to the prism using an adaptive refractive index liquid. The prism was made such that when the sample is mounted, the rotation axis of the goniometer falls on its the free surface.

The light source is mounted on a stage allowing to adjust the height and the lateral position with respect to the rotation axis of the goniometer. One can use a laser which emits collimated beam or a white source, for instance, a halogen lamp. In the latter case, one needs to collimate the light beam in

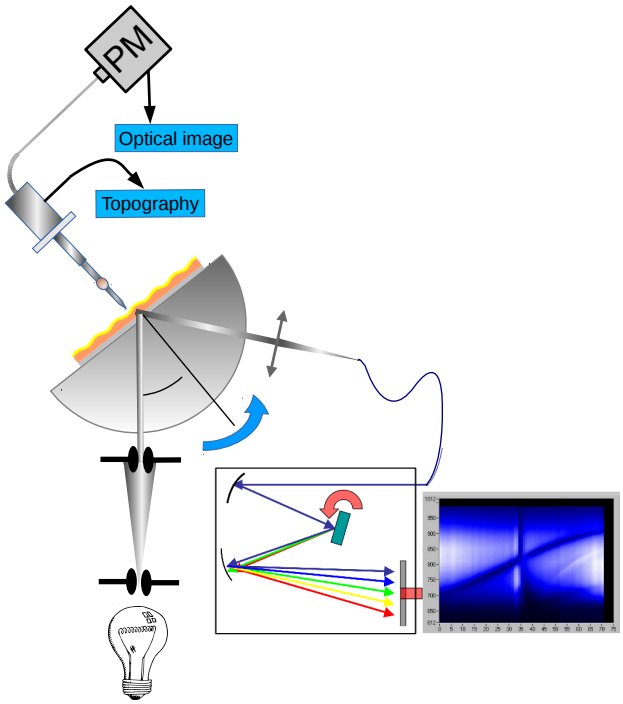

Figure 5.7: Angular-resolved reflectance spectroscopy

order to minimize error on the measured value of the incident angle. The collimation is achieved by passing the light beam through two pinholes. The divergence of the resulted beam is determined by the distance between the two pinholes and their size by the expression (see **Figure 5.8a**):

$$tg(\frac{\alpha}{2}) = \frac{d_1 + d_2}{2l}$$

or

$$\alpha \approx \frac{d_1 + d_2}{l} \quad \text{for} \quad \alpha \ll \pi$$

Collimating white light by this method comes at a cost of losing the light intensity but it avoids the use of lens which introduce also complication due to their optical dispersion. In order to increase to portion of light directing towards the sample, we place the halogen lamp at the focal point of a parabolic mirror. The detector is a photodiode when a laser source is used and a spectrometer when we use a white source. The spectrometer is equipped with a multichannel detector (Ames Photonics Larry-2048) capable of resolving $0.2nm$. In this case, the specular reflected beam from the sample is focused on one end of of an optical fiber to guide the signal into the spectrometer. Care should be taken on the alignment of the light source, the sample and the detector so the same area of the sample is illuminated

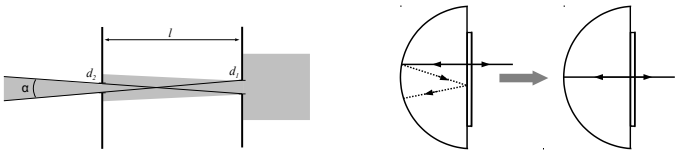

(a) (b)

Figure 5.8: Conditioning of the white source. (a) Collimating using two aligned pinholes. (b) Optical alignment.

as the angle of incidence varies and all the reflected beam is focused to the detector. In order to normalize the measurement, the reflected intensity from a glass surface illuminated under total reflection condition is take as reference.

5.6 Conclusion

We have described the fabrication method of the films and the gratings as well as the characterization of their morphology and of their refractive index. We have also presented the angular-resolved reflectance spectroscopy set-up which allows to measure the dispersion relation of the SPs presented in Chapter 6.

Bibliography

[1] Ke Yang, Suizhou Yang, Xiaogong Wang, and Jayant Kumar. Enhancing the inscription rate of surface relief gratings with an incoherent assisting light beam. *Appl. Phys. Lett.*, 84(22):4517–4519, 2004.

[2] Filippo Fabbri. *Déformation photoinduite dans les films minces contenant des derivés d'azobenzene: effets de polarisation, effets de proximité et effets de contact.* PhD thesis, Ecole Polytechnique, 2009.

[3] Filippo Fabbri. *Déformation photoinduite dans les films minces contenant des derivés d'azobenzene: effets de polarisation, effets de proximité et effets de contact.* PhD thesis, Ecole Polytechnique, 2009.

[4] GE Jellison Jr. Spectroscopic ellipsometry data analysis: measured versus calculated quantities. *Thin solid films*, 313:33–39, 1998.

Chapter 6

Optical and plasmonic properties of periodic gold nano-structures

6.1 Introduction

Resonant surface plasmon (SP) is an electromagnetic mode propagating at a metal/dielectric interface. The electromagnetic field of the SP is maximal at the interface and decays exponentially along its normal axis. This large field confinement allows squeezing light into subwavelength volume therefore is promising for the light-based device miniaturization. Furthermore, SP is highly sensitive to the environment change and has thus potential use in sensing application.

In this study, the SPs are excited by light. As explained in chapter 4, the phase-match condition, equivalent to the conservation of the momentum, must be fulfilled. The polarization condition is in general easily achieved. Light couples to the SPs via the evanescent wave generated, for instance, under total reflection or by the scattering from surface corrugation. The optical excitation of the SPs by surface grating is a particular case of the latter process in which the surface corrugation exhibits a periodic structure. The interaction of the SPs and the gratings has recently received renewed interest because of their role in the Surface Enhanced Raman Scattering (SERS) [1], in giving rise to photonic band gaps [2, 3], in the enhanced optical transmission [4] and in the design of novel plasmonic devices [5].

Azopolymer constitutes a unique and attractive platform for material fabrication to harness the optical and the plasmonic properties. In particular, the photo-induced SRG generation in azobenzene-containing film combined with metal deposition offers a convenient and flexible way to

elaborate metal gratings. The size and the shape of the gratings can be easily tailored to the specific properties [6–10]. Moreover, metal deposited at glancing incidence takes advantage of the shadow effect and offers even more tuning possibility of the metal structure. Finally, a particular feature of the photo-patterning using azofilm is the possibility to continuously adjust the structure by illumination which can hardly be achieved with other patterning methods. This opens up the interesting perspective of optical manipulation the SPs.

In this chapter, we study the optical and the plasmonic properties of the metal gratings fabricated by using the photo-induced mass transport in azofilm. We consider two types of metal grating: continuous metal film and arrays of metal nanostructures, obtained by metal evaporation at normal and grazing incidence, respectively.

6.2 Sample fabrication

Our experiments are conducted on a $250nm$-thick PMMA-DR1 film spin-coated on glass substrate. The surface gratings are obtained by direct exposure to an optical interference pattern to activate the photo-isomerization of the azo dye. Green ($\lambda = 532nm$) and blue lasers ($\lambda = 488nm$) are used to create the interference patterns. The beams' polarizations are oriented at $+45°/-45°$ with respect to the plane of incidence to achieve the optimal inscription efficiency [11, 12]. **Figure 6.1** (b1, b2) illustrates the surface patterning process. The sample is illuminated at the angle of incidence $\theta = 45°$ through its glass substrate which is optically coupled to a glass prism. The interference pattern inscribes a 1-dimensional (1D) SRG of the same period. Subsequent patterning allows to achieve more complicated SRGs such as the 2-dimensional (2D) pattern shown in **Figure 6.1** (c1, c2). The kinetics of the surface patterning process is measured by SNOM. The same process was used to produce the 2D egg-shell surface motif shown in **Figure 6.1**(c1).

Au is evaporated on the 1D and 2D patterned surface to produce different hybrid metal/polymer structures, as shown in **Figure 6.2**. The evaporation angle ϕ allows tailoring the deposited metal structure. **Figures 6.2** shows SEM images of the *Au* structures deposited on the 1D and 2D structured surfaces in two deposition configurations. When $\phi = 0°$, one obtains a continuous corrugated *Au* film (Fig. 6.2(a1-a3)), when $\phi \approx 90°$, *Au* is only deposited on one side of the surface reliefs (Fig. 6.2(b1-b6)), resulting in *Au* stripe or grid pattern depending on the template surface. The shear-force topography profile in **Figure 6.2** (b5) clearly shows the lateral *Au* deposition whose the edges are indicated by the gray dashed line [13].

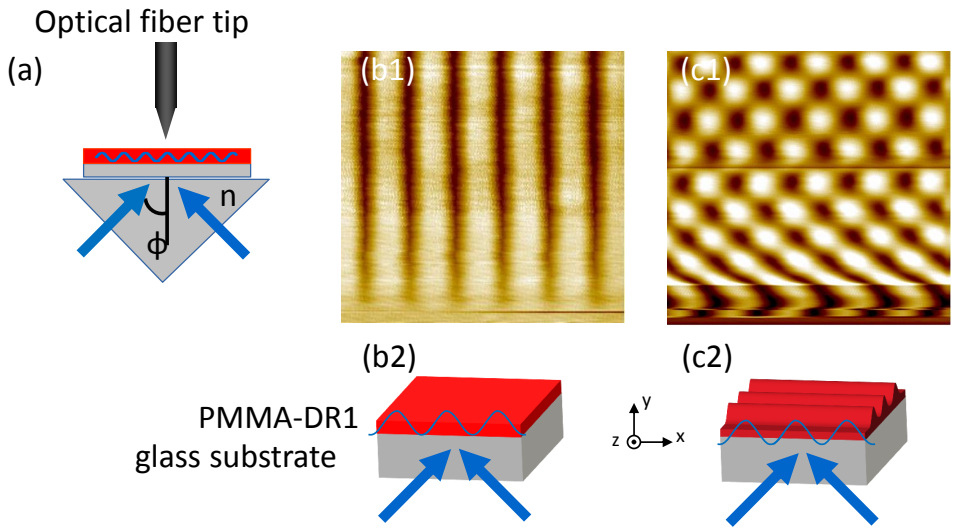

Figure 6.1: Optical patterning of SRG with *in situ* monitoring. (a) Experimental set-up. (b-c) Optical patterning of (b1-2) 1D and (c1-2) 2D structure.

6.3 Numerical modelling

6.3.1 Rigorous Coupled-Wave Analysis

Rigorous Coupled-Wave Analysis (RCWA) is a prominent method for calculating the electromagnetic properties of surface grating thanks to its simplicity, straight forward numerical implementation and fast convergence [14]. First formulated by Moharam and Gaylord in the 80*s*, it has received tremendous improvement to improve the numerical stability and the convergence speed [15–20]. Here, we used RCWA to study the optical properties of the continuous *Au* film having 1D structure illustrated in **Figure 6.3** (a).

The grating problem consists of the wave equation, the boundary conditions associated with the grating structure and the optical parameters (permittivity and permeability) of the studied media. The wave equation in the differential form reads:

$$\left(\frac{\partial^2}{\partial x^2} + \frac{\partial^2}{\partial y^2} + k_0^2 \mu\epsilon\right) F = 0 \tag{6.1}$$

where F is a field component in the z direction, $k_0 = \frac{2\pi}{\lambda}$ is the amplitude of the wavevector in vacuum, λ is the vacuum wavelength, ϵ is the permittivity, μ is the permeability. In RCWA, a film with arbitrary surface profile is approximated by a staircase structure consisting of binary layers (see **Figure 6.3** (b)) and the boundary conditions are reformulated to the new profile

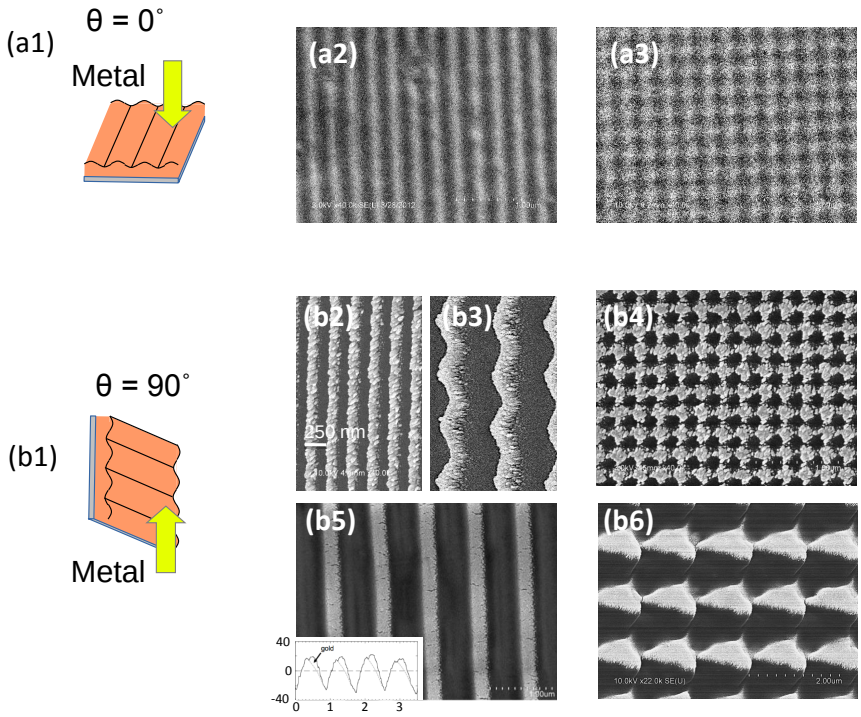

Figure 6.2: Thermal evaporation of Au at glancing incidence. (a) Normal incident deposition $\phi = 0°$ on (a2) 1D and (a3) 2D structure. (b) Grazing incident deposition $\phi \approx 90°$ on (b2, b5) 1D structure with the Au flux perpendicular to the grating and (b2, b4, b6) 2D structure with different orientations of the grating with respect to the Au flux. The inset of (b5) clearly shows the lateral metallic structures, the edge of the Au deposition are indicated by a gray dashed line [13].

[17]. The problem is next transformed into an eigenvalue problem by using Fourier analysis. The accuracy of the solution depends on the number of the Fourier harmonics used in the computation and the number of the binary layers in the approximated structure [17].

6.3.2 Implementation

We use alternatively two different implementations of the RCWA[1], a free version written by Pavel Kwiecien [21] and another provided by the Institut d'Optique. The sinusoidal profile is modeled by staircase structure illustrated in **Figure 6.3** (b). The numbers of the staircases and of the Fourier harmonics are determined by the balance between accuracy and the compu-

[1] both written in Matlab^{TM}

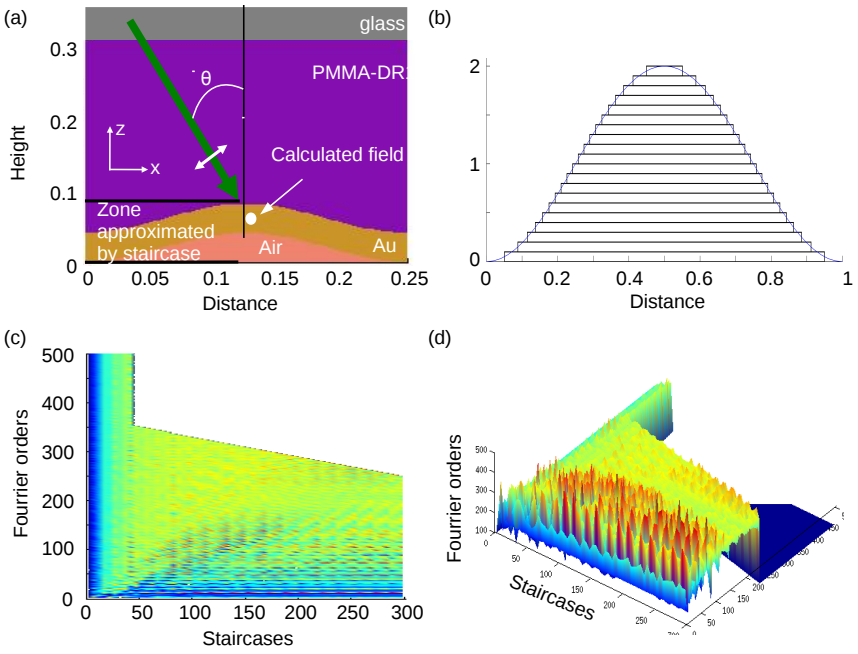

Figure 6.3: Implementation of RCWA. (a) The sample structure. (b) Staircase approximation for the corrugated region. (c) Convergence in function of the number of Fourier orders and of staircases. (d) 3D representation of (c).

tation time. An example of such study is illustrated in **Figure 6.3** (c, d). Here, we plot the calculated electromagnetic field at a point in the middle of the *Au* layer as a function of the numbers of the Fourier harmonics and of the number of the staircases. We observe that the calculated field converges at large values of both parameters.

An inherent issue of the staircase approximation in RCWA is the structural singularities at the stairs' edges. They produce large fluctuation in the calculated electric field under p polarization [22] which is expected for an actual staircase structure but is inaccurate in describing the optical field at a smooth surface. Nevertheless, it has been shown that the fluctuation decays rapidly to the correct values at far enough distance from the edges. Moreover, the spatial extent of the fluctuation decreases with the number of stairs. There exist several numerical techniques to overcome this singularity issue [20, 22]. Here, we simply choose the number of the staircases and of the Fourier harmonics to reduce the extent of the fluctuation and apply apodization to the graphic representation of the field.

6.4 Flat *Au* film

6.4.1 Normal incident deposition

Continuous *Au* films are obtained by evaporating *Au* at normal incidence. The films' thickness depends on the quantity of deposited *Au*.[2] **Figure 6.4** compares the reflectivity of the *Au* films deposited on (a) a raw glass substrate and (b) a PMMA-DR1 film supported by a glass substrate. The sample is illuminated under the Kretschmann's configuration[3] by a red laser beam of wavelength $\lambda = 633nm$ under p and s polarization.

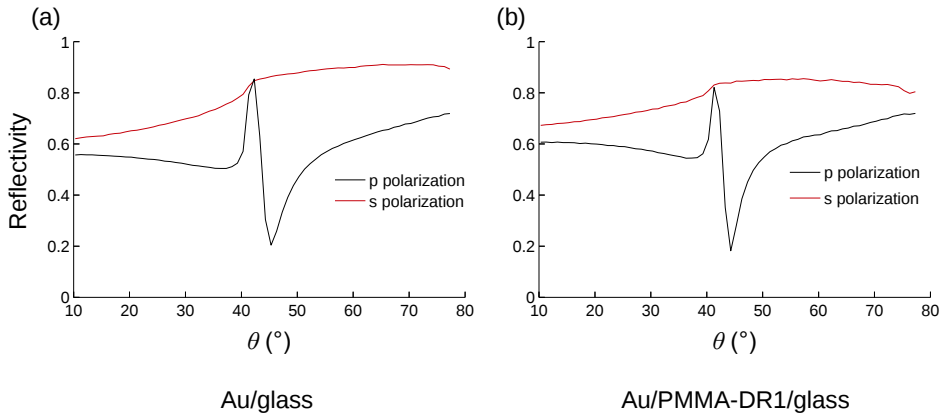

Figure 6.4: Far-field reflectivity measurements on flat $40nm$-thick *Au* layer deposited on raw glass substrate or on PMMA-DR1 at normal incidence. The samples are illuminated by red laser beam ($\lambda = 633nm$, beam size $1mm$) under both p polarization and s polarization (a)*Au* on glass. (b) *Au* on PMMA-DR1/glass.

Under p polarization, the *Au*/air SP is coupled to the evanescent optical field generated under total reflection. It gives rise an abrupt variation of the reflectivity which is only observed under p polarized illumination on both the samples shown in **Figure 6.4**. One notes also a slight difference in the reflectivity under s polarization between the two samples. The reflectivity of the *Au*/PMMA-DR1/glass sample decreases at large angle of incidence because of the guiding effect of the PMMA-DR1 film. In fact, for $\lambda = 633nm$, the refractive index of PMMA-DR1 $n_{PMMA-DR1} = 1.64$ is slightly higher than $n = 1.51$ of glass. Therefore, when the reflected light at the *Au*/PMMA-DR1 interface arrives at the PMMA-DR1/glass one, it is partially reflected back into the film and so on. The PMMA-DR1 layer

[2] In our study, no adherent (*Chromium*, *Nickel*, etc) layer is used between the *Au* and the substrate to avoid SPs loss.

[3] See **Figure 4.2** (a) in Chapter 4.

thus stocks a fraction of the incident energy which increases with the angle of incidence.

6.4.2 Glancing incident deposition

Au films obtained by glancing angle deposition (GLAD) is composed of elongated Au grains. This stems from the shadowing effects and the competition between nucleating grains [23]. The higher points of the film intercept the flux, hinder the growth of the lower points. This process results a porous film with isolated Au rods inclined towards the Au source. The shape ratio of these grains depends on the shadowing geometry and the diffusion rate of the adsorbed Au atoms at the surface [24, 25]. While the former is determined by the angle of incidence, the later depends on the competition between the deposition rate and on the surface mobility which depends on the chemical nature of the grains and the substrate. It was reported that the elongated structure of the Au grains has polarizing effect [23]. The SP coupling which depends on the light polarization would exhibit asymmetric behaviours on such surface.

Figure 6.5 shows the reflectivity measurement performed on a Au film obtained by GLAD. The nominal deposition rate is $1nm/s$ and the incidence is close to 90° with respect to the surface normal. The film is excited by a red laser beam $\lambda = 633nm$ under p and s polarizations under Kretschmann's configuration. Two sample configurations are considered: the Au columns are either (a1) perpendicular or (a2) parallel to the plane of incidence.

Considering the Au film on glass, the reflectivity prior to the total reflection is larger when the light polarization is parallel to the Au columns, i.e. s polarization in (b1) or p polarization in (b2). This asymmetric behaviour also applies for the SP coupling. Under p polarization, the reflectivity minima beyond the total reflection limit indicate the excitation of the Au/air SP. This coupling occurs at larger angle when the light polarization and the Au columns are perpendicular (b1) than when they are parallel (b2). The reflectivity minimum associated with the former case is also wider. The SP propagating perpendicular to the Au columns would experience more collision with the grain boundary, inducing loss, which explains the widening and the shift to larger angle of the coupling. However, the reflectivity minima are close to zeros which means that the incident energy is totally transferred to the SP modes. In such Au films, it is possible to excite the SPs at a specific direction determined by the asymmetry of the surface morphology.

In **Figure 6.5** (c1, c2), the Au films deposited on PMMA-DR1 surface exhibit much less optical asymmetric compared to the one deposited on glass, even though the samples are obtained in the same deposition. This is probably explained by the local liquidification of the PMMA-DR1 film

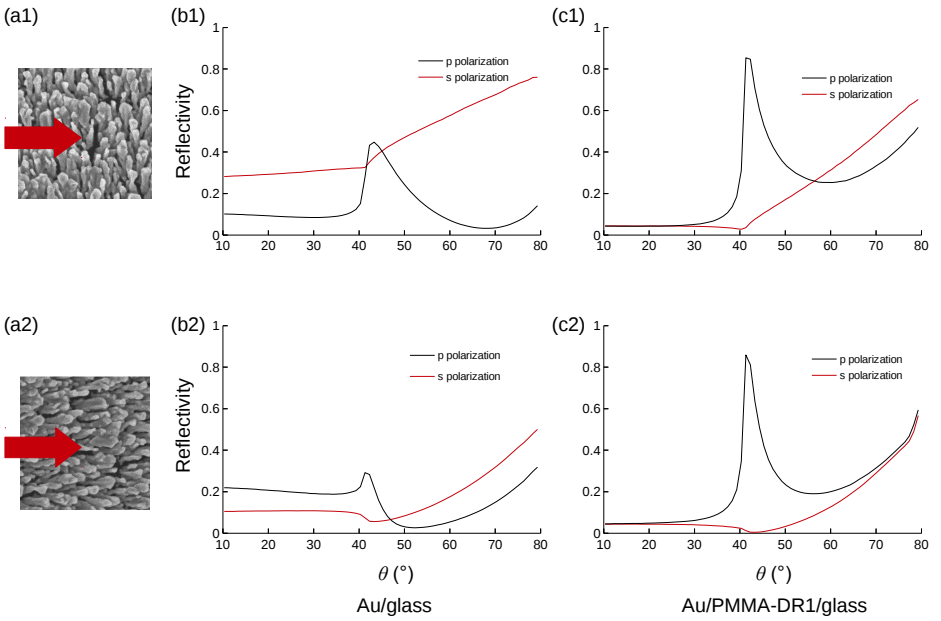

Figure 6.5: Far-field reflectivity measurements on a flat $40nm$-thick Au layer deposited at grazing incidence on (b) glass and (c) on PMMA-DR1. The samples are illuminated by red laser beam ($\lambda = 633nm$, beam size $1mm$) under p polarization and s polarization. (a1, a2) indicate the orientation of the Au film with respect to the plane of incidence. (b1, b2) Reflectivity of Au film deposited on glass. (c1, c2) Reflectivity of Au film deposited on PMMA-DR1/glass. The nominal deposition rate is $1nm/s$ and the incidence is close to 90° with respect to the surface normal.

($T_g = 120°$) by the heat from the Au particles. In the remaining sections, since we only deal with Au films or structures deposited on PMMA-DR1, the optical asymmetry due to the surface morphology is considered negligible.

6.5 Continuous nanostructured Au film

In this section, we investigate the optical and the plasmonic properties of the continuous corrugated Au thin films. These films, shown in **Figure 6.2** (a2, a3), are obtained by Au deposition at normal incidence on patterned PMMA-DR1 thin film supported by glass substrate. The SPs are optically excited under Kretschmann's configuration with the sample optically coupled to a cylindrical glass prism. Under this conditon, the Au/air SP is excited by the evanescent field generated by the incident light under total reflection and the Au/PMMA-DR1 is only excited thanks to the surface gratings.

6.5.1 1D structure

We first consider continuous Au film which is periodically corrugated in one direction. A $40nm$-thick Au film is deposited on a PMMA-DR1 surface having 1D structure of lattice constant $250nm$ and of height $40nm$. The obtained Au film has wavy shape conforming with the PMMA-DR1 surface underneath.

Far-field reflectivity

Figure 6.6 shows the far-field reflectivity and the near-field transmission data. The sample is illuminated through the cylindrical prism by a red laser beam ($\lambda = 635nm$, beam size $1mm$) under p and s polarizations. Two configurations of the sample are studied, depicted in **Figure 6.6** (b, c)) where the grooves are parallel (**PARAL**, $--$) or perpendicular (**PERP**, —) to the plane of incidence. These measurements are compared to the one conducted on a flat Au film of the same thickness, (**FLAT**, $++$).

Under p-polarized illumination, the SP resonances manifest as reflectivity dips at the angle of incidence θ fulfilling the phase match condition **C2**.[4] At $\theta = 45.5°$, which is beyond the total reflection limit ($\theta_c = 40.3°$), a reflectivity dip is observed in all the three measurement configurations. This dip corresponds, by **C2**, to the excitation of the Au/air SP. In the **PERP** configuration, an additional dip is observed at $\theta \approx 22°$ which, by **C2**, is due to the excitation of the Au/PMMA-DR1 SP via the grating diffraction.

Under s-polarized illumination, no sign of SP coupling is observed. In the **FLAT** and the **PERP** configurations, the polarization condition **C1** is not fulfilled. In the **PARAL**, the SP coupling is prohibited by the phase-match condition **C2**. We also note a gradual drop in the reflectivity at large angle of incidence. This drop is explained by the increasing leak of energy into the guided mode of the PMMA-DR1 layer. Indeed, the refractive index of the PMMA-DR1 layer ($n_{PMMA-DR1} \approx 1.64$) is higher than the one of glass substrate ($n_{glass} \approx 1.51$) at this wavelength $\lambda = 635nm$.

Near-field imaging

The excitation of the Au/air SP resonance give rise to the same far-field reflectivity for the three sample configurations. However, in near-field measurement, they shows distinctive features which correlates strongly to the structure of the Au surface. The topographic and optical near-field measurements are conducted in the **PERP** configuration at the excitation of the Au/air SP ($\theta = 45.5°$). **Figure 6.6** (d) shows the topographic image

[4] See 4.2

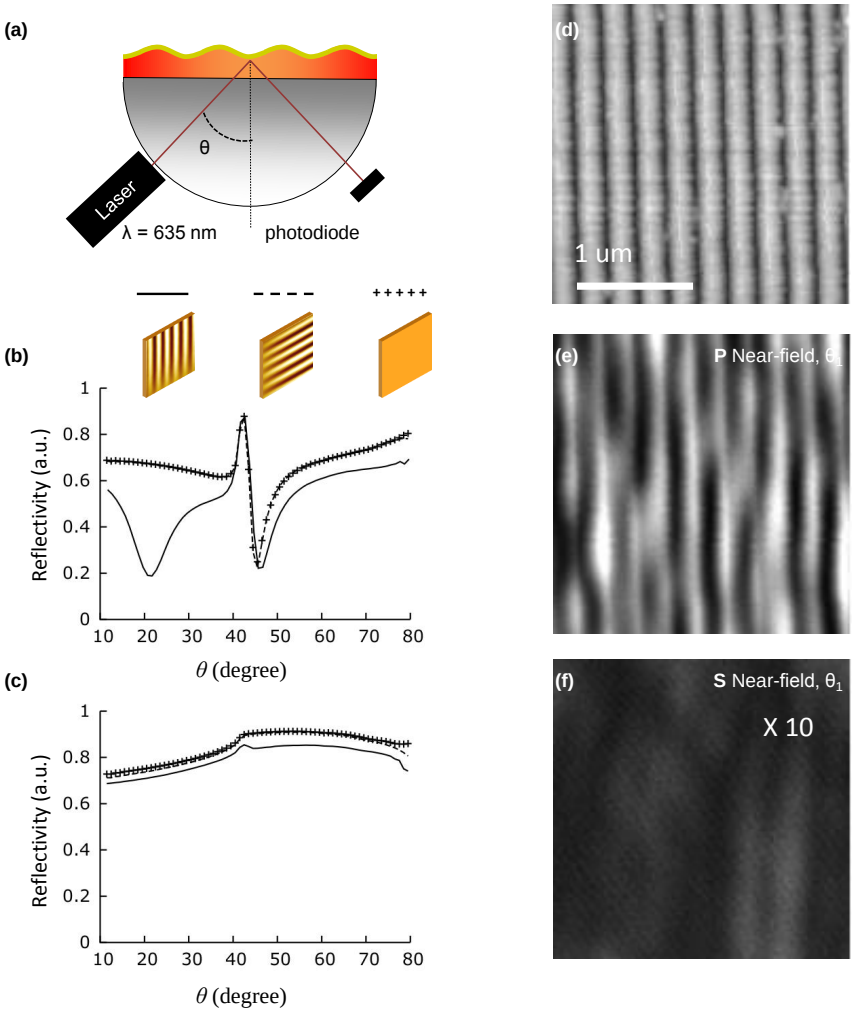

Figure 6.6: Far-field reflectivity and near-field transmission measurements carried out on Au film with 1D pattern. The sample is illuminated by red laser ($\lambda = 635nm$, beam size $1mm$). (a) experimental set-up. (b, c) reflectivity under p and s polarizations for three sample configurations: $(++)$ flat surface, $(--)$ and $(—)$ 1D-patterned surface with the grooves perpendicular or parallel to the plane of incidence, respectively. (d) $5\mu m \times 5\mu m$ topographic image of the sample surface. (e, f) near-field transmission measured under p and s polarizations.

of the $40nm$-height $250nm$-period SRG while the optical transmitted near-field images are shown in **Figure 6.6** (e, f) respectively for p and s-polarized illumination.

The features of the optical near-field are different under p-polarized and s-polarized illumination. Under p polarization, the contrast in the optical image shows a periodic structure of the same pace and in opposite phase with respect to the surface topography. This periodic optical pattern disappears when the tip is set to $1\mu m$ away from the sample surface. We observe here the confinement of the optical field in the normal direction to the surface associated with the Au/air SP. Under s polarization, the absence of SP coupling explains the much weaker near-field intensity. In **Figure 6.6** (f), even though the optical intensity is multiplied by a factor of 10, it still appears much darker than the one obtained under p polarization. There is a small intensity fluctuation which is not correlated with the topographic structure which remains even when the tip is withdrawn to 1 μm from the sample surface. We thus attribute it to the optical field scattered by the random defects of the Au surface.

To gain more insight into the field confinement of the SPs, we compare the experimental and the calculated near-field of the current condition ($\theta = 45.5°$) with two other ones: $\theta = 21.5°$ corresponding to the reflectivity dip before the total reflection in **Fig 6.6** ($-$) and $\theta = 58.9°$ which is beyond the total reflection limit but far from any SP coupling. We only consider the **PERP** configuration. **Figure 6.7** shows the measured near-field profiles along the direction of the grating wavevector for these three conditions. The first column (a1-a3) shows the results for $\theta = 21.5°$: (a1, a2) show the measured and (a3) shows the calculated near-field. The equivalent data for $\theta = 45.5°$ and $\theta = 58.9°$ are shown in (b1-b3) and (c1-c3), respectively. All the measurements are performed at the same spot on the sample surface.

At $\theta = 21.5°$ (**Figure 6.7** (a1-a3)), the Au/PMMA-DR1 SP is only excited under p polarization. The calculated optical intensity reveals the field enhancement close to the Au/PMMA-DR1 interface. However, this field enhancement is not observed experimentally since the field is substantially attenuated as it penetrates across the Au layer. Moreover, the transmitted optical field contains also the propagating component since the angle of incidence is smaller than the total reflection limit. This propagating component gives rise to a homogeneous optical intensity across the sample surface which dominates over the near-field evanescent signal.

In the cases of $\theta = 45.5°$ and $\theta = 58.9°$ which are both beyond the total reflection limit, the field enhancement and confinement associated with the SP resonance is evidenced by comparing the measured and the calculated near-field (**Figure 6.7** (b, c)). Under s polarization, no field enhancement is observed as the SPs are not excited and the same optical near-field intensity is measured in both cases. This is expected from our previous report on the far-field reflectivity (see **Figure 6.6** (c)). Under p polarization, the

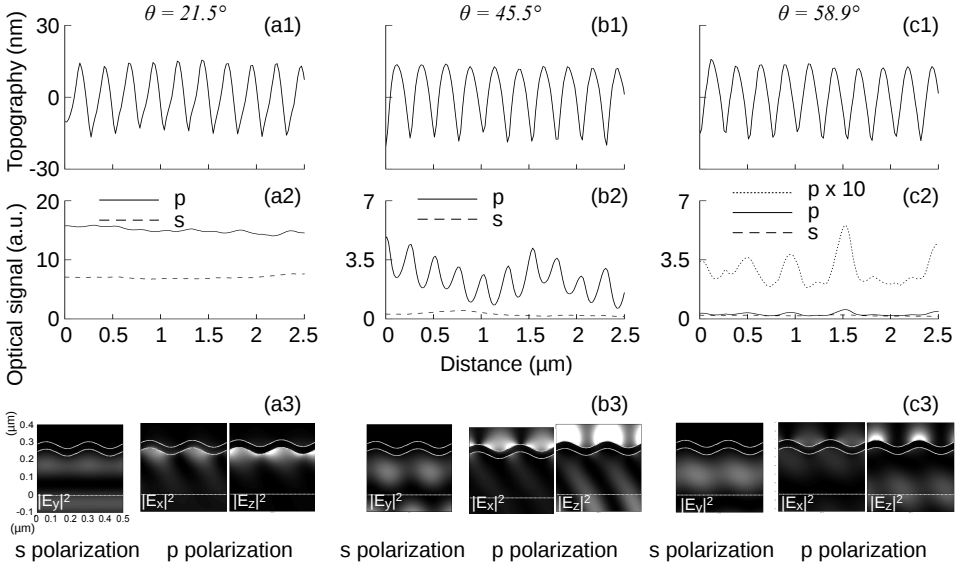

Figure 6.7: Measured and calculated near-field when the 1D patterned Au film is illuminated by a laser beam of $\lambda = 635nm$ at (a) $\theta = 21.5°$, (b) $\theta = 45.5$ and (c) $\theta = 58.9°$.

excitation of the Au/air SP at $\theta = 45.5°$ is evidenced by the strong optical measured near-field. This enhanced near-field exhibits the same modulation as the surface topography. Nevertheless, at $\theta = 58.9°$, a periodic pattern is also revealed in the measured optical near-field when it is multiplied by a factor of 10 (**Figure 6.6** (c2)). This points to the role of the surface modulation in confining the optical near-field in the parallel direction to the surface and the confinement is enhanced because of the SP resonance.

Finally, in the calculated near-fied at SP resonace ($\theta = 45.5°$, **Figure 6.7** (b)), only $|\mathbf{E_x}|^2$ is in π-phase with respect to the surface topography. The measured optical near-field reveals thus only the $\mathbf{E_x}$ component, in agreement with the well-known better sensitivity of an apertured optical fiber probe to this field component [26]. From the calculation, it can be speculated that $\mathbf{E_z}$ exhibits much stronger intensity and is confined to the peaks of the topograpic structure.

Surface grating can modify the SP near-field distribution giving rise to a stationary field distribution. The near-field is largely enhanced under SP resonance, especially the field component perpendicular to the surface.

The dispersion relation of the SP

The propagation of the SP is characterized a dispersion relation showing the dependence of its energy $\hbar\omega$ (ω is the angular frequency) on its wavevector k_{SP} (equivalent to the momentum $\hbar k_{SP}$). The dispersion relation can be established by the reflectivity spectroscopy at varied angle of incidence. The Angular Resolved Spectroscopy set-up was developed for this purpose.[5] The sample is illuminated by a broadband light ($400nm - 1100nm$) and the reflected spectrum is analyzed. The dispersion relation of the SPs are revealed by representing these spectra as proportional gray color in the ($k_{\|}$, $\hbar\omega$) coordinates.

Figure 6.8 (a, b) shows the measured and the calculated reflectivity spectra of a 1D-patterned continuous Au film illuminated under the **PERP** configuration. Two dark curves are observed both in the experimental and the calculated data showing the trajectories of the reflectivity dips associated with the SP resonances (see **Figure 6.6** (c)). They corresponds the trajectories of the zeros of the scattering matrix which, together with the poles, consist the manifestation the SP resonances [27]. In fact, the dispersion relation of the SP is associated with trajectory of the poles. Nevertheless, in highly conducting metal like Au, the real part of the poles and the zeros are almost equal [27] therefore the dispersion relation are usually attributed to the trajectory of the zeros.

Figure 6.8 (c) explains schematically the formation of these dark curves. Here, the measured data fall into the positive quadrant of $\mathbf{k}_{\|}$. The green lines are the dispersion of light in air ($k = \frac{\omega}{c}$) and in glass ($k = n \times \frac{\omega}{c}$ where n is the refractive index of glass). The red curves are the dispersion of the SPs propagating on the different interfaces of the Au film. By symmetry, the same curves exist in the negative quadrant of $\mathbf{k}_{\|}$. Due to grating diffraction, these curves are replicated and shifted along the $k_{\|}$-axis by an integer amounts of the grating vector $k_a = \frac{2\pi}{a}$ where a is the grating constant. In particular, the curves in the $k_{\|} < 0$ quadrant are shifted by k_a and intersect with the ones in the $k_{\|} > 0$ quadrant. Guided by this schematic representation, one can identify the different dispersion relations in **Figure 6.8** (a) and (b). Thus, the bright band of positive slope in (a) corresponds to the light line in air. The dark band next to it on the right (labelled i) reveals the dispersion relation of the Au/air SP. The second dark band having negative slope (labeled ii) in (a) and (b) is the dispersion relation associated with the Au/PMMA-DR1 SP.

The dark band (i) reveals an energy band gap at $\hbar\omega = 2.25eV$. Indeed, it comprises an increasing and a decreasing part connected by a bending part at $\hbar\omega = 2.25eV$. Referring to **Figure 6.8** (c), this bending occurs at

[5] See 5.5

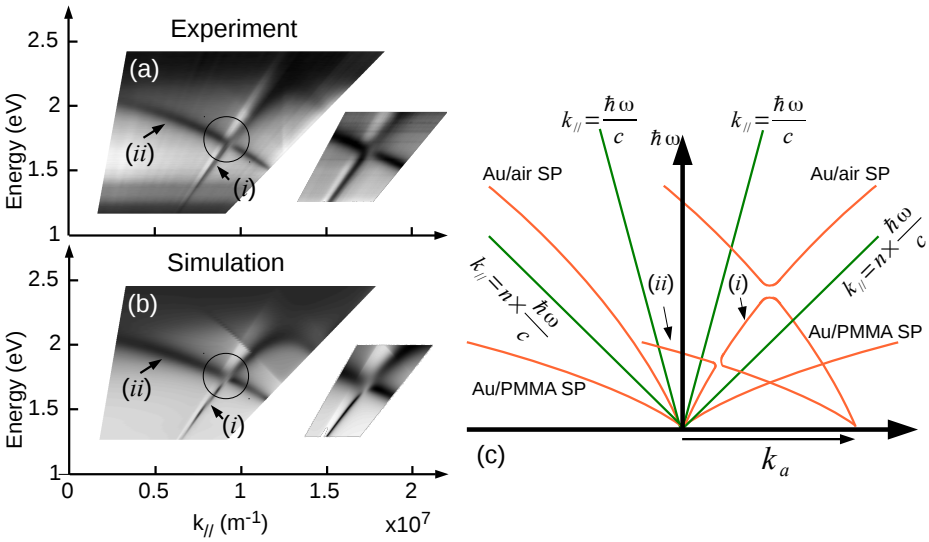

Figure 6.8: The dispersion relations of the SPs constructed from the reflectivity spectra at various angle of incidence. (a) The experimental measurement. (b) Calculated dispersion diagram by RCWA. (c) Schematic representation of the dispersion relations.

the crossing between the dispersion relation of the Au/air SP and an equivalent curve describing the SP which propagates at the same Au/air interface but in the opposite direction. The second dispersion relation belongs to the negative side of $k_{\|}$ and is shifted left by k_a due to the grating diffraction. The bending consists the low energy edge of the band gap. The high energy edge of this gap is not revealed because in its corresponding energy range, the halogen lamp provides very low output and the absorption of the DR1 film becomes important. This energy band gap arises from the interaction between the two counter-propagating SPs of the Au/air interface. As explained in [2], they interfere and give rise to two stationary electromagnetic waves whose energies correspond to the two edges of the band gap.

Apparent k-gap in the trajectory of the zeros

There exists a second intersection (circled in **Figure 6.8** (a)) which brings about the simultaneous excitation of two SPs, each is associated with one interface of the Au film, the Au/air and the Au/PMMA-DR1 interfaces. On an optically thick metal film, since the SPs do not sense the presence of the other, their dispersion curves will simply cross without modifying each other. However, if the metal film is sufficiently thin, the interference of the SPs' electromagnetic field may occur. Such interaction of the SPs of the different metal interfaces across the film is termed "cross-coupling" [28–

30]. It has been reported that the cross-coupling modifies the dispersion curves at their intersection and may give rise to an anti-crossing [30, 31]. The insets in **Figure 6.8** (a) and (b) provide a zoom into the circled area and reveal a small gap in the $k_{\|}$ direction both in the experimental and the calculated dispersion data. The reflectivity dips which consist the edges of this apparent k-gap must be related to SP excitation since no propagating diffracted wave is predicted or observed under this condition of (ω, $k_{\|}$).

The apparent k-gap is seen both in the experimental and the calculated data (**Figure 6.8** (a, b)) at $\hbar\omega = 1.69eV$ ($\lambda = 733nm$). The zooms of the circled area given in the insets are established from the (a) measured and the (b) calculated reflectivity spectra using the angle increment $\Delta\theta = 0.1°$. Thus, the precision of the wavevector is about $\Delta k_{\|}/k_{\|} = 0.2\%$.[6] In the experimental data, ratio between the gap width Δk_g and the wavevector at the center of the gap $k_{\|c}$ is $\Delta k_g/k_{\|c} \approx 7\%$. The calculated data in **Figure 6.8** (b) shows an apparent k-gap at $\lambda = 733nm$. The angle of incidence corresponding to the gap's edges are: $\theta_1 = 44.3°$ and $\theta_2 = 48.7°$, giving also $\Delta k_g/k_{\|c} \approx 7\%$, in good agreement with the experimental data. The apparent k-gap is much larger than the experimental uncertainty in determining $k_{\|}$.

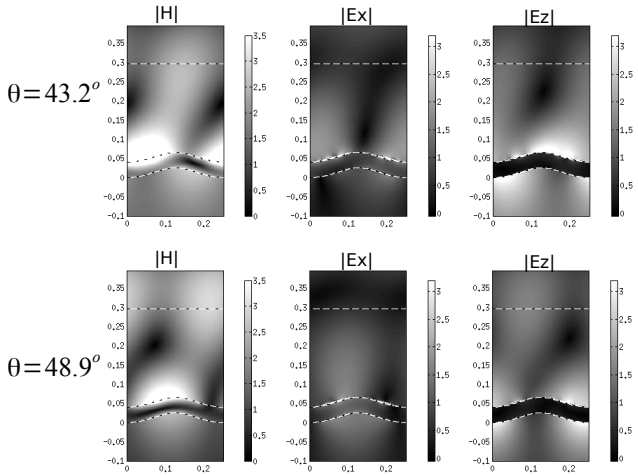

Figure 6.9: (a,b) Trajectories of the poles (red for the Au/air SP and black for the Au/PMMA-DR1 SP) and the zeros. The inset of (a) is represent the trajectories of the pole with both the real and the imaginary part of $k_{\|}$.

The existence of a k-gap in the dispersion curves is highly questionable

[6] Value corresponding to center of the gap.

because the vertical edges of such gap imply infinite group velocity of the involved wave. In fact, understanding the apparent k-gap in **Figure 6.8** (a) and (b) requires distinguishing the trajectories of the poles and the zeros which is so far unnecessary. These trajectories are calculated and reported in **Figure 6.9** (a, b) in the $(k_0, k_\parallel)$ coordinates, here $k_0 = \frac{2\pi}{\lambda} = \frac{\omega}{c}$ is equivalent to $\hbar\omega$. We are interested to the behaviour of the poles' and the zeros' trajectories in the proximity of the cross-coupling point, i.e. the intersection between the trajectories associated with the Au/air and the Au/PMMA-DR1 SPs. Far from the cross-coupling, the dispersion relations of the SPs given by the poles' trajectories is well approximated by the trajectory of the zeros which justifies our discussion made so far on the dispersion relations. However, close to the cross-coupling, the trajectories of the poles and the zeros deviate considerably from one another. In particular, the trajectories of the poles (red for the Au/air SP and black for the Au/PMMA-DR1 SP) simply go by without influencing each other at the crossing point. Indeed, the 3D plot, taking into account both the real and the imaginary parts of $k_\parallel$, in the inset of **Figure 6.9** (a) reveals that the trajectories of the poles do not actually intersect since the imaginary parts of the $k_\parallel$'s at the crossing are not equal.

On the other hand, the crossing between the trajectories of the zeros (the green curves in **Figure 6.9** (a, b)) does exhibit a k-gap. It is possible to explain this apparent k-gap by an interference process described in [27, 32]. The reflected wave from a continuous corrugated Au film can be expressed as:

$$I = r^2 = \left(r_0 + \frac{X_1}{k_\parallel - k_1^r} + \frac{X_2}{k_\parallel - k_2^r} \right)^2 \tag{6.2}$$

where $r_0 = \frac{E_r}{E_{inc}}$ is the amplitude coefficient of reflection of a semi-infinite Au medium, E_{inc} and E_r are the incident and the reflected electric field, k_i^r $(i = (1,2))$ are the zeros of the two SP resonances, X_i $(i = (1,2))$ contains the amplitude and the phase of the re-radiated wave of the SPs, their values depend on the grating structure and the optical indices. The resonant character of the SP means that $r_0 + \frac{X_i}{k_\parallel - k_i^r}$ admits a solution while far away from this solution, $\frac{X_i}{k_\parallel - k_i^r} \approx 0$.

- In this description, if $k_1^r \neq k_2^r$, there exist two distinct values of $k_\parallel$ which are solutions of $r_0 + \frac{X_i}{k_\parallel - k_i^r} = 0$ for $i = 1$ or $i = 2$ exclusively. If moreover, k_1^r and k_2^r are well separated, it follows that $I \approx 0$ at these $k_\parallel$. These two distinct solutions give rise to the two reflectivity minima observed in **Figure 6.6** (b). The measured value of I does not attain exactly zero mainly because the k_i^r are complex.[7]

[7] and partly because the incident beam is not completely polarized.

- At the crossing point of the trajectories of the zeros, we have $k_1^r = k_2^r = k^*$. $r_0 + \frac{X_i}{k_\parallel - k_i^r}$ $(i = 1, 2)$ now admit the same solution. It follows that $r = r_0 + \frac{X_1}{k_\parallel - k_1^r} + \frac{X_2}{k_\parallel - k_2^r}$ changes sign twice as $k_\parallel$ goes from smaller to larger than k^*, as illustrated in **Figure 6.9** (c). There exist thus two values $k_1^* < k^* < k_2^*$ such that $I(k_i^*) = r(k_i^*)^2 = 0$. As $k_\parallel$ varies from k_1^* to k_2^*, $I(k_\parallel)$ passes by a local maximum, as illustrated in **Figure 6.9** (d). This interference scheme explains thus the creation of the apparent k-gap at the crossing of the trajectories of the zeros associated with two different SPs. k_1^* and k_2^* make up the edges of this apparent k-gap.

In this sense, the apparent k-gap reported here stems from the interference of two SPs propagating at the two interfaces of the Au film. Note that the cross-coupling should involve two counter propagating SPs to give rise to an apparent k-gap. When they propagate in the same direction, as was shown in [31], the gap arising from the cross-coupling is oblique in the ($\hbar\omega$, $k_\parallel$) coordinates.

The periodic corrugation in a Au film gives rise to the confinement of the SP electromagnetic field in the direction parallel to the film plane. The field is maximized at the peaks of the structure where it is polarized along the normal direction. SNOM allows to evidence such localization as well as the expected field-enhancement due to SP resonances. The angular-resolved reflectivity spectroscopy gives insight into the trajectories of the zeros which are, in most cases, good approximation of the dispersion relations of the SPs. At the intersection of the trajectories of the zeros associated with the SPs propagating at the different metal interfaces, anti-crossing arises from the interference of the SPs' and the incident wave's electromagnetic field. An apparent k-gap can be observed in the reflectivity spectra when the interference involves two counter propagating SPs. However, according to calculation, no k-gap actually occurs in dispersion relation of the SPs.

Calculated near-field at the apparent k-gap

We are now interested in the electromagnetic field in the situations close to the k-gap with the help of the numerical calculation. The sample is modeled by a multi-layer of air/sinusoidal Au layer/PMMA-DR1/glass substrate. p-polarized plane wave illuminates the sample from the substrate side. **Figure 6.10** shows the intensity of $\mathbf{H}$, $\mathbf{E_x}$, $\mathbf{E_z}$ in the proximity of the sample surface. The interfaces between the different layers are marked

by dashed white lines. The calculation are reported for $\lambda = 733nm$ and $\lambda = 742nm$ and the angles of incidence associated with the minima of the far-field reflectivity. For each energy level, the far-field reflectivity reaches minimum at two values of the angle of incidence.

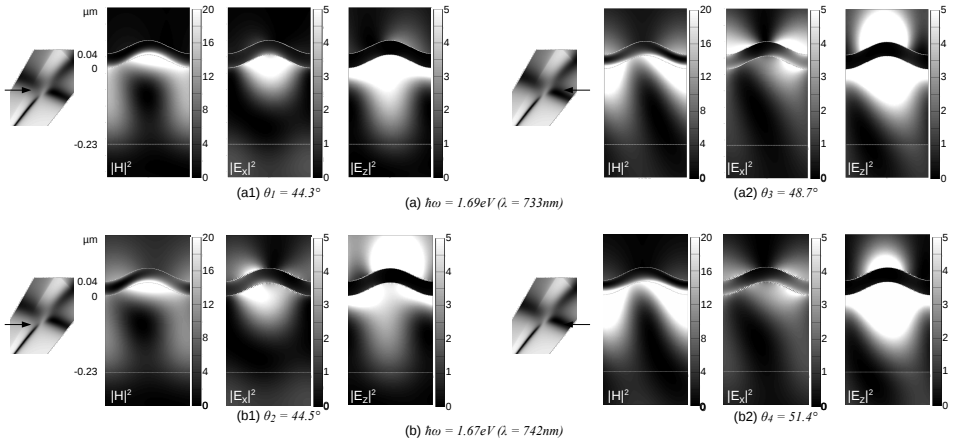

Figure 6.10: Calculated optical near-field of the 1D patterned sample excited by a p-polarized light beam of (a) $\lambda = 733nm$, (b) $\lambda = 742nm$. For each λ, the intensity of the field components $\mathbf{H}$, $\mathbf{E_x}$, $\mathbf{E_z}$ are computed for the angle of incident corresponding to reflectivity minima.

Regarding the dispersion band on the left of the apparent k-gap, the reflectivity is minimized at $\theta_1 = 44.3°$ for $\lambda = 733nm$ (**Figure 6.10** (a1)) and $\theta_2 = 44.5°$ for $\lambda = 742nm$ (**Figure 6.10** (b1)). At θ_1, the field enhancement is observed only at the Au/PMMA-DR1 interface suggesting that SP is only excited there. At θ_2, the field enhancement occurs on both side of the metal film, the two SPs are simultaneously excited. Concerning the dispersion band on the right of the apparent k-gap. The reflectivity reaches minimum at $\theta_3 = 48.7°$ for $\lambda = 733nm$ and $\theta_4 = 51.4°$ for $\lambda = 742nm$. The simultaneous field enhancement occurs in both cases (**Figure 6.10** (a2, b2)). Nonetheless, in the case of θ_3, the field enhancement is stronger and more equally distributed on the two metal interfaces. We conclude that the cross-coupling of the SPs results in simultaneous field enhancement on both sides of the metal layer at two different value of the angle of incidence. However, the most equal field distribution does not necessarily occur at the same wavelength for the left and the right dispersion curves with respect to the apparent k-gap.

6.5.2 2D structure

We now study the optical and the plasmonic properties of continuous Au films which are corrugated along two perpendicular directions. $40nm$-thick of Au is deposited on a PMMA-DR1 film having 2D pattern of period $250nm$ and of height $40nm$. The obtained Au film exhibits the same structure as the PMMA-DR1 template with the lattice constants: $a_{(1,0)} = a_{(0,1)} = 250nm$ while $a_{(1,1)} = 354nm$, as illustrated in **Figure 6.11** (a).

Far-field reflectivity

Figure 6.11 shows the far-field reflectivity measurements conducted with a red laser beam ($\lambda = 633nm$, beam diameter $1mm$) under p and s polarization. **Figure 6.11** (c-d) report the reflectivity of a flat film (++), a 2D-corrugated film under three sample configurations: $((1,0)$, —), $((1,1)$, $\cdots)$ and $((0,1)$, $--)$.

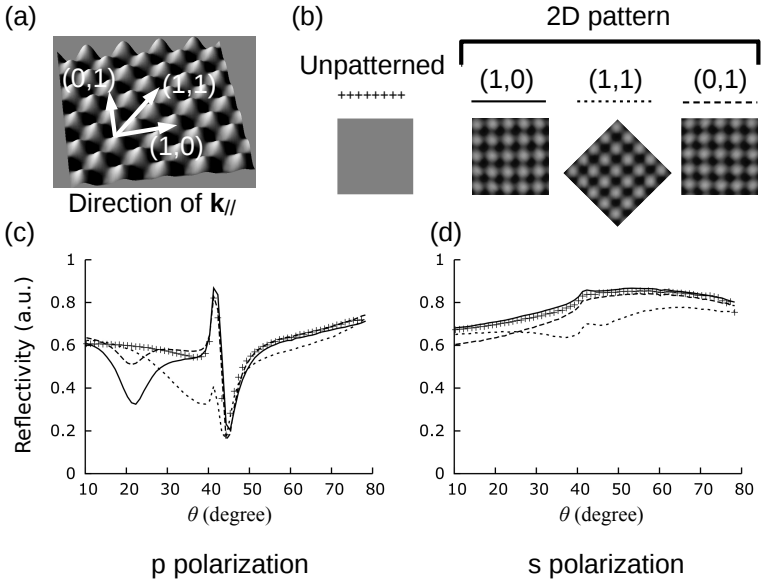

Figure 6.11: Far-field reflectivity measurements. The sample is illuminated by a red laser beam ($\lambda = 633nm$, beam size $1mm$). (a) The directions of $\mathbf{k}_{\|}$ corresponding to the different orientation of the surface grating. (b) The configurations of the sample and the corresponding reflectivity curves: (++) flat surface; sample with 2D pattern in (—) $(1,0)$ orientation, $(\cdots)$ $(1,1)$ orientation and $(--)$ $(0,1)$ orientation. (c) Reflectivity under p polarizations. (d) Reflectivity under s polarization.

When the sample is in the $(1,0)$ or the $(1,0)$ orientation, the measured reflectivity is similar to the case of the 1D structure shown in **Figure 6.6**

(b). Under s polarization, SP is not excited and the reflectivity resembles the one of a flat Au film. Under p polarization, the SP couplings give rise to reflectivity dips at the angles of incidence fulfilling the phase-match condition **C2**.[8] The two observed dips are associated with the Au/PMMA-DR1 and the Au/air SPs. The reflectivity attains higher minimum when the Au/PMMA-DR1 SP is excited in the $(0,1)$ $(--)$ than in the $(1,0)$ direction $(—)$. The 1^{st} order diffraction at the origin of the Au/PMMA-DR1 SP coupling is more efficient in the latter case. When the sample is in the $(1,1)$ orientation, two reflectivity dips are observed under both p and s polarizations. The optical processes giving rise to these dips will be clarified when we establish their dispersion relations in the next section.

SP dispersion relation

Figure 6.12 shows the measured reflectivity spectra for three grating orientations: (a) $(0,1)$, (b) $(1,0)$ under p polarization and (c, d) $(1,1)$ under p and s polarizations, respectively, (e) shows a unit lattice of the surface pattern in the $(1,1)$ direction, (f) represents schematically the different SP coupling processes taking place in this case of sample orientation (c) and (d). In fact, in the experiment, the sample was placed slightly off the precise angle for the $(1,1)$ direction.

Comparing the SP resonances measured in the $(0,1)$ and the $(1,0)$ directions, we note that the Au/PMMA-DR1 SP's dispersion curve is less pronounced in the former case. It reflects our remark made previously on the minimal reflectivity associated with the Au/PMMA-DR1 resonance. However, the SNOM measurement shows the same corrugation hight and period in both directions. The Au film was deposited in normal incidence and would exhibit isotropic optical index. Therefore, the difference in the diffraction efficiency points to an anisotropy in the optical index of the PMMA-DR1 layer as a consiquence of the sequential patterning. Here, the apparent k-gap is only observed in the $(1,0)$ direction. This is because one of the dispersion curves, or more precisely trajectories of the zeros, involved in giving rise to the apparent k-gap is brought about by grating diffraction. The amplitude of the diffracted wave determines the outcome of the interference process at the origin of the apparent k-gap.

Regarding the $(1,1)$ direction, the Au/air SP is only excited under p polarization (**Figure 6.12** (c, d)). In addition, two other dark bands, labeled (i) and (ii) are observed. Comparing with the reflectivity measurement in **Figure 6.11** (c), under p polarization, one of the dark band is the trajectory of the reflectivity minimum before the total reflection whereas the other dark band is the trajectory of a minimum which is hidden by the Au/air

[8] See 4.2

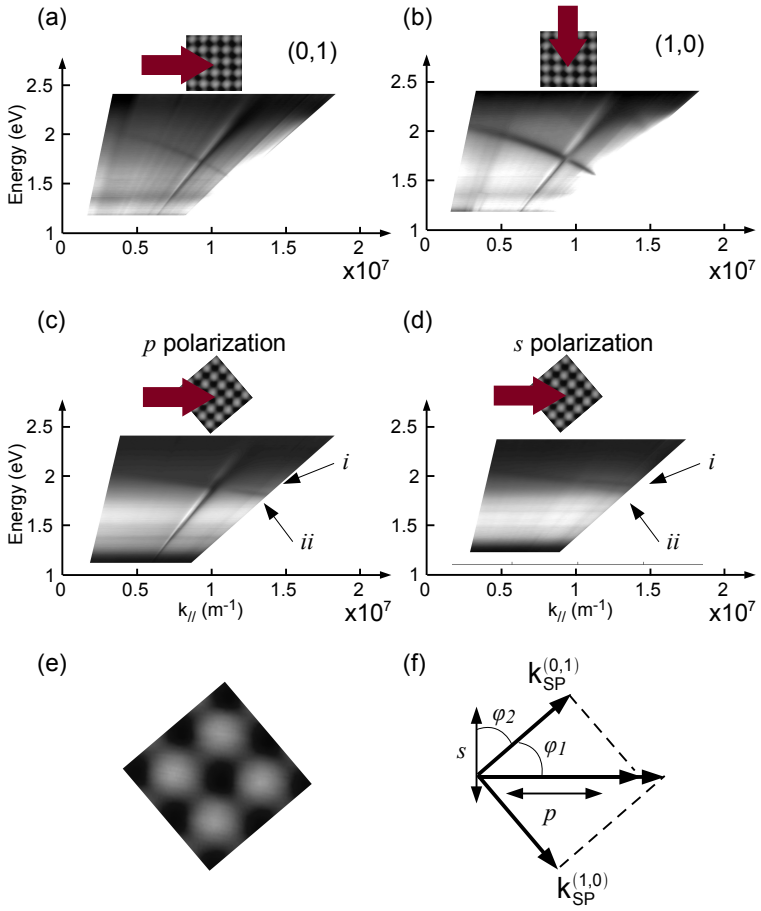

Figure 6.12: Dispersion relations of the SPs on a 2D-patterned Au film measured for different directions of the surface grating. (a, b): $(1,0)$ and the $(0,1)$ directions, both are measured under p polarization. (c, d): $(1,1)$ direction measured under p and s polarizations, respectively. (e) The orientation of the surface grating in the (c, d) measurements. (f) Schematic representation of the SP coupling processes occurring in (c, d).

SP resonance. Under s polarization, the two distinct dark bands are the trajectories of the two reflectivity minima reported in **Figure 6.11** (d). It is noteworthy that these additional dark bands are the same under p and s polarized illumination. In order to identify the origin of these dark bands, we note that:

- The dark bands are trajectories of zeros. This point to some resonant coupling process.

- The dark bands are only observed in the $(1,1)$ direction. The surface

grating plays thus an important role.

- Under s and p polarizations, the resonance requires the same phase-match condition.
- The two dark bands approach the energy as $k_{\parallel}$ tends to zero.

Here, we propose an explanation in temrs of the Au/PMMA-DR1 SP excitation which propagates along a tilted direction with respect to the plane of incidence. Denote $\mathbf{k}_{\parallel \mathbf{i}}$ $(i = 1, 2)$ in-plane wavevector of the illumination, $\mathbf{k}_{\mathbf{a}}^{(\mathbf{m},\mathbf{n})}$ $m = 0, 1$, $n = 1 - m$ the grating vector in the direction (m, n), $k_{SP}^{Au/PMMA-DR1}$ the Au/PMMA-DR1 SP's wavevector. Under p polarization, the polarization condition is automatically fulfilled, the Au/PMMA-DR1 SP is excited if one of the the following phase-match conditions is met:

$$\mathbf{k}_{\parallel \mathbf{1}} - \mathbf{k}_{\mathbf{a}}^{(\mathbf{0},\mathbf{1})} = k_{SP}^{Au/PMMA-DR1}$$

or

$$\mathbf{k}_{\parallel \mathbf{2}} - \mathbf{k}_{\mathbf{a}}^{(\mathbf{1},\mathbf{0})} = k_{SP}^{Au/PMMA-DR1}$$

Assume that φ_1 and φ_2 are the angles between the plane of incidence and the direction $(0, 1)$ and $(1, 0)$, respectively, given $\varphi_1 + \varphi_2 = 90°$. When $\varphi_1 \neq 45°$, $\mathbf{k}_{\parallel \mathbf{1}} \neq \mathbf{k}_{\parallel \mathbf{2}}$, there exist two possible values of $\mathbf{k}_{\parallel}$ at which Au/PMMA-DR1 SP can be excited. The same phase-match condition applies for s polarization. Moreover, the polarization can be fulfilled thanks to the 2D corrugation of the surface. Indeed, the curvature of the surface in two perpendicular directions results that at certain places the s-polarized incident electric field can possess a component perpendicular to the Au surface.

6.6 Arrays of Au lines

Periodic arrays of Au structures can be fabricated by GLAD on a patterned surface as illustrated in **Figure 6.2** (b). Au structures deposited on an PMMA-DR1 film can also be optically modified. Here, we are interested in controlling the optical and the plasmonic properties of the Au line arrays by illumination. We consider arrays of $823nm$-separated, $318nm$-wide, $30nm$-thick Au lines supported by a $250nm$-think PMMA-DR1 film. These arrays are fabricated by GLAD of Au on a PMMA-DR1 surface having 1D periodic structure of the same lattice constant. Three types of arrays are considered: straight Au lines, wavy Au lines in which the modulation period is either $823nm$ or $506nm$. The arrays of wavy Au lines are obtained by two different methods: a "1-shot" approach in which Au is deposited on a 2D structure, referred to as 1-shot array, and a sequential approach in which the array of

straight Au lines is subsequently deformed by illumination, referred to as sequential array.

6.6.1 Spectra of transmission

The transmission spectra in **Figure 6.13** reveal how the plasmonic properties of the Au lines can be optically modified. The samples are illuminated at normal incidence by polarized light from the glass substrate side. The transmitted intensity is measured and normalized to the transmittance of the glass substrate. For all the samples, the absorption band between $400nm - 600nm$ is attributed to the photo-isomerization of the azobenzene molecules. The more the film had been irradiated in order to generate the surface structure, the less it absorbs because of the angular hole-burning (see 1.1.3) and that the azobenzene molecules are photodegraded. The transmittance (a1) measured on a flat area indicates that no optical asymmetry related to the evaporation direction of Au is of concern.[9]

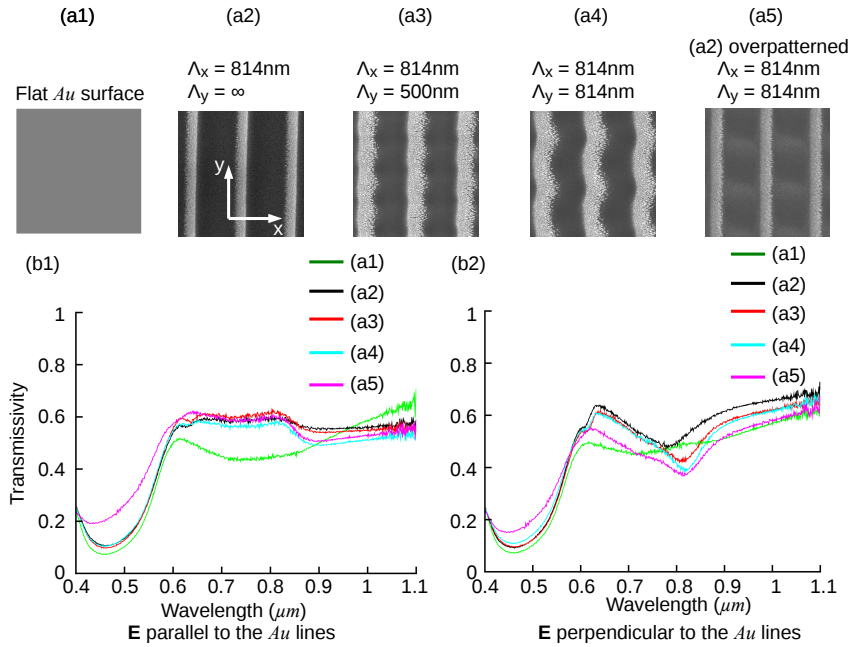

Figure 6.13: Spectra of transmission under normal incident illumination. (a1) Flat Au film. (a2-4) SEM images of the different Au line arrays. (b) Absorptivity when the light polarization is (b1) parallel and (b2) perpendicular to the Au lines.

We now consider the wavelength range $600nm - 1100nm$. When the

[9]The Au film is thinner than the Au lines because they do not see the Au flux at the same angle of incidence.

light polarization **E** is parallel to the *Au* lines, the transmittance is globally the same for all the studied structures. The shouldering observed at $\lambda \approx 823nm$ is associated with the passing-off of the $\pm 1th$ orders of diffraction. The drop of transmittance at the passing-off of the $\pm 1th$ indicates that the energy recovered from the passed-off orders are distributed to the guided modes of the substrate which has higher refractive index than air. When **E** is perpendicular to the *Au* lines, we observe transmittance minima at $782nm$ for the structure (a2) and at about $816nm$ for (a3, a4). The polarization dependence of these minima suggests that they are related to plasmonic resonance, either localized surface plasmon resonance (LSPR) or lattice SP. In the former case, the incident wave is in resonance with the surface electron oscillation of and perpendicular to each *Au* line. In the latter case, the LSPR on the *Au* lines oscillate coherently creating a wave propagating perpendicular to the *Au* lines and in parallel with the surface.[10] However, like the grating coupling of the SP, the resonance of the lattice SP should occur at larger wavelength than the passing-off of the $\pm 1th$ diffraction orders. We therefore attribute these minima to the LSPR.

We note that the 1-shot and the sequential arrays exhibit LSPR at the same wavelength. This suggests a link between the LSPR and the structure of the *Au* line. Comparing the LSPR wavelength of the straight, the $506nm$-pitch and the $823nm$-pitch wavy *Au* line arrays show a red-shift of the LSPR wavelength in the presence of a modulation along the *Au* lines. Moreover, the *Au* lines having the same modulation exhibit the same wavelength shift of the LSPR even though they are fabricated by different methods: 1-shot or sequential.

6.6.2 Dispersion relation

Like in the case of *Au* thin film, the dispersion relation of the LSPR can be established by angular resolved reflectance spectroscopy. **Figure 6.14** (a) reports the reflectivity spectra measured when the *Au* lines is parallel to the plane of incidence and is perpendicular to the light polarization (i.e. *s* polarization). The dispersion relations of the LSPR are the curves indicated by the arrows in **Figure 6.14** (a1, a2). Indeed, these curves extrapolate to intersect the $\hbar\omega$-axis at $1.55eV$ which is approximately the LSPR's energy when it is excited under normal incidence ($\lambda = 782nm$ and $\lambda = 816nm$ for straight and wavy *Au* lines, respectively). These dispersion curves are linear and exhibit a group velocity of about $3.2 \times 10^5 m/s$ (measured at $k_{\parallel} = 0.5 \times 10^7 (m^{-1})$).

When the *Au* lines are perpendicular to the plane of incidence and the

[10] This lattice SP is the equivalence of the SP in the case of discontinuous periodic metal film.

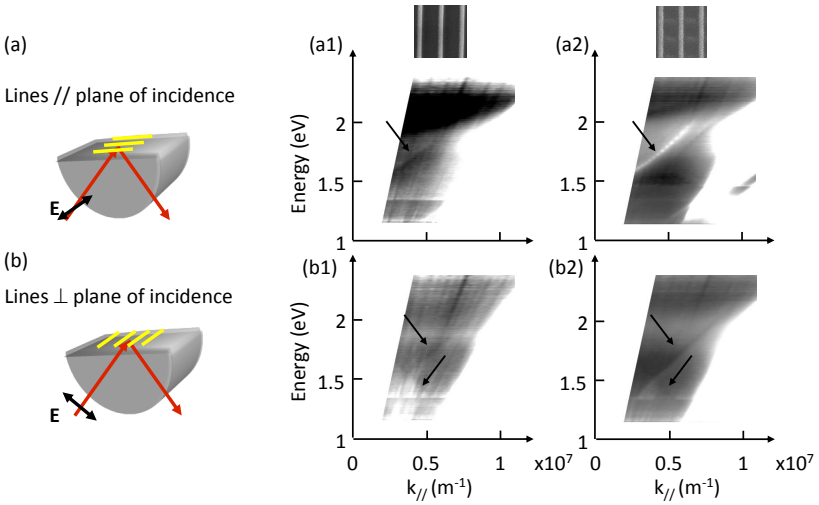

Figure 6.14: Dispersion of the LSPR as they propagate (a) along the *Au* line, (b) across the the *Au* lines.

light polarization (p polarization), as shown in **Figure 6.14** (b), we do not observe signature of the LSPR. The observed dark curves indicated by the arrows are actually due to grating diffraction. Indeed, they do not extrapolate to intersect the $\hbar\omega$-axis at the LSPR energy $1.55eV$ under normal incidence illumination. Moreover, their existence does not depend on illumination polarization. The same curves were observed when the illumination polarization was rotated to s. The possible reason would be the complex cross section of the *Au* lines and their asymmetric geometry (bounded by air and PMMA-DR1 on the either sides). Changing the angle of incidence is equivalent to rotating the *Au* lines along their longitudinal axis with respect to the illumination. This changes the LSPR coupling condition and may strongly attenuate or shift the resonance out of the investigated energy and wavevector range.

By taking advantage of the photo-mechanical properties of the azobenzene-containing film, it is possible to optically modify the plasmonic properties of *Au* lines. We evidence this possibility by showing how changing the shape of the *Au* lines influences their LSPR.

6.7 Conclusion

We have demonstrated a simple method for the fabrication of metal gratings based on the photo-generation of SRGs in the azofilm. This technique

is used to in our study of the optical and the plasmonic properties of metal periodic structures. Two complementary studies have been pursued. On one hand, we study the coupling of the SPs propagating at the different interfaces of a continuous metal film. On the other hand, we explore the possibility to optically manipulate the optical and the plasmonic properties of periodic arrays of metal lines. Regarding the case of continuous metal films, the surface grating gives rise to plasmonic energy band gap. Furthermore, we observed an apparent k-gap in the reflectivity spectroscopy measurement. This gap arises from the interference of the counter propagating SPs associated with the different interfaces of the metal film. Near-field measurements show the confinement of the plasmon-enhanced optical field on the periodic structure, in agreement with numerical calculation. Regarding the optical manipulation of the optical and the plasmonic properties, we demonstrated the possibility to optically inscribe a periodic structure along Au stripes. This, in turn, gives rise to changes in the optical properties of the Au stripes.

Bibliography

[1] Axel Nemetz, Ulrich Fernandez, and Wolfgang Knoll. Surface plasmon field-enhanced Raman spectroscopy with double gratings. *Journal of Applied Physics*, 75(3):1582–1585, 1994.

[2] W. L. Barnes, T. W. Preist, S. C. Kitson, and J. R. Sambles. Physical origin of photonic energy gaps in the propagation of surface plasmons on gratings. *Phys. Rev. B*, 54:6227–6244, Sep 1996.

[3] SC Kitson, William L Barnes, and JR Sambles. Full photonic band gap for surface modes in the visible. *Physical review letters*, 77:2670–2673, 1996.

[4] TW Ebbesen, HJ Lezec, HF Ghaemi, and T Thio. Extraordinary optical transmission through sub-wavelength hole arrays. *Nature*, 1998.

[5] William L WL Barnes, Alain Dereux, and Thomas W TW Ebbesen. Surface plasmon subwavelength optics. *Nature*, 424(August):824–830, 2003.

[6] L. Lévesque and P. Rochon. Surface plasmon photonic bandgap in azopolymer gratings sputtered with gold. *J. Opt. Soc. Am. A*, 22(11):2564–2568, Nov 2005.

[7] Paul L. Rochon and Luc Lévesque. Standing wave surface plasmon mediated forward and backward scattering. *Opt. Express*, 14(26):13050–13055, Dec 2006.

[8] R. J. Stockermans and P. Rochon. Experimental demonstration of photonic bandgaps in azopolymer resonant waveguide grating systems. *J. Opt. Soc. Am. A*, 24(8):2457–2463, Aug 2007.

[9] Ribal Georges Sabat, Nathan Rochon, and Paul Rochon. Dependence of surface plasmon polarization conversion on the grating pitch. *J. Opt. Soc. Am. A*, 27(3):518–522, Mar 2010.

[10] Justin Jefferies and Ribal Georges Sabat. Surface-relief diffraction gratings' optimization for plasmonic enhancements in thin-film solar cells. *Progress in Photovoltaics: Research and Applications*, 22(6):648–655, 2014.

[11] N. K. Viswanathan, S. Balasubramanian, L. Li, S. K. Tripathy, and J. Kumar. A detailed investigation of the polarization-dependent surface-relief-grating formation process on azo polymer films. *Jap. J. Appl. Phys. Part 1*, 38(10):5928–5937, 1999.

[12] F. Fabbri, D. Garrot, K. Lahlil, J. P. Boilot, Y. Lassailly, and J. Peretti. Evidence of two distinct mechanisms driving photoinduced matter motion in thin films containing azobenzene derivatives. *The Journal of Physical Chemistry B*, 115(6):1363–1367, 2011.

[13] Filippo Fabbri. *Déformation photoinduite dans les films minces contenant des derivés d'azobenzene: effets de polarisation, effets de proximité et effets de contact*. PhD thesis, Ecole Polytechnique, 2009.

[14] Lifeng Li, Jean Chandezon, Gérard Granet, and Jean-Pierre Plumey. Rigorous and efficient grating-analysis method made easy for optical engineers. *Appl. Opt.*, 38(2):304–313, Jan 1999.

[15] M. G. Moharam and T. K. Gaylord. Rigorous coupled-wave analysis of planar-grating diffraction. *J. Opt. Soc. Am.*, 71(7):811–818, Jul 1981.

[16] M. G. Moharam and T. K. Gaylord. Diffraction analysis of dielectric surface-relief gratings. *J. Opt. Soc. Am.*, 72(10):1385–1392, Oct 1982.

[17] M. G. Moharam, Eric B. Grann, Drew A. Pommet, and T. K. Gaylord. Formulation for stable and efficient implementation of the rigorous coupled-wave analysis of binary gratings. *J. Opt. Soc. Am. A*, 12(5):1068–1076, May 1995.

[18] Philippe Lalanne and G. Michael Morris. Highly improved convergence of the coupled-wave method for tm polarization. *J. Opt. Soc. Am. A*, 13(4):779–784, Apr 1996.

[19] Lifeng Li. Use of fourier series in the analysis of discontinuous periodic structures. *J. Opt. Soc. Am. A*, 13(9):1870–1876, Sep 1996.

[20] Gérard Granet. Reformulation of the lamellar grating problem through the concept of adaptive spatial resolution. *J. Opt. Soc. Am. A*, 16(10):2510–2516, Oct 1999.

[21] Pavel Kwiecien. rcwa-1d. Sourceforge, 03 2014.

[22] Evgeny Popov, Michel Nevière, Boris Gralak, and Gérard Tayeb. Staircase approximation validity for arbitrary-shaped gratings. *J. Opt. Soc. Am. A*, 19(1):33–42, Jan 2002.

[23] K. Robbie, M. J. Brett, and A. Lakhtakia. Chiral sculptured thin films. *Nature*, 384(6610):616–616, December 1996.

[24] T Karabacak, JP Singh, Y-P Zhao, G-C Wang, and T-M Lu. Scaling during shadowing growth of isolated nanocolumns. *Physical Review B*, 68(12):125408, 2003.

[25] Alireza Dolatshahi-Pirouz, Mads Bruun Hovgaard, Kristian Rechendorff, J Chevallier, M Foss, and F Besenbacher. Scaling behavior of the surface roughness of platinum films grown by oblique angle deposition. *Physical Review B*, 77(11):115427, 2008.

[26] V. I. Safarov, V. A. Kosobukin, C. Hermann, G. Lampel, J. Peretti, and C. Marlière. Magneto-optical effects enhanced by surface plasmons in metallic multilayer films. *Phys. Rev. Lett.*, 73:3584–3587, Dec 1994.

[27] E. Popov. Plasmon interactions in metallic gratings: ω- and k-minigaps and their connection with poles and zeros. *Surface Science*, 222(2–3):517 – 529, 1989.

[28] Rw Gruhlke, Wr Holland, and Dg Hall. Surface plasmon cross coupling in molecular fluorescence near a corrugated thin metal film. *Physical review letters*, 56(26):2838–2841, June 1986.

[29] M. G. Weber and D. L. Mills. Determination of surface-polariton minigaps on grating structures: A comparison between constant-frequency and constant-angle scans. *Phys. Rev. B*, 34:2893–2894, Aug 1986.

[30] S. Wedge, I. Hooper, I. Sage, and W. Barnes. Light emission through a corrugated metal film:?the role of cross-coupled surfaceplasmon polaritons. *Physical Review B*, 69(24):245418, June 2004.

[31] I Pockrand. Coupling of surface plasma oscillations in thin periodically corrugated silver films. *Optics Communications*, 13(3):311–313, 1975.

[32] Anne-Laure Fehrembach, Stéphan Hernandez, and Anne Sentenac. k gaps for multimode waveguide gratings. *Phys. Rev. B*, 73:233405, Jun 2006.

Part III

Conclusion and perspectives

Conclusion

In this work, our goal is to exploit the photo-mechanical properties of the azobenzene-containing thin films for the optical manipulation of nano-objects and for obtaining and studying the optical and the plasmonic properties of metal gratings. Local probe microscopy has been employed to measure the topography and the optical field at submicronic scale.

We have demonstrated, for the first time, the optical displacement of metal or dielectric NPs at the surface of azobenzene-containing thin film. Motion over several microns is achieved along the direction controlled by the light polarization. The dependence of the movement on the illumination configuration and on the properties of the azofilm has allowed to attribute the NP transport to the photofluidization. It turns out that the light polarization plays a predominant role. We have derived a phenomenological formula to capture the relation between the movement speed and the illumination condition. This finding provides a novel toolkit for the manipulation of NPs and new insight into the mechanisms of the photo-induced mass transport in azobenzene-containing films.

On the other hand, we have developed a light-based method to elaborate metal gratings with no requirement of masking and development steps. The obtained periodic structures consist of Au deposited on photochromic film and can have various shape (lines, dots, ...). 1D and 2D patterned films are achieve by tailoring the photopatterning and the metal deposition. The optical and the plasmonic properties of these structures are studied. In particular, we have measured the dispersion relations of the surface plasmons (SP) supported by such system. The surface grating participates in the SP coupling process and gives rise to plasmonic energy band gap and apparent k-gap. The latter occurs in the trajectories of the zeros of the system's scattering matrix and is created by the interference of the counter propagating SPs pertaining to the different interfaces of the metal film. These results are reproduced by numerical calculation using the RCWA.

Perspectives

We present here several directions we would like to pursue beyond this work. First, we are interested in translating this work to the azobenzene-containing thin film fabricated by sol-gel process. These silica-based films are robust, more chemically stable and their mechanical properties can be adjusted without affecting the structure. In particular, using an appropriate combination of vacuum and heat treatment, it is possible to remove completely the photochromic molecules once the desired surface structure is achieved. This

results in transparent nanostructured films which are more suitable for the applications in optics.

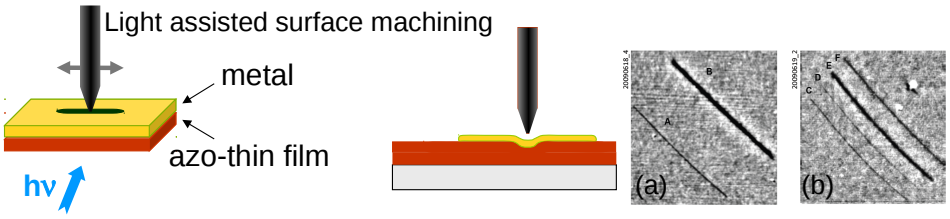

Figure 6.15: Machining of metal thin film deposited on PMMA-DR1 using shear-force tip. Illuminating the surface during the machining allows to enhance the efficiency thanks to the photofluidization of the underlying photochromic film.

The second direction we would like to explore is the control of the spontaneous emission by placing the nano-emitters in the proximity of a plasmonic structure. Light emission is one of the fundamental process in the light-base devices. The control of the spontaneous emission can be addressed by coupling the emitter to a resonant structure. The SP resonance is therefore a promising candidate in the subwavelength scale. However, the precise positioning of the NPs with respect to a metal structure at nanoscale remains a technological challenge [1, 2].

Our work provides a good framework to address this challenge. Two of the possible schemes are depicted in **Figure 6.16**. Metal structures can be fabricated as described in Chap 6. Moreover, it is possible to locally shape the metal film using a shear-force tip as described in **Figure 6.15** [3]. The shear-force feedback mechanism allows adjusting finely the force applied to the surface whereas the photofluidization of the azofilm facilitate the surface deformation. It is thus possible to adjust the distance between the metal and the emitters in the vertical direction while their lateral disposition can be tailored by using the photo-induced transport of NPs on azofilm demonstrated in this work.

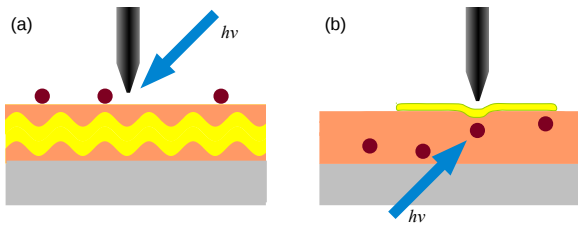

Figure 6.16: Enhancement of the spontaneous emission by plasmonic structures.

It should be noted that when the NPs are buried under metal film, to localize the NPs, one would have to rely on the detection of their near-field. Indeed, this allows resolving the emitters which are of subwavelength size and directly reshaping the metal film at these positions using the tip. The location of the emitter by measuring the optical near-field turns out to be a complex task. Because one needs to scan the tip, the acquisition time for each data point must be reasonably fast. However, the emission through a metal film produce a weak near-field signal which requires long integration time.

Bibliography

[1] A Dousse, L Lanco, J Suffczyński, E Semenova, A Miard, A Lemaître, I Sagnes, C Roblin, J Bloch, and P Senellart. Controlled light-matter coupling for a single quantum dot embedded in a pillar microcavity using far-field optical lithography. *Physical review letters*, 101(26):267404, 2008.

[2] C Belacel, B Habert, F Bigourdan, F Marquier, J.-P. Hugonin, S de Vasconcellos, X Lafosse, L Coolen, C Schwob, C Javaux, B Dubertret, J.-J. Greffet, P Senellart, and A Maitre. Controlling spontaneous emission with plasmonic optical patch antennas. *Nano Letters*, 13(4):1516–1521, 2013.

[3] Filippo Fabbri. *Déformation photoinduite dans les films minces contenant des derivés d'azobenzene: effets de polarisation, effets de proximité et effets de contact.* PhD thesis, Ecole Polytechnique, 2009.

[4] M. Brun, S. Huant, J. C. Woehl, J.-F. Motte, L. Marsal, and H. Mariette. Low-temperature near-field spectroscopy of cdte quantum dots. *Journal of Microscopy*, 202(1):202–208, 2001.